Investigation of diffractively produced $\eta\pi$ and $\eta'\pi$ final states in COMPASS

Henri Clemens Pekeler

Masterarbeit in Physik
angefertigt im Helmholtz-Institut für Strahlen- und Kernphysik

vorgelegt der
Mathematisch-Naturwissenschaftlichen Fakultät
der
Rheinischen Friedrich-Wilhelms-Universität
Bonn

Juni 2019

I hereby declare that this thesis was formulated by myself and that no sources or tools other than those cited were used.

Bonn, ...

Date Signature

1. Gutachter: Prof. Dr. Bernhard Ketzer
2. Gutachterin: Prof. Dr. Ulrike Thoma

Acknowledgements

I would like to thank everybody, who supported me while writing my master thesis. In particular:

- Professor Dr. Bernhard Ketzer, who gave me the opportunity to work on this interesting topic and was always there with some advise and insight on the physical processes
- Professor Dr. Ulrike Thoma, who kindly agreed to be the second corrector for this thesis
- The COMPASS collaboration, for the possibility to work with the data taken during the hadron run in 2008
- Riccardo Longo, who helped me with the setup of the Monte-Carlo tool chain at Blue Waters and provided some very useful tools
- Mikhail Mikhasenko and Mathias Wagner for the great support and many helpful discussions
- Mathias Wagner for proof-reading this thesis
- My girlfriend Lea Krause, for always having my back and supporting me during the last five years

Contents

CHAPTER 1

Introduction

Within the constituent-quark model, a meson consist of a quark (q) and an antiquark ($\bar{q}$). Quarks, together with the leptons[1], are the fundamental particles from which all matter is build of. Quarks carry spin 1/2 and opposite intrinsic parity compared to their antiparticles ($p_q = -p_{\bar{q}}$). Following this, the parity P of a $q\bar{q}$-pair is given as

$$P = p_q \cdot p_{\bar{q}} \cdot (-1)^l = (-1)^{l+1} \tag{1.1}$$

and the charge parity[2] $C = (-1)^{l+S}$, where l is the orbital angular momentum between the $q\bar{q}$ and S the total spin. $S = S_q \oplus S_{\bar{q}}$ can be either 0 or 1, leaving quantum numbers

$$J^{PC} = 0^{--},\ 0^{+-},\ 1^{-+},\ 2^{+-},\ 3^{-+},\ 4^{+-}, \ldots \tag{1.2}$$

to be not possible within a $q\bar{q}$ pair. J is the total spin of the $q\bar{q}$ ($J = l \oplus S$). A particle, which carries these quantum numbers would be called exotic meson. One interesting decay channel is $X^- \to \eta^{(\prime)}\pi^-$, where X^- is some negatively-charged resonance state. The quantum numbers of $\eta^{(\prime)}$ and π^- are

$$J^{PC}(\eta^{(\prime)}) = 0^{-+} \text{ and } J^{PC}(\pi^-) = 0^{-+} \text{ [1]} \tag{1.3}$$

which makes it possible to get quantum numbers $J^{PC} = 1^{-+}$ with orbital angular momentum $l = 1$ (P-wave) between these two particles for the resonance state X^-. Neither π^- nor X^- are eigenstates of the C-parity. Nevertheless, the C-parity of the isospin-triplet partner of the π^-, i.e. π^0, is used to clarify the exotic nature of the X^-.

First evidence of an exotic meson of this kind was reported by the GAMS Collaboration in 1988 [2]. They searched for exotic mesons in the $\pi^- p \to \eta\pi^0 n \to 4\gamma n$ channel at beam energies of 100 GeV and claimed a resonance signal at $m = (1\,406 \pm 20)\,\mathrm{MeV}/c^2$, with a width of $\Gamma = (180 \pm 30)\,\mathrm{MeV}$. However, these results are questioned in [3] but neither ruled out nor confirmed.

In addition, the E852 Collaboration found a resonance like phase motion in the $\rho\pi$ channel, while investigating the reaction $\pi^- p \to \pi^+\pi^-\pi^- p$ at $18\,\mathrm{GeV}/c$, measured by the Brookhaven experiment E852. They extracted resonance parameters of $m = (1593 \pm 8^{+29}_{-47})\,\mathrm{MeV}/c^2$ and $\Gamma = (160 \pm 20^{+150}_{-12})\,\mathrm{MeV}$ via a mass-dependent fit [4].

[1] Electrons, muons and tauons.

[2] Charge parity describes the behavior of a particle under charge conjugation.

In 1998, the Crystal Barrel Collaboration found evidence for a resonant behavior of the $\eta\pi$ P-wave in antiproton-neutron annihilation: $\bar{p}n \to \pi^-\pi^0\eta$. They extracted resonance parameters of $m = (1400 \pm 20 \pm 20)\,\mathrm{MeV}/c^2$ and $\Gamma = (310 \pm 50^{+50}_{-30})\,\mathrm{MeV}$ [5].

Among others, the search for an exotic meson motivated the hadron program of the COMPASS experiment, which had its pilot run in 2004. COMPASS is a fixed-target experiment, which mostly used a negatively-charged pion beam with a momentum of 191 GeV/c during the hadron runs. In 2008 and 2009 the COMPASS experiment took lots of data within the hadron program. In 2010, first results were published [7]. They reported a resonance with spin-exotic quantum numbers $J^{PC} = 1^{-+}$ at 1.66 GeV/c^2 decaying to $\rho\pi$. In 2015 two signals in the $\eta\pi^-$ and $\eta'\pi^-$ final state were seen by the COMPASS collaboration. Fitting a simple Breit-Wigner model to the data, resonance parameters consistent with the $\pi_1(1400)$ decaying to $\eta\pi^-$, and $\pi_1(1600)$ decaying to $\eta'\pi^-$, were extracted. However, they found the $\eta\pi^-$ signal to be suppressed with respect to the $\eta'\pi^-$ signal [8].

Most recently, in 2019, a coupled-channel analysis of the $\eta\pi^-$ and $\eta'\pi^-$ data, taken by the COMPASS experiment, was performed and a rather surprising conclusion was drawn. The authors claim to have found just one hybrid meson with a mass m of $(1564 \pm 24 \pm 86)$ MeV and a width Γ of $(492 \pm 54 \pm 102)$ MeV, which can explain both signals at the same time [9].

The reconstruction of the final state particles for the 2008 and 2009 COMPASS data was heavily improved recently. The calorimeter description of the COMPASS experiment was updated and a new Monte-Carlo software was developed, in order to describe the acceptance of the detector even better. In addition, the reconstruction of the charged particle tracks was improved. Ultimately, this resulted in a new event selection of the 2008 data, which yielded > 40% more events in the $\eta\pi^-$ and $\eta'\pi^-$ final state respectively [10]. This encourages a new analysis of the 2008 data. In addition to the partial-wave analysis in bins of the final-state invariant mass, the data can be separated even further, by splitting it into four slices of the four-momentum transfer t' (see eq. (2.8)). The characterizing parameters of a resonance, e.g. its mass and width, do not depend on different transferred momenta. However, the production mechanism depends on t' through the cross section. By analyzing the data in different t' slices, one should be able to disentangle the background from the resonant signal more easily.

Within this thesis, the next step in analyzing the new data set is done, by performing a first partial-wave analysis of the newly produced data set. This thesis is structured as follows.

In chapter 2 the partial-wave model, which is used in order to describe the COMPASS data, will be introduced. It requires the real data, as well as the description of the detector acceptance. The COMPASS experiment will be introduced in chapter 3, as well as the used software to reconstruct and select good events. The new Monte-Carlo software TGEANT [11] is used in order to generate the Monte-Carlo events, which will undergo the same event selection as the real data [10] and the selected events will serve to determine the detector acceptance. The full generation and analysis procedure of the Monte-Carlo events will be described in chapter 4.

Finally, the combined sample of COMPASS events and newly generated Monte-Carlo events is used to perform the partial-wave analysis. For this, a completely new program is developed and presented in chapter 5. It is programed in object-oriented C++ and operated by a graphical user interface, where many adaptations to the analysis procedure can be made. In chapter 6, first results of the partial-wave analysis will be presented.

CHAPTER 2

Theory

During this thesis, data from the COMPASS experiment in 2008, where a negatively-charged pion beam was shot on a fixed proton target, is under investigation. To be more explicit

$$\pi^- p \to X^- p \to \eta^{(\prime)} \pi^- p, \quad \eta^{(\prime)} \to \pi^- \pi^+ \pi^0(\eta), \quad \pi^0(\eta) \to \gamma\gamma \tag{2.1}$$

will be looked at. The most prominent branching ratios of the η and η' decay are

Table 2.1: Most prominent decay modes, with the corresponding branching ratios, of η and η' as given in [1].

Decay mode of η	branching ratio in %	Decay mode of η'	branching ratio in %
$\eta \to \gamma\gamma$	39.41 ± 0.20	$\eta' \to \pi^+\pi^-\eta$	42.9 ± 0.7
$\eta \to \pi^0\pi^0\pi^0$	32.68 ± 0.23	$\eta' \to \rho\gamma$[1]	29.1 ± 0.5
$\eta \to \pi^+\pi^-\pi^0$	22.92 ± 0.28	$\eta' \to \pi^0\pi^0\eta$	22.2 ± 0.8

The main interest of any analysis is to have as many good events to analyze as possible. Therefore, decay channels with the highest branching ratios are usually preferred. Looking at the decay $X^- \to \eta\pi^- \to \pi^-\gamma\gamma$ or $X^- \to \eta\pi^- \to \pi^- 3\pi^0 \to \pi^- 6\gamma$, π^0 decays almost always ((98.823 ± 0.034) % [1]) into two photons, the primary vertex reconstruction would be tough, as just one charged particle is present in the final state. The track reconstruction of the recoil proton at COMPASS is not very precise and therefore disregarded, while reconstructing the primary vertex. Also, distinguishing six photon clusters in the electromagnetic calorimeters is very complicated. See chapter 3 for more details on the COMPASS experiment. In addition, a final state describing both, the $\eta\pi^-$ and the $\eta'\pi^-$ intermediate state at the same time comes in handy, as the event selection is then practically the same for both cases. The only thing that needs to be changed is the mass cut applied on the $\pi^-\pi^+\gamma\gamma$ mass and the two photon mass, respectively. See sec. 4.4 for more details on the event selection. Because of all these reasons, the three charged pions, two photons and one proton final state is chosen during this thesis.

[1] Including non-resonant $\pi^+\pi^-\gamma$

2.1 Two-body → two-body scattering

Two-body → two-body scattering describes the process, where two incoming particles interact and scatter to two different (inelastic scattering) or the same (elastic scattering) particles (see fig. 2.1).

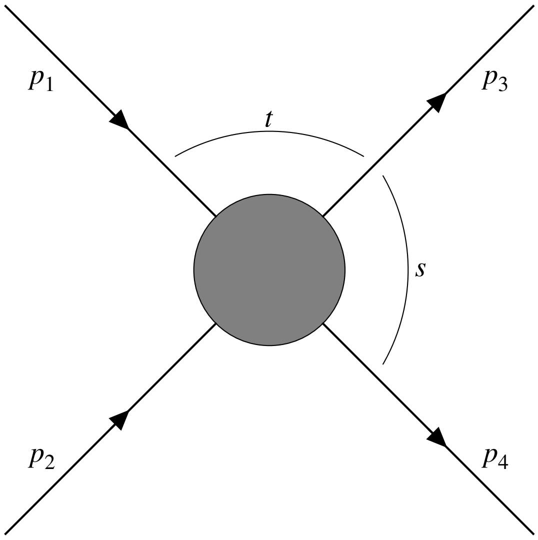

Figure 2.1: General description of two-body → two-body scattering, where the incoming particles are denoted by there four-momenta p_1 and p_2 and the outgoing particles by p_3 and p_4. The Mandelstam variables t and s are shown.

Each particle is characterized by its four-momentum $p = \begin{pmatrix} E \\ \vec{p} \end{pmatrix}$, while the total four-momentum needs to be conserved

$$p_1 + p_2 = p_3 + p_4 \tag{2.2}$$

and the four-momentum squared is given by

$$p^2 = m^2 = E^2 - |\vec{p}|^2 \Leftrightarrow |\vec{p}| = \sqrt{E^2 - m^2} \tag{2.3}$$

The mandelstam variable s describes the invariant mass of the system

$$s = (p_1 + p_2)^2 = (p_3 + p_4)^2 \overset{\text{CM}}{=} \begin{pmatrix} E_3^{\text{CM}} + E_4^{\text{CM}} \\ \vec{0} \end{pmatrix}^2 = \left(E_3^{\text{CM}} + E_4^{\text{CM}}\right)^2 \tag{2.4}$$

while t describes the four-momentum transfer.

$$t = (p_1 - p_3)^2 = p_1^2 - 2p_1 p_3 + p_3^2 = m_1^2 + m_3^2 - 2(E_1 E_3 - |\vec{p}_1||\vec{p}_3| \cos\theta_{13}) \tag{2.5}$$

s, t and p_i^2 are lorentz invariant. Therefore, they can be evaluated in the frame of choice. In this case, this is the Center of Momentum (CM) frame where $\vec{p}_1 = -\vec{p}_2$ and $\vec{p}_3 = -\vec{p}_4$. After some calculation, the energy of one particle in the CM frame is given by

$$\begin{aligned} p_1^2 &= (p_3 + p_4 - p_2)^2 = m_2^2 + (p_3 + p_4)^2 - 2p_2(p_3 + p_4) \\ m_1^2 &= s + m_2^2 - 2\begin{pmatrix} E_2^{\mathrm{CM}} \\ \vec{p}_2^{\mathrm{CM}} \end{pmatrix}\begin{pmatrix} E_3^{\mathrm{CM}} + E_4^{\mathrm{CM}} \\ \vec{0} \end{pmatrix} \\ E_2^{\mathrm{CM}} &= \frac{s + m_2^2 - m_1^2}{2\sqrt{s}} \end{aligned} \tag{2.6}$$

In a similar manner, E_1, E_3 and E_4 can be deduced. Applying eq. (2.6) and (2.3) to eq. (2.5), one can find a formula for t, which is solely depending on the masses of the given particles and the invariant mass of the system s. Now, the minimal and maximal momentum transfer (t_{min} and t_{max}) can be calculated, by setting $\cos\theta_{13} = \pm 1$.

$$\begin{aligned} t_{\mathrm{min}}^{\mathrm{CM}} &= m_1^2 + m_3^2 - 2\left(\frac{s - m_2^2 + m_1^2}{2\sqrt{s}}\right)\left(\frac{s + m_3^2 - m_4^2}{2\sqrt{s}}\right) - 2\sqrt{\left(\frac{s - m_2^2 + m_1^2}{2\sqrt{s}}\right)^2 - m_1^2}\sqrt{\left(\frac{s + m_3^2 - m_4^2}{2\sqrt{s}}\right)^2 - m_3^2} \\ t_{\mathrm{max}}^{\mathrm{CM}} &= m_1^2 + m_3^2 - 2\left(\frac{s - m_2^2 + m_1^2}{2\sqrt{s}}\right)\left(\frac{s + m_3^2 - m_4^2}{2\sqrt{s}}\right) + 2\sqrt{\left(\frac{s - m_2^2 + m_1^2}{2\sqrt{s}}\right)^2 - m_1^2}\sqrt{\left(\frac{s + m_3^2 - m_4^2}{2\sqrt{s}}\right)^2 - m_3^2} \end{aligned} \tag{2.7}$$

2.2 Partial-wave analysis in $m_{\eta^{(\prime)}\pi^-}$ and t' bins

The underlying model to describe the data collected in the $\eta^{(\prime)}\pi^-$ final state will be the partial-wave model. The phase space of the two-body $\to$ two-body reaction shown in eq. (2.1) can be fully described by different partial waves, in bins of $m_{\eta^{(\prime)}\pi^-}$ and t' for a given data sample.

t' is the transferred momentum from the beam π^- to the $\eta^{(\prime)}$ subtracted by the minimal absolute momentum transfer $|t|_{\mathrm{min}}$.

$$t' = |t| - |t|_{\mathrm{min}} \tag{2.8}$$

$|t|_{\mathrm{min}}$ corresponds to $|t_{\mathrm{max}}|$ (see eq. (2.7)), as t is always negative for the given reaction (2.1). This can be seen rather easily by looking into the definition of t (eq. (2.5)) and inserting momentum conservation (eq. (2.2)), as well as identifying the target proton with particle 2 and the recoil proton with particle 4 from fig. 2.1.

$$t = (p_2 - p_4)^2 = m_p^2 + m_p^2 - 2m_p E_{\mathrm{recoil}} = 2m_p(m_p - E_{\mathrm{recoil}}) < 0 \tag{2.9}$$

t_{min} changes for each event, due to different beam kinematics and hence different s. In order to correct for the bias on t introduced by this, it is convenient to use t' instead of t as a characterizing parameter for the given process.

The relative probability for an event to be in a given bin is described by the so called intensity function, which is the absolute value squared of the sum of each partial-wave included in the model, weighted with a complex amplitude c. The set of kinematic variables τ characterizes given events and the different partial waves are distinguished by J and m. J is the total spin of the $\eta^{(\prime)}\pi^-$ system and m

its projection on the z-axis. In addition, a flat background term is added to compensate for non $\eta^{(\prime)}\pi^-$ background, which is inside the data sample due to some reconstruction or selection errors. For a given bin in $m_{\eta^{(\prime)}\pi^-}$ and t', the intensity function reads

$$I(\tau) = \left| \sum_{Jm} c_{Jm} \Psi_{Jm}(\tau) \right|^2 + |c_{\text{flat}}|^2 \tag{2.10}$$

Each partial wave can be identified as a spherical harmonic. Therefore, the azimuthal angle ϕ and the polar angle θ, of $\eta^{(\prime)}$, are the logical choice for the kinematic variables. Reaction (see eq. (2.1)) follows the rules of strong interaction, which means that parity has to be conserved during the process. Unfortunately, the spherical harmonics are not eigenfunctions of parity. In order to correct for that, a reflection operator is introduced, which preserves all relevant momenta and acts on the rest frame of the $\eta^{(\prime)}\pi^-$ system. The reflection operator is just the parity operator followed by a rotation by π around the y-axis. The basis transforms to the new reflectivity basis as follows [12]

$$|\epsilon, l, m\rangle = a(m) \cdot \left(|l, m\rangle - \epsilon P (-1)^{J-m} |l, -m\rangle \right) \tag{2.11}$$

with

$$a(m) = \begin{cases} \frac{1}{\sqrt{2}} & m > 0 \\ \frac{1}{2} & m = 0 \\ 0 & m < 0 \end{cases} \tag{2.12}$$

The hereby introduced frame is the Gottfried-Jackson (GJ) frame. The $\eta^{(\prime)}\pi^-$ state is at rest and the z-axis is given by the beam axis, while the xz-plane is chosen to be the production plane, i.e. the y-axis is formed via cross product of target and beam. ϵ is the so called reflectivity, which can come in the form of -1 and +1. $\epsilon = +1$ corresponds to natural exchange, i.e. the exchange particle carries natural quantum numbers $J^P = \text{odd}^-$ or even^+, while $\epsilon = -1$ corresponds to unnatural exchange, i.e. the exchange particle carries unnatural quantum numbers $J^P = \text{even}^-$ or odd^+. J is the total spin of $\eta^{(\prime)}\pi^-$ and P the parity of the same.

Following eq. (1.1) and knowing the quantum numbers of $\eta^{(\prime)}$ and π^- (eq. (1.3)), J can be identified as l and $P_{\eta^{(\prime)}\pi^-} = (-1)^l$ for the $\eta^{(\prime)}\pi^-$ system. Accounting for that all, eq. (2.11) now reads

$$|\epsilon, l, m\rangle = a(m) \cdot \left(|l, m\rangle - \epsilon (-1)^{m} |l, -m\rangle \right) \tag{2.13}$$

With a few useful properties of the spherical harmonics

$$\begin{aligned} \Psi_{lm}(\theta, \phi) &= \Psi_{lm}(\theta) e^{im\phi} \\ \Psi_{l(-m)}(\theta, \phi) &= (-1)^m \Psi^*_{lm}(\theta, \phi) = (-1)^m \Psi_{lm}(\theta) e^{-im\phi} \end{aligned} \tag{2.14}$$

where $\Psi_{lm}(\theta)$ is real and * denotes the complex conjugate, the transformation into the reflectivity-basis can be applied to the spherical harmonics and one can distinguish directly between the positive and negative reflectivity parts.

$$\begin{aligned} \Psi^+_{lm}(\theta, \phi) &= 2ia(m) \Psi_{lm}(\theta) \sin m\phi \\ \Psi^-_{lm}(\theta, \phi) &= 2a(m) \Psi_{lm}(\theta) \cos m\phi \end{aligned} \tag{2.15}$$

Within the GJ-frame and the given final state, the angular part of the spherical harmonics can be identified with the Wigner d-functions [12].[2]

$$\Psi_{lm}(\theta) = d_{lm}(\theta) = (-1)^m \sqrt{(l+m)!(l-m)!(l!)^2}\, x^m \left[\sum_{k=0}^{l-m} \frac{(-1)^k x^{2k} y^{2(l-m-k)}}{(l-m-k)!(l-k)!(m+k)!k!}\right] y^m \tag{2.16}$$

with

$$x = \sin\frac{\theta}{2} \text{ and } y = \cos\frac{\theta}{2} \tag{2.17}$$

Now, the intensity function for one $(m_{\eta^{(\prime)}\pi^-}, t')$ bin reads

$$I(\theta,\phi) = \sum_{\epsilon=+1,-1} \left| \sum_{lm} c^{\epsilon}_{lm} \Psi^{\epsilon}_{lm}(\theta,\phi) \right|^2 + |c_{\text{flat}}|^2 \tag{2.18}$$

The strength of each partial wave within the data set is given by c_{lm}, which is first of all a free complex parameter. Therefore, one needs to find a way to determine c_{lm}. The chosen method is to maximize the likelihood function. It is defined as the product of the probability to have N events in a given data set multiplied with the probability to have each of these events with their specific kinematic variables. The amount of data taken with a detector is a statistical process and therefore Poisson distributed.

$$P(N) = e^{-N_e} \frac{N_e^N}{N!} \tag{2.19}$$

where N_e is the expected number of events. Multiplying the intensity function for given kinematic variables $I(\theta,\phi)$ with the acceptance of the detector $\xi(\theta,\phi)$ and integrating that over all angles yields the expected number of events.

$$N_e = \iint I(\theta,\phi)\xi(\theta,\phi)\, \mathrm{d}(\cos\theta)\mathrm{d}\phi \tag{2.20}$$

The probability to find one event k with specific kinematic variables (θ_k, ϕ_k) is the intensity function evaluated at these kinematic variables divided by the expected number of events.

$$P_k = \frac{I(\theta_k \phi_k)}{N_e} \tag{2.21}$$

Combining this, the likelihood function reads

$$\mathcal{L} = e^{-N_e} \frac{N_e^N}{N!} \prod_{k=1}^{N} \frac{I(\theta_k \phi_k)}{N_e} = \frac{e^{-N_e}}{N!} \prod_{i=k}^{N} I(\theta_k \phi_k) \tag{2.22}$$

Maximizing a product is not an easy task. Especially since it is a product of probabilities, which becomes smaller and smaller for an increasing amount of events[3]. It is significantly easier to deal with a sum. In addition, minimizing is simpler than maximizing. Combining this, one can take the natural

[2] They use m' for m and their m is always 0 for the given channel.

[3] The probability is always between 0 and 1

logarithm[4] of the likelihood function and then minimize the negative of that.

$$- \ln \mathcal{L} = N_e - \sum_{k=1}^{N} \ln I(\theta_k \phi_k) - \ln N! \tag{2.23}$$

$\ln N!$ is constant and therefore does not effect the determination of the minimum. Hence, it is dropped for the minimization process, yielding the negative log-likelihood function to be

$$- \ln \mathcal{L} = \iint I(\theta, \phi)\xi(\theta, \phi)\mathrm{d}(\cos\theta)\mathrm{d}\phi - \sum_{k=1}^{N} \ln I(\theta_k \phi_k) \tag{2.24}$$

The first term is described by the detector acceptance and the second one by experimental data. Therefore, Monte-Carlo simulations are performed in order to describe the acceptance of the detector well (see sec. 4), while the real data was taken by the COMPASS experiment in 2008 (see sec. 3).

[4] The natural logarithm is strictly monotonically increasing. Hence, the maximum is at the same location.

CHAPTER 3

The COMPASS experiment

The COmmon Muon Proton Apparatus for Structure and Spectroscopy (COMPASS) is a fixed-target experiment located at the Super Proton Synchrotron (SPS) at CERN in Geneva, Switzerland. One aim of this experiment is to study hadron structure and perform hadron spectroscopy. The experiment can be operated with hadron, electron and muon beams, although electron beams are usually just used for calibration purposes. Within this thesis only the operation with negatively-charged pion beams is considered, during the data taking period in 2008. The COMPASS experiment can be split into four parts along the beam axis. First, the beam line section, where the incoming particles get identified, followed by the target region, the Large Angle Spectrometer (LAS) and the Small Angle Spectrometer (SAS). See fig. 3.1 for a more detailed description of the four sections.

3.1 2008 setup

The layout of the COMPASS detector in 2008 is shown in fig. 3.1. In addition almost all detector components are shown in fig. 3.2 as the detector is shown there from the side and the components are lettered. Both these pictures are created with TGEANT (see section 4.1) and labeled according to [13]. The following description of the detector uses [13] as a guideline. More detailed information of the different detector types can also be found at [14].

3.1.1 Beam line section

The negatively-charged hadron beam is provided as a secondary beam from the 400 GeV protons[1], accelerated at the SPS, scattering off a thin beryllium target. It is a compound of $\pi^-(96.8\%)$, $K^-(2.4\%)$ and $\bar{p}(0.8\%)$ at a beam energy of 191 GeV. The beam type is identified by two CEDAR (ČErenkov[2] Differential counters with Acromatic Ring focus) detectors. The underlying principle is the Cherenkov effect. A charged particle crossing a medium can be faster than the medium speed of light and thus emits electromagnetic radiation. Depending on the refractive index n of the medium, the momentum of the particle p and the mass of the particle m one can then distinguish between pions, kaons and

[1] Natural units will be used throughout this thesis. $c = \hbar = 1$

[2] This is the scientific transliteration of the surname of Pavel Alexeevič Čerenkov, who discoverd the Cherenkov effect. In the following the more common Cherenkov will be used.

antiprotons, by measuring the emission angle θ_c of the radiation.

$$\cos\theta_c = \frac{1}{\beta n} = \frac{m}{p \cdot n} \tag{3.1}$$

The CEDAR detector is filled with helium gas and the pressure and temperature (and therefore n) can be adjusted.

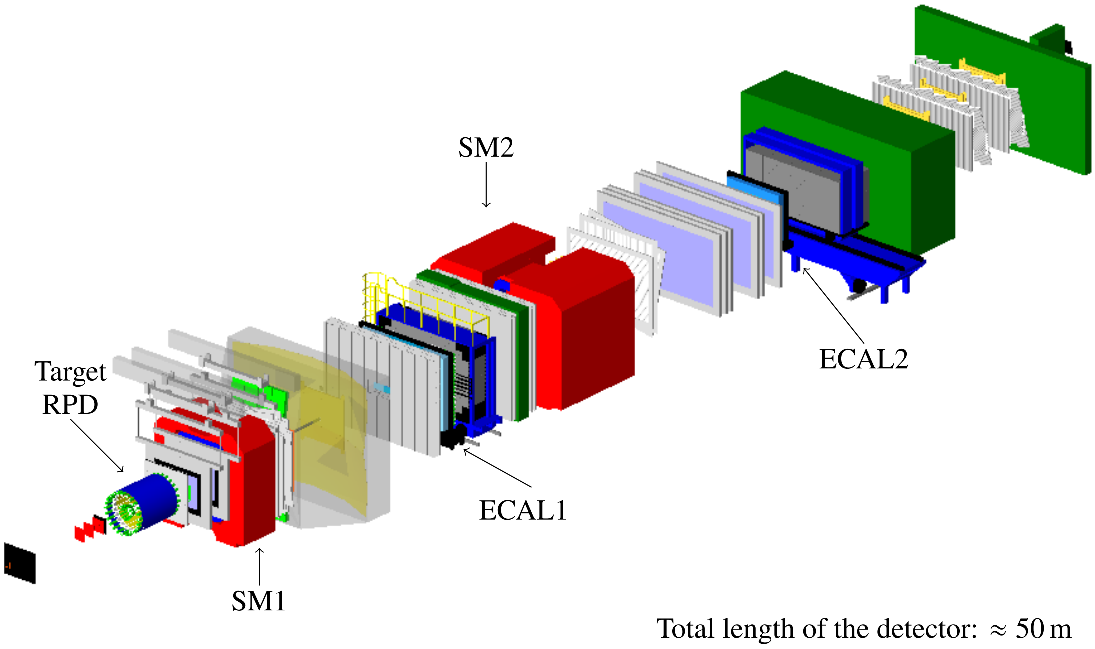

Figure 3.1: 3D view of the COMPASS detector as it was for the hardon run in 2008. The beam goes from the lower left to the upper right corner. Marked are the dipole magnets (SM1 and SM2), the target and recoil proton detector (RPD) and the electromagnetic calorimeters ECAL1 and ECAL2. The beam line section starts upstream of the target and ends right before it. Then, the target region extends up until SM1, followed by the Large Angle Spectrometer (LAS), which concludes before SM2 and the Small Angle Spectrometer (SAS) marks the end of the detector, downstream of SM2 and including the same.

3.1.2 Target region

A cylindrically shaped target cell, with a length of 40 cm and a diameter of 3.5 cm is filled with liquid hydrogen and used as a proton target. Right around it, the recoil proton detector (RPD) is installed. It is a time-of-flight detector, which uses two rings of plastic scintillators, positioned right around the target. The first ring is segmented in 12 slabs and the second into 24, together covering polar angles between 50° to 90°, if one considers a particle produced in the middle of the target. The RPD is used in the trigger system and for the measurement of the momentum direction of the recoiling proton. The trigger requirement is one hit in each ring and a straight line connecting these hits needs to go through

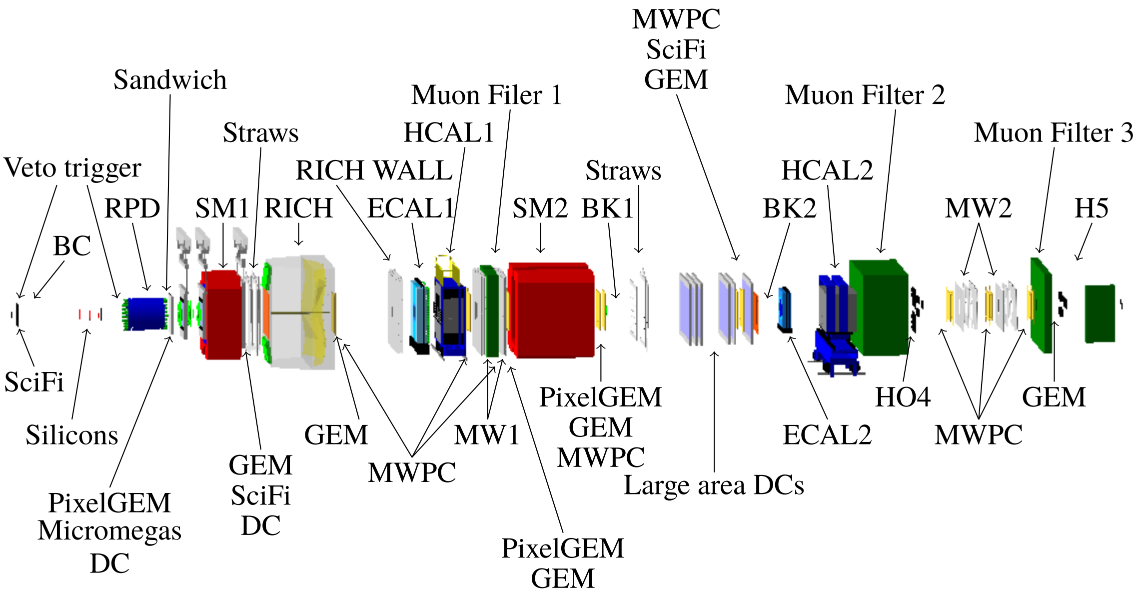

Figure 3.2: Side view of the COMPASS detector setup from 2008, where the beam runs from left to right. Some detector parts are not visible, due to their relatively small size.

the target area.

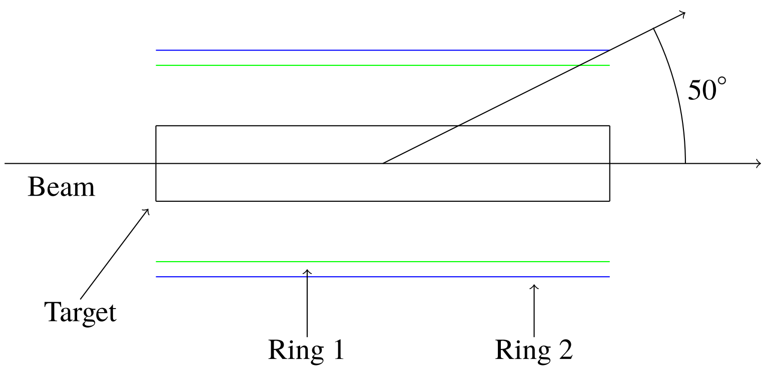

Figure 3.3: Side view of the recoil-proton detector (not to scale), where the target cell is shown in the middle and the two rings are marked in green and blue. The beam axis lies horizontally in the target and one recoil proton with a polar angle of 50 ° is shown. Any recoil proton with a smaller polar angle will not be detected from at least one of the rings of the recoil-proton detector.

Three silicon stations together with a scintillating-fiber counter are positioned upstream of the target, which are tracking detectors, meant to determine the trajectory of the incoming beam. In addition, scintillator hodoscope detectors function as part of the veto system.

A particle emerging from the target region with a polar angle smaller than 50 ° cannot be detected by the RPD, but LAS just covers polar angles up to 180 mrad (≈ 10.3 °). Therefore, any particle with polar angles between 10.3 ° and 50 ° is not registered by the COMPASS detector. The sandwich veto detector is build directly downstream of the target and covers this acceptance gap between RPD and

LAS (see sec. 3.1.3) and consists of five layers of steel-covered lead plates and scintillators, with a central hole, which matches the acceptance of LAS. A hit in the sandwich veto detector therefore signals a particle, which will not be seen by the COMPASS detector, meaning that one would not be able to reconstruct this particle properly. Therefore, events where the sandwich veto detector registers a hit need to be rejected, which makes it part of the veto system of the detector.

3.1.3 Large Angle Spectrometer (LAS)

In order to reconstruct particle momenta, magnets are a powerful tool. The dipole magnets used at COMPASS deflect the outgoing particles and thus separate positively- and negatively-charged particles. In addition, particles with higher momentum get deflected more than such with lower momentum. This results in much better distinguishable particle tracks, which makes their reconstruction a lot easier and in addition requires a smaller detector resolution and therefore, simplifies the detector design.

The large-angle spectrometer features the region around the first dipole magnet SM1. Up- and downstream of the magnet, tracking and particle-identification detectors as well as calorimeters are installed.

Usually a detector needs to measure either energy or momentum. Focusing first on tracking detectors, depending on the position of the given detector inside the whole spectrometer, different criteria are considered. Detectors near the beam axis need to be robust as well as precise in terms of resolution and their readout needs to be as fast as possible. In addition, less material is always good, if no secondary particles should get created inside the detector. Detectors covering wider angle ranges are not required to be super precise, because particles (particle tracks) further away from the beam axis are better distinguishable (e.g. because of the dipole magnets). In order to measure the energy of a given particle, calorimeters are the most common choice. The underlying principle, is the particle shower. The incoming particle showers to many particles, which then have less energy. The three main underlying physical processes are: pair production, where one photon produces an electron-positron pair in presence of a nucleus; bremsstrahlung, where a charged particles gets decelerated in matter and loses energy in form of an emitted photon; and Compton scattering, where a photon collides with matter and loses energy in the process, while the matter recoils and absorbs the energy. A photon hitting the electromagnetic calorimeter would produce an electron and positron via pair production, which would have less energy each then the incoming photon. They would then themselves emit a photon via Compton scattering or bremsstrahlung. This would go on until all particles have so little energy that they are stopped. The energy of the incoming particle is than measured by combining all energies of the secondary, tertiary etc. particles. For this principle to work, a lot of material is necessary. This process is also destructive, which is the reason why calorimeters are placed more downstream of the tracking detectors.

One can distinguish between small-area and large-area tracking detectors. For small-area tracking detectors, GEM (Gas Electron Multiplier) detectors are a common choice throughout COMPASS. They consist of little material and measure particle hits with a typical resolution of some 100 μm. They are gas-filled detectors and operate via ionization of the gas and amplification of the resulting ions or electrons. One alternative is the Micromegas (MICRO-MEsh GAseous Structure) detector, which is operated in a similar way. The read-out signal is very fast (some ns) and they reach a precision of around 100 μm as well. For large-area tracking detectors, wired based gaseous detectors are usually used. They can cover large areas and still reach resolutions of about 250 μm. The large Drift Chambers (DCs) are installed as well as the straw tube chambers (Straws) and a Multi-Wire

Proportional Chamber (MWPC), see fig. 3.2.

In order to identify the particle ID, i.e. its mass, one needs to measures the momentum and either the energy or the speed of the given particle. As seen in sec. 3.1.1, a Cherenkov detector is a good choice for speed measurement. At COMPASS the RICH-1 (Ring-Imaging CHerenkov detector) is installed downstream of SM1. It can seperate pions, kaons and protons up to certain energies, which depend on the medium inside RICH-1. The Rich Wall, which is a drift tube detector, is used for particle tracking between RICH-1 and ECAL1.

ECAL1 (Electromagnetic CALorimeter) and HCAL1 (Hadronic CALorimeter) are installed to measure the energy of electrons or photons and hadrons respectively. As described above, the calorimeters are positioned downstream of the tracking and identifying detectors because they measure the energy destructively. ECAL1 is a combination of 1500 different lead glass module types and divided into three parts, i.e. OLGA, Mainz and GAMS, due to availability and cost reasons. Named after the experiments where these modules were originally used, the OLGA modules cover the outer horizontal, the Mainz modules the outer vertical and the GAMS modules the inner part of ECAL1. In addition, there is a central hole, where particles with small opening angles fly through (see fig. 3.4).

During this work, the electromagnetic calorimeters will become of some interest, as they are the central part in photon reconstruction, while the charged particles are mostly reconstructed via the tracking detectors (sec. 4.4 will cover the reconstruction of charged particles in more detail). Because of that, HCAL1 is of less importance during this thesis.

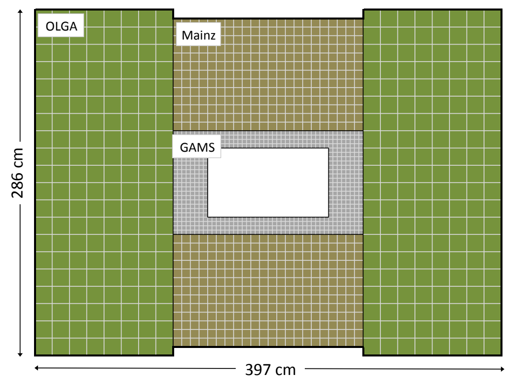

Figure 3.4: Geometrical description of ECAL1. Labeled are the different module types [13]. ECAL1 is viewed against the beam direction, meaning, that the right handed coordinate system is formed by the horizontal x-axis and vertical y-axis, where the z(beam)-axis stands perpendicular to the viewed plane.

More downstream of HCAL1, a Muon Filer is placed, which is essentially a thick absorber. One can identify a muon, if a track can be reconstructed from both parts of the tracking detectors directly up- and downstream of the Muon Filter, the Muon Wall (MW1), because just muons should be able to pass the absorber and leave a hit inside MW1 [15]. LAS covers polar angles up to 180 mrad.

3.1.4 Small Angle Spectrometer (SAS)

The small angle spectrometer (SAS) covers the area downstream of the second dipole magnet SM2, including SM2 itself. The different detector parts can be seen in fig. 3.2. PixelGEM, GEM and SciFi detectors again track the particles throughout SAS, where a high density of tracks is expected, i.e. near the beam line, while Straws, MWPCs and DCs take care of the large area tracking. In addition two beam killers are placed shortly after SM2 and right before ECAL2. They are scintillator counters and placed directly onto the beam axis, so they can identify events, where the beam did not interact with the target. Therefore, they play an important role within the trigger.

Downstream of the tracking detectors, ECAL2 and HCAL2 are stationed. ECAL2 is a compound of three different types, GAMS, GAMS radiation-hardened (GAMS-R) and Shashlik. GAMS and GAMS-R are again lead glass based, each consisting of 1332 and 848 modules respectively and positioned on the most outer part (GAMS) and the part between GAMS and Shashlik (GAMS-R). The Shashlik modules on the other hand are a combination of lead plates and scintillator plates. The hole inside ECAL2 is shifted according to the deflection of the beam from SM1 and SM2 (see fig. 3.5).

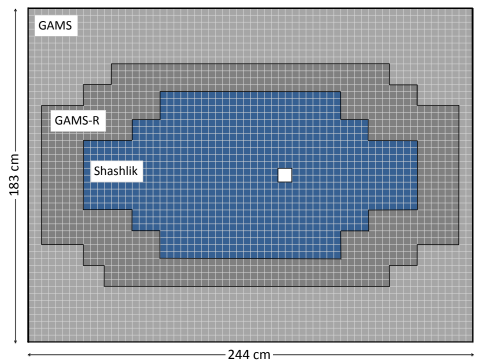

Figure 3.5: Geometrical description of ECAL2. Labeled are the different module types [13]. ECAL2 is viewed against the beam direction, meaning, that the right handed coordinate system is formed by the horizontal x-axis and vertical y-axis, where the z(beam)-axis stands perpendicular to the viewed plane.

Downstream of HCAL2 only the muon tracking remains, again consisting of muon filters (absorbers) and tracking detectors (MW2, MWPCs and GEM), serving a similar purpose than those in the LAS region (see sec. 3.1.3). In addition some scintillator hodoscope detectors are placed to cover the muon trigger [15].

3.1.5 Trigger

The trigger determines on event-by-event basis if the given event is useful or not. In order to select for good events, within this thesis, the following trigger conditions need to be matched. First, an incoming beam needs to be seen. Therefore, the Beam Counter needs to register a hit. Secondly, the beam should have interacted, inside the target region and a recoil proton should have been produced. This means, that the RPD needs to register precisely one recoil proton and the Beam Killers inside SAS can not measure a signal. In addition, all particles, emerging from the primary vertex, need to be measured inside the spectrometer and therefore reconstructible. This means, if a particle is seen by the Sandwich veto detector, the event needs to be rejected.

3.2 Reconstruction and analysis

The important step after the data taking period, is the reconstruction and analysis of good events. At COMPASS this is done in two steps, i.e. with two separate programs, both written in C++.

3.2.1 CORAL

The COmpass Reconstruction ALgorithm (CORAL) is developed and maintained by the COMPASS collaboration and functions as the main reconstruction software [15]. It takes care of decoding and clustering of the raw detector information and then performs track, RICH and beam reconstruction. In addition it performs clustering for the calorimeters and takes care of track-particle association and muon identification. As a last step, vertices get reconstructed and the final information gets stored. The storage is done via ROOT-trees [16], where the track, cluster and vertex information as well as the particle IDs, detector information etc. are stored. These Data Storage Trees (DST) files are taken as an input for the analysis software (see sec. 3.2.2). During this thesis, CORAL output files will be referred to as mDST files, since often just a subset of the whole analyzed data is used and the resulting output is then called mDST (mini Data Storage Tree) file.

CORAL is operated via an option file and needs several inputs for it to work. The complete geometry of the detector in form of a ROOT-geometry as well as additional detector information via a `detectors.dat` file need to be present. In addition, calibration files for the different detector types as well as alignment information have to be available. Inside the CORAL installation, default option files are provided and the user usually just needs to adjust small things, e.g. the path to the `detectors.dat` and ROOT-geometry file, the input data file and how many events should be processed. CORAL also comes with a visualization tool which can be switched on/off by the option file. This comes in very handy if one wants to quickly see the reconstruction event by event.

3.2.2 PHAST

The PHysics Analysis Software Tools (PHAST) is the main analysis software used at COMPASS. It takes an arbitrary amount of mDST files as input and is written extremely user friendly [17]. PHAST takes care of the decomposition of the different events and the user can analyse the data event by event, via a 'UserEventXXX' function, where he or she can specify what kind of analysis should be performed within each event. 'XXX' is hereby an arbitrary number, but one cannot define the same UserEvent twice, i.e. UserEvent1 cannot be present twice. In addition one has the possibility to write a function which will be called each time an event has a different run number in comparison to the previous event via a 'UserRunEndXXX' function and lastly a 'UserJobEndXXX' function which will be called after the last event got processed. These two are very useful, if one wants to show some progress during or at the end of the analysis.

The main usage of PHAST during this thesis will be the eventselection (see sec. 4.4). During this step, every event needs to match certain criteria to be accepted as a good event. In order to reduce future computing time, PHAST provides the possibility to store events, which survived the selection in an mDST file again, often referred to as μDST (micro Data Storage Tree) because the given data sample is even smaller than before. During the event-by-event analysis, the user can decide to save interesting values in ROOT-diagrams.

CHAPTER 4

Monte-Carlo data generation

Monte-Carlo (MC) simulation is a common tool in particle physics. It uses the process of random numbers to solve complicated problems. For detectors in particular, MC simulations are used to describe the detector acceptance and background contributions.

4.1 Simulation at COMPASS

At COMPASS a new MC simulation program called TGEANT (Total Geometry ANd Tracking) was invented in 2016 [11]. It is based on the Geant4 (Geometry ANd Tracking) toolkit [18] and meant to replace the old COMPASS MC simulation program COMGEANT. TGEANT is commonly used newer days for MC simulations, but for the 2008 hardon run[1], COMGEANT was the standard until now. Nevertheless, TGEANT is used during this work to simulate the much needed MC data, as it provides a very detailed description of the different detector parts and the underlying physical processes.

TGEANT is written in object-oriented C++ and therefore follows the programming language used for CORAL and PHAST (see sec. 3.2). In the following, the working principle of TGEANT will be explained and the adjustments, made for this thesis, presented.

All detector components of the COMPASS experiment are implemented in the software package, including the target, the tracking and particle identification detectors as well as the calorimeters and the veto system[2]. TGEANT is operated via a settingsfile, where several options can be chosen, e.g. the detectors which should be present for the upcoming simulation, the alignment and calibration files, the geometrical description of the detectors, some beam properties, the beam file, the event generator and more. TGEANT even provides the possibility to visualize given detector setups and events.

As described in chapter 3, one needs to simulate a 191 GeV π^- beam, scattering off a fixed proton target, where the intermediate state X^- is formed and the final state, i.e. $(\pi^-\pi^-\pi^+\gamma\gamma p)$, is then propagated through the detector simulation.

In order for TGEANT to simulate exactly this, two additional things have to be provided. The information about the incoming beam needs to be given in a specific format and once the primary vertex, i.e. the collision point of the beam π^- and the proton target, is found, the final state particles need to be generated and fed through the detector simulation. Of course, the correct detector parts with

[1] The real data analyzed during this thesis was taken by the COMPASS experiment during the 2008 hadron run.

[2] For a detailed description of the COMPASS experiment, see sec. 3 and [13],[15]

the correct geometrical description and alignment need to be presented as well, but these information just enter via the settingsfile and were given by the COMPASS collaboration for the 2008 data run.

4.1.1 Beam file

The beam file provides information about the incoming beam particle itself. In order to provide realistic beam information, real data events from the 2008 run were analyzed and the beam information extracted. TGEANT requires a particular format for the beam file, where the horizontal and vertical position as well as the slope and the energy of the beam particle need to be provided. In addition, the file needs to be in a specific binary format [19]. The beam file is created with over 8×10^5 events, which should be sufficient as statistical beam fluctuation. The distribution of the beam particles over the horizontal and vertical position (x and y) as well as the slope distribution can be seen in fig. 4.1 and the Energy distribution in fig. 4.2.

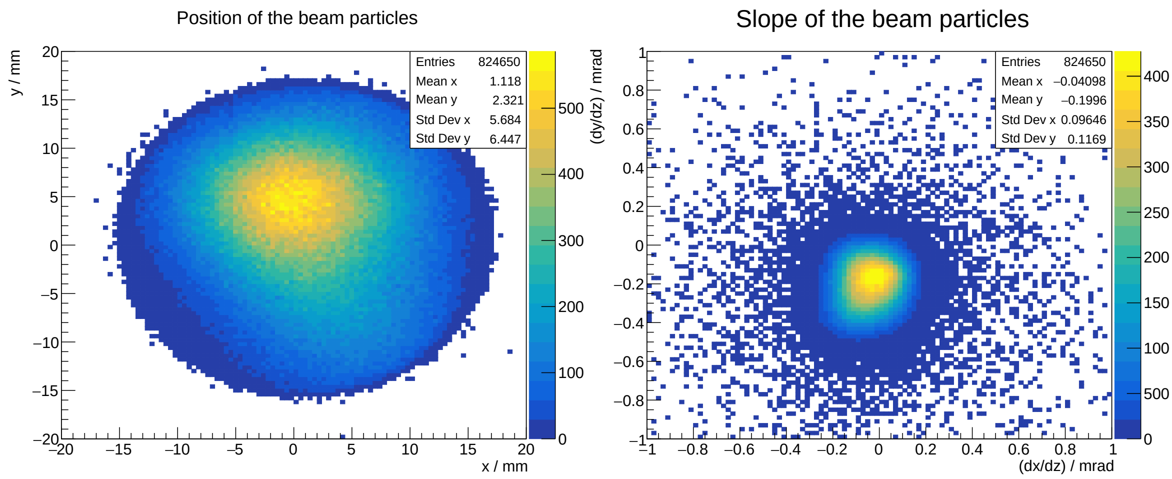

Figure 4.1: Distribution of the beam particles' horizontal and vertical positions, as well as their slope at z=−7.5 m.

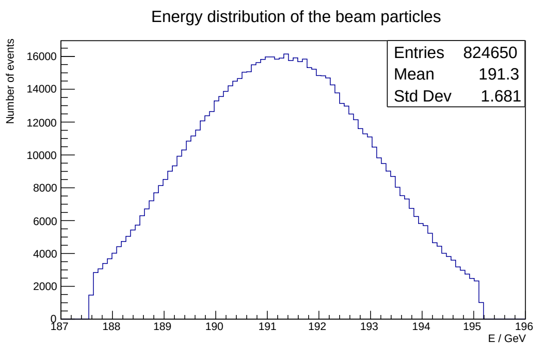

Figure 4.2: Distribution of the energy of the beam particles.

The x and y coordinates are calculated at $z = -7.5$ m, because TGEANT requires a starting point of the beam at that position. Noteworthy is the small slope, below 1 mrad, compared to the acceptance of the COMPASS detector (180 mrad). The energy of the beam particles is nicely centered around 191 GeV with a standard deviation of roughly 1.7 GeV.

4.1.2 Event generator

For the given process (see eq. 2.1), a new event generator was implemented by Waldemar Renz. It is embedded in TGEANT and was first presented in [20] and further improved since then. During this work, the core elements of the generator were tested and approved. In the following, the generator version used to simulate the MC data during this thesis, will be described briefly.

A fixed number of events is generated per TGEANT call. This number can be set inside the settings file. At the TGEANT start, a random starting point in the beam particle list (generated of the beam file) is drawn. For the first event, the beam particle at the drawn position is taken. The following events get beam particles, which follow the previous within the list. Once, the end of the list is reached, beam particles from the beginning of the list are taken, and so on. For each event, a primary vertex is determined and the event generator is called.

The given event generator, takes the incoming beam particle as well as the proton target and starts to map out the kinematic properties of the final state particles. This is done in several steps. Each step can be described as a one-body → two-body (one particle decays into two daughter particles) or two-body → two-body (two particles scatter to two others, where the others relate to at least different kinematic properties) process. Focusing on the given reaction (see eq. (2.1)), the generator would first regard a two-body → two-body process, where the beam particle scatters off the proton target to the intermediate state X^- and the recoiling proton. The energies are determined according to the available phase space, while the emerging direction of the particles are weighted with the empiric t'-distribution[3] function, extracted by COMPASS, while analyzing the real data events.

$$\frac{dN}{dt'} = t' \exp^{-8.45\,\mathrm{GeV}^{-2} t'} \tag{4.1}$$

In addition, a specific range of the t' distribution and the mass of the produced X^- can be chosen within the settings file, if one wants to produce events with tight kinematic values.

The proton does not decay further and is therefore regarded as the first final state particle. X^- on the other hand needs to decay to either $\eta\pi^-$ or $\eta'\pi^-$ which is also given as an input to the generator, leading to the first one-body → two-body reaction. Here the event generator changes to the X^- rest frame and draws random energies, following the phase-space distribution, for the two outgoing particles. The particles' momentum direction vector $\vec{x}$ is determined via spherical coordinates, with the polar angle θ (running from 0 to π) and the azimuthal angle ϕ (running from 0 to 2π) drawn uniformly distributed.

$$\vec{x} = \begin{pmatrix} \sin\theta\cos\phi \\ \sin\theta\sin\phi \\ \cos\theta \end{pmatrix} \tag{4.2}$$

Now, the kinematic distribution of $\eta^{(\prime)}$ and π^- is boosted back to the lab frame. π^- is the second final state particle and $\eta^{(\prime)}$ decays to $\pi^-\pi^+\pi^0$, which is seemingly problematic because it is a one-body → three-body and not a one-body → two-body reaction. This problem is solved by

[3] For a definition of t' see eq. (2.8).

introducing an intermediate particle Y^+, leaving the chain to be

$$\eta^{(\prime)} \rightarrow \pi^- Y^+, \quad Y^+ \rightarrow \pi^+ \pi^0. \tag{4.3}$$

This is possible, because every one-body $\rightarrow$ n-body reaction can be split in (n-1) one-body $\rightarrow$ two-body reactions mathematically [1] and it is therefore irrelevant, how Y is formed, i.e. by what subset of particles. Nevertheless, it needs to be given as an input to the generator. Both of the resulting one-body $\rightarrow$ two-body reactions follow the same principle as explained above. π^- and π^+ are final state particles, leaving only one one-body $\rightarrow$ two-body reaction, namely $\pi^0 \rightarrow \gamma\gamma$. This again follows the same rules. After these steps, all kinematic properties of the six final state particles are known and given to TGEANT as outgoing particles from the primary vertex. They will be fed through the detector simulation and the simulated output of the detectors will be saved. In addition, the MC truth, i.e. the bare information on the beam particle and the final state particles, generated by the generator, are saved.

All final state particles are simulated at the primary interaction vertex. This is possible, because the lifetime of the intermediate particles, e.g. $\eta^{(\prime)}$ and X^-, is very small ($< 10^{-20}$ s [1]). They therefore decay after a very short distance (< 1 µm), even when one considers Lorentz boost.

Specifying the reaction in the TGEANT settings file

The generator accepts one input string and the reaction needs to be determined therewith. The input string for the given reaction and a specific range in (t', m_{X^-}) can look like

pi^- p >m[...:...]t'[...:...](pi^- eta(pi^- pi^+ pi^0(gamma gamma))) p.

">" separates the educts from the products. The particles are written in the same way, one would do in latex math mode. m[...:...] specifies the mass range of X^-, t'[...:...] the range of the t' distribution. (...) signals a closed group, e.g. pi^0(gamma gamma) specifies that π^0 has to decay to two photons. If three decay particles are given, the last two will form the intermediate state Y^+, e.g. eta(pi^- pi^+ pi^0) will be treated as $\eta \rightarrow \pi^- Y^+$, $Y^+ \rightarrow \pi^+ \pi^0$.

4.2 Reconstruction and analysis

After the simulation, TGEANT outputs the detector information as well as the MC truth, for each event, to a compressed data file. This file is then fed to CORAL (see sec. 3.2.1) as a MC input file. CORAL analyzes the detector information in a similar way as for real COMPASS data and outputs its results to an mDST file. The MC truth information is not used during CORAL but rather carried directly to the mDST file. Once the data is reconstructed with CORAL, it can be analyzed with PHAST (see sec. 3.2.2), which works similar as for the real data analysis. Small differences in the event selection will be pointed out in sec. 4.4. In addition, the MC truth can be analyzed and compared to the MC reconstructed.

TGEANT provides a quick analysis tool itself, called toolbox. Therewith, the detector information and MC truth can be looked at right after the TGEANT simulation.

4.3 Monte-Carlo data production at BlueWaters

Recently, the COMPASS data of the 2008 hadron run went through a new production. The alignment of the detectors as well as the description of the calorimeters was heavily improved and this yielded an increase in usable real data events of roughly 40%, leaving 162985 $\eta\pi^-$ and 54999 $\eta'\pi^-$ events in a mass range of 0.5 to 8 GeV and a t' range of 0.07 to 1.1 GeV^2 (see [10]). In order to determine, how many MC events should be generated, one needs to know how many events are necessary to describe the detector acceptance in the partial-wave analysis well. According to [21] roughly 10 times more accepted MC events than accepted real COMPASS events are necessary.

In sec. 4.4 one can see, that roughly 15% of the generated MC events survive the event selection, leaving a minimum of 10^7 generated MC events for the $\eta\pi^-$ final state alone. Generating 1000 MC events with TGEANT needs roughly 3 h on one CPU (Central Processing Unit) of a local computer at Bonn, leaving a total of 3×10^4 h, which is more than three years, to generate just the minimum of MC data, for just the $\eta\pi^-$ final state on one local machine. The reconstruction with CORAL and analysis with PHAST is not included in this time estimate.

The logical consequence is to move the MC data generation to a computer cluster. The COMPASS collaboration booked computing time at one of the biggest super computers in the world, namely Blue Waters. It is located at the National Center for Supercomputing Applications in Illinois (USA) and consist of 22 640 computing nodes [22]. Each node is a combination of 32 scheduling units [23], which means that up to 32 different jobs can be setup in parallel at each node. The COMPASS collaboration provides a script, which distributes a number of jobs, specified in some text file to the different scheduling units of one node. A few tests showed, that the time for one TGEANT job went down, if just 31 out of the 32 scheduling units were booked with TGEANT jobs and one was left free to perform background processes.

The generation of 31 000 TGEANT events seemed to take between 7 and 9 h on one Blue Waters node. This number of events rises from the fact, that one TGEANT job was scheduled to generate 1 000 MC events, but 31 jobs were sent in parallel to one computing node. In order to estimate the number of nodes needed for the MC data generation, one needs to look at the COMPASS data again.

The partial-wave analysis will be performed in 4 different t' slices[4], with an equal amount of events per t' slice and a little under 80 mass slices per t' slice. The amount of events present above a X^- mass of 3 GeV decreases significantly. Therefore, the constant mass slice width is increased from 40 MeV to 250 MeV upwards of an X^- mass of 3 GeV.

Two arguments were regarded while deciding for these ranges. First, one wants the analysis to be independent of m and t' and second, enough events need to be present per slice in order to analyze the data properly. These numbers of t' and m slices seem to satisfy both conditions.

The COMPASS data was split into the given slices and for each slice a number of nodes were booked, in order to produce enough MC events. See fig. 4.3 and 4.4 for the exact amount of nodes for the first t' slice. To keep it simple, no node was used for different slices, which leads to more generated MC events than originally proposed. In addition, a survive rate of 5% instead of 15% was regarded for the event selection. This is of course not a bad thing, since more events describe the

[4] The ranges are 0 to 0.150 GeV^2, 0.150 to 0.242 GeV^2, 0.242 to 0.393 GeV^2 and 0.393 to 5.392 GeV^2. The minimal/maximal value of t' emerges from the minimal/maximal value of t' found in the selected COMPASS data of the 2008 hadron run. These extreme values are possible due to some error in the reconstruction or selection. Physics wise, 0.07 GeV^2 should be the border on the lower edge and somewhat around 1 GeV^2 on the upper edge of t'.

detector acceptance better than less, and if one really wants to decrease the number of events one can do this much easier than producing new ones.

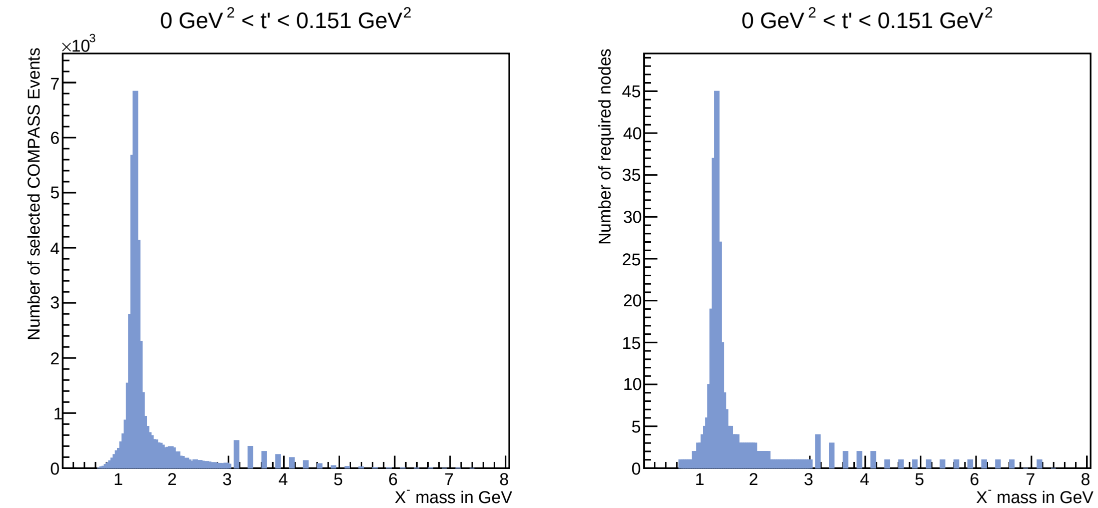

Figure 4.3: The number of real data events per mass slice in the first t' slice from 0 to 0.15 GeV^2 is shown in the left plot, as well as the resulting number of nodes used at the Blue Waters supercomputer for the $\eta\pi^-$ final state.

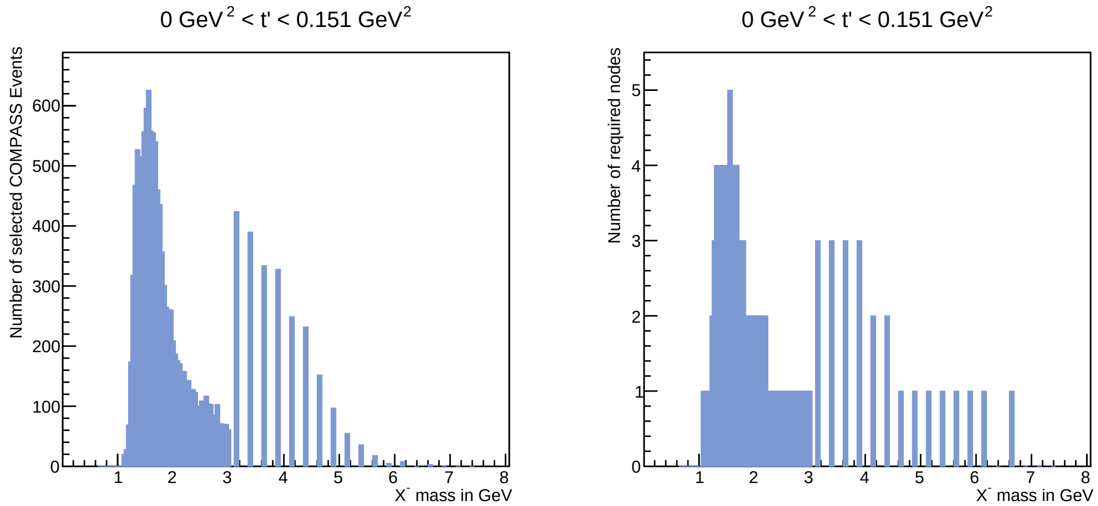

Figure 4.4: The number of real data events per mass slice in the first t' slice from 0 to 0.15 GeV^2 is shown in the left plot, as well as the resulting number of nodes used at the Blue Waters supercomputer for the $\eta'\pi^-$ final state.

After generating all MC events, the toolbox was used to merge TGEANTs output files in packs of 10^3 events per file. This was done because CORAL accepts just one MC input file per job, and it reconstructs events much faster than TGEANT simulates them. In praxis, 10^4 MC events took less then 3 h for CORAL to reconstruct on one scheduling unit at Blue Waters. This is a factor of 30 less in time, compared to the event simulation by TGEANT. After the reconstruction, the produced mDST files were merged by PHAST in order to produce mDST files of roughly 1.5 to 2 GB of size, leaving a relatively small number of mDST files, 825 for the $\eta\pi^-$ and 430 for the $\eta'\pi^-$ final state, to by analyzed. As a last step, the generated MC events were selected with PHAST (see sec. 4.4).

All generated files were transferred to a local backup machine at Bonn, in order to provide the possibility to perform new selections or even redo the reconstruction, if necessary.

4.4 Event selection

The event selection follows the main principles described in [10]. During this work, a new UserEvent function was developed, which is able to select MC events, as well as COMPASS events for the final state $\pi^-\pi^-\pi^+\gamma\gamma p$. The COMPASS event part serves as a cross-check to the event selection done in [10] and is heavily inspired by the same. For the MC part on the other hand, some adjustments had to be done. In the following, the different steps of the event selection are discussed and the differences emphasized.

The first step during any event selection is to satisfy the trigger condition. This means for the given data taking period, that the RPD needed to detect exactly one proton, the Beam Counter (upstream of the target) needs to see a beam, the Beam Killer (downstream of the target) does not see a beam and the veto system did not trigger (see sec. 3.1.5). For a more detailed description of the COMPASS detector parts see chapter 3. For the COMPASS events, the trigger information is coded in one single number, constructed by CORAL and the selection is therefore pretty easy, as one just needs to investigate this number. Unfortunately, this is not implemented for MC events. As a workaround, CORAL is given an option to save all hit information of the RPD, sandwich veto detector, Beam Counter and Beam Killers and during the event selection no hit in the Beam Killers and sandwich veto detector as well as exactly one hit in the Beam Counter and RPD is required on an event-by-event basis.

Once the trigger conditions are met, it is important to have exactly one best primary interaction vertex and it has to be inside the target area. Usually, the reconstruction part of the analysis takes place on the CORAL stage. The RPD is an exception to this, as PHAST analyses the hit pattern of the RPD, rather than CORAL. Consequently, no track of the recoil proton is present in the CORAL output mDST. Therefore, just three charged particles, namely two π^- and one π^+ need to leave the primary vertex. This means, that exactly three tracks need to leave the primary vertex and the charge sum of these tracks needs to be -1.

In order to determine the four-momentum of the charged particles, either the energy of the particles or the type needs to be known. Since in a later stage, a close cut to the three pion invariant mass will be applied (around the $\eta^{(\prime)}$ mass), just pions are possible as charged particles with a sufficent lifetime. The next particle on the mass scale, which lives long enough to be detectable inside the detector would be a kaon, but with its mass of 494 MeV [1] it is to heavy to decay from an $\eta^{(\prime)}$ with another kaon, which is needed due to flavor conservation, and pion[5]. This simplifies the charged particle reconstruction, as one can just assign the pion mass to the momentum direction vector of the track, which then determines the total four-momentum of the particle.

Next, the electromagnetic calorimeters are under investigation. Since the photons are chargeless, no track should be associated to a found calorimeter cluster. In addition, some energy and time cuts are applied, in order to separate background photons[6] from the final state photons. After all possible

[5] The pion is needed to conserve parity.

[6] Background photons can for example emerge from secondary processes, where particles scatter in material.

photons are found, just events with exactly two photons are excepted.

Now, all final state particles are found, but one has to make sure, that they did decay from η/η', in case of $\pi^-\pi^+\pi^0(\gamma\gamma)/\pi^-\pi^+\eta(\gamma\gamma)$ and π^0/η in case of $\gamma\gamma$. This is done by applying a rather thin cut around the invariant mass of the η/η' inside the invariant mass spectrum of the three pions and around the π^0/η mass inside the $\gamma\gamma$ invariant mass spectrum.

The resulting beam four-momentum is calculated, by taking the incoming track to the primary vertex as the momentum direction and the energy is calculated via the four-momentum of the state X^- and the masses of the involved particles, i.e. m_p for the proton mass, m_x for the mass of the intermediate state X^- and m_{π^-} for the pion mass. In the following, the beam is denoted by the index b, the target[7] as t, the recoil proton as r and the intermediate state X^- as x. From momentum conservation one can then deduce:

$$\begin{aligned} p_b + p_t &= p_x + p_r \\ p_r^2 &= \left(p_b + p_t - p_x\right)^2 \\ m_p^2 &= p_b^2 + p_t^2 + p_x^2 + 2p_bp_t - 2p_xp_t - 2p_bp_x \\ m_p^2 &= m_{\pi^-}^2 + m_p^2 + m_x^2 - 2E_bm_p - 2E_xm_p - 2E_bE_x + 2\vec{p}_b\vec{p}_x \\ m_p^2 &= m_{\pi^-}^2 + m_p^2 + m_x^2 - 2E_xm_p + 2E_b(|\vec{p}_b|\vec{p}_x + m_p - E_x) \\ E_b &= \frac{m_{\pi^-}^2 + m_x^2 - 2E_xm_p}{2(m_p - E_x + |\vec{p}_b|\vec{p}_x)} \end{aligned} \tag{4.4}$$

In addition an exclusivity cut is applied. This is a combined cut of the beam energy being around 191 GeV (see sec. 3.1.1) and the coplanarity angle $\Delta\phi$ being close to $\pm\pi$. Mathematically, $\Delta\phi$ should always be $\pm\pi$, but due to inaccuracies in the reconstruction, the four-momenta of the particles are not exact and therefore $\Delta\phi$ can differ from $\pm\pi$. $\Delta\phi$ is defined as

$$\begin{aligned} \Delta\phi &= \sphericalangle(\vec{p}_{X^-} \times \vec{p}_{\text{Beam}}, \vec{p}_{\text{Recoil}} \times \vec{p}_{\text{Beam}}) \\ &= \sphericalangle((\vec{p}_{\text{Beam}} + \vec{p}_{\text{Target}} - \vec{p}_{\text{Recoil}}) \times \vec{p}_{\text{Beam}}, \vec{p}_{\text{Recoil}} \times \vec{p}_{\text{Beam}}) \\ &= \sphericalangle(\vec{p}_{\text{Beam}} \times \vec{p}_{\text{Recoil}}, \vec{p}_{\text{Recoil}} \times \vec{p}_{\text{Beam}}) \\ &= \pm\pi \end{aligned} \tag{4.5}$$

while using momentum conservation

$$\vec{p}_{\text{Beam}} + \vec{p}_{\text{Target}} = \vec{p}_{\text{Recoil}} + \vec{p}_{X^-} \tag{4.6}$$

By applying this cut, the exclusivity of the final state is tested, hence the name of the cut. If one event would have one π^+, two π^-, one proton and three γ, instead of two, in the final state but for some reason, one of the photons was not reconstructed within the ECALs, then the event selection would not throw the given event. This is overcome by the exclusivity cut, as an additional particle would introduce a shift in the coplanarity angle.

For a detailed number of events which survived what cut, see tab. 4.1. Note, that not each event is reconstructed or simulated due to some errors, e.g. TGEANT did not find an interaction vertex inside

[7] Important to note, is that the target is at rest, i.e. its momentum vector is 0.

the target. Because of that, the generated number of events is not a multiple of 31 000.

Table 4.1: Number of events, which survived a given cut, for the $\eta\pi^-$ and $\eta'\pi^-$ final state

Cut	# Events ($\eta\pi^-$)	# Events in % ($\eta\pi^-$)	# Events ($\eta'\pi^-$)	# Events in % ($\eta'\pi^-$)
Generated events	37 199 674	100.00	15 119 717	100.00
Trigger cut	33 453 705	89.93	13 560 930	89.69
Primary vertex found	33 049 304	88.84	13 404 598	88.66
Target cut	31 804 795	85.50	12 921 243	85.46
3 charged particles	23 674 183	63.64	9 644 008	63.78
charge conservation	23 452 162	63.04	9 555 280	63.20
2 photons requirement	9 215 249	24.77	5 181 015	34.27
$\gamma\gamma$ mass cut	7 255 608	19.50	3 766 000	24.91
Exclusivity cut	5 658 620	15.21	2 801 838	18.53
$\pi^-\pi^+\gamma\gamma$ mass cut	5 459 790	14.68	2 766 581	18.30

The comparison between the event selection on the COMPASS data and the event selection in [10] is done in Appendix B. The final number of events for the $\eta^{(\prime)}\pi^-$ final state differ on a permil level. For the same diagrams, but concerning the MC data sample, see Appendix C.

4.5 Multidimensional Acceptance

The goal of the MC simulation is to describe the multidimensional acceptance of the detector in the given final state. As described in section 4.4, events that survived the given cuts were saved and therefore marked as accepted $\eta^{(\prime)}\pi^-$ events. The acceptance of the detector within different kinematic variables is than the ratio between generated and selected events. The accepted events within the scattering angles θ and ϕ of $\eta^{(\prime)}$ in the Gottfried-Jackson frame can be seen in fig. 4.6. Note that the $(\cos\theta,\ \phi)$ distribution was generated flat within the Gottfried-Jackson frame[8] (see fig. 4.5).

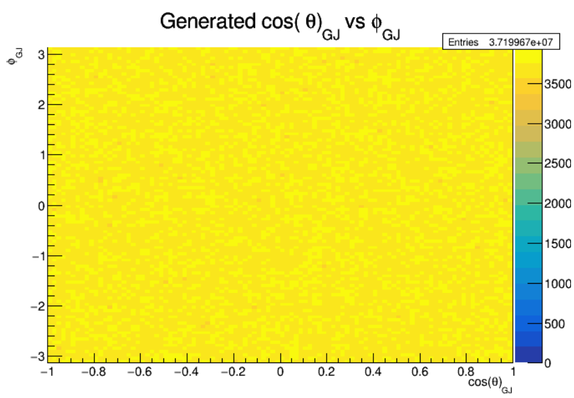

Figure 4.5: Shown is the generated distribution of $\cos\theta_{\mathrm{GJ}}$ and ϕ_{GJ} for the $\eta\pi^-$ final state.

[8] see sec. 2.2 for a definition of the Gottfried-Jackson frame

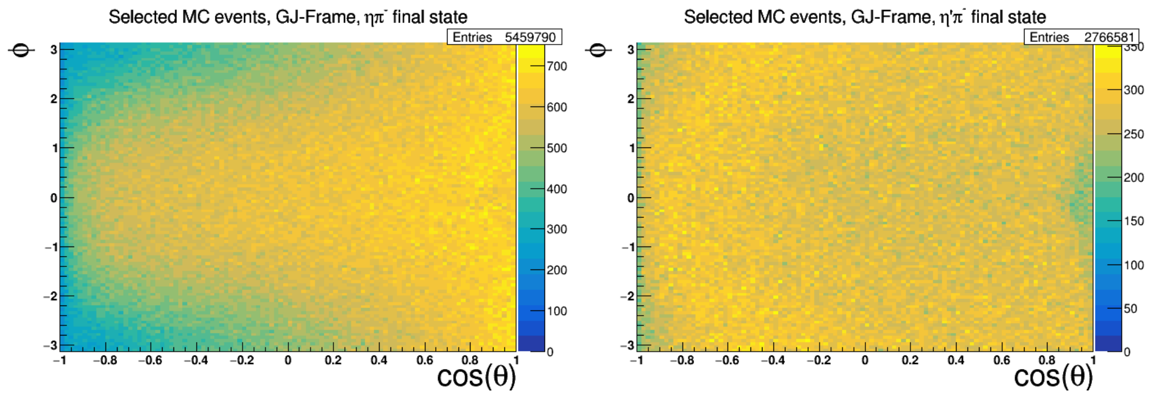

Figure 4.6: Shown is the distribution of $\cos\theta_{\mathrm{GJ}}$ and ϕ_{GJ} for the $\eta\pi^-$ final state (left) and the $\eta'\pi^-$ final state (right)

Focusing first on the accepted events of the $\eta\pi^-$ final state, within the GJ-angles $\cos(\theta)_{\mathrm{GJ}}$ and ϕ_{GJ}[9], one can see an acceptance drop for $\cos(\theta)_{\mathrm{GJ}} = -1$. This is due to the fact, that final state particles emerging of η particles with $\cos(\theta)_{\mathrm{GJ}} = -1$ have large polar angles in the lab frame, which then are simply not seen by the COMPASS detector. For η' on the other hand, this acceptance drop is way less drastic. η' is much heavier than η and therefore, $\cos(\theta)_{\mathrm{GJ}} = -1$ corresponds to much smaller polar angles in the lab frame. Hence, the final state particles lie more often within the acceptance of the detector. On the other hand, η' with $\cos(\theta)_{\mathrm{GJ}} = 1$, which correspond to final state particles produced very narrow to the beam axis, are accepted less. This is explained by looking at the detector setup. Each detector leaves a small hole for the beam, in order to minimize damage on the central detectors, as not every beam particle interacts with the target, which implies a high particle density near the beam axis. Hence, particles produced very narrow to the beam axis fly through these holes of the detectors and therefore cannot be detected.

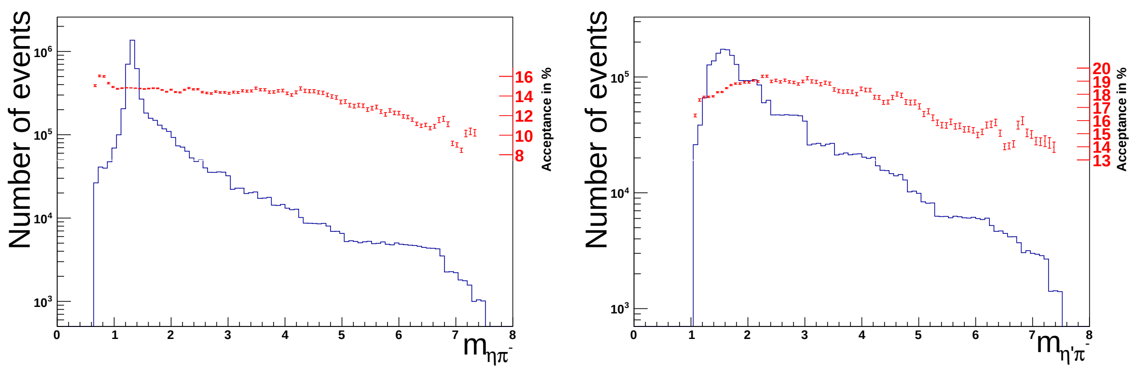

Figure 4.7: The acceptance of the Monte-Carlo events across the full mass spectrum of X^- is shown. On the left for $\eta\pi^-$ and on the right for $\eta'\pi^-$

The core acceptance to look at, is the one in the X^- mass spectrum, as can be seen in fig. 4.7.

[9] The ϕ angle within the GJ-Frame is often referred to as the Treiman-Yang angle. However, it will be called ϕ_{GJ} in this thesis.

Notice, that the acceptance to the $\eta'\pi^-$ final state is higher than for the $\eta\pi^-$ final state. Following the arguments given above, this is expected. One can also notice a little bump at low masses in the $\eta\pi^-$ spectrum, which is probably due to some near threshold effects. In addition, the whole detector acceptance decreases a bit to higher masses of X^-.

In the end, the selected MC events shall represent the detector acceptance in the partial-wave analysis. As described in sec. 4.2, the MC truth is carried through CORAL and PHAST, in addition to the detector information. This means, that there are now two options to choose from when trying to extract the information on the events, i.e. the MC truth and the reconstructed particles. In a way, the event selection confirms that the characteristics of the generated final state are accepted from the detector itself. In addition, the purpose of the event selection is to find the correct properties of the final state particles. But this is already known due to the MC truth information on the given event.

This leaves the MC truth information, to be the logical choice as the input to the partial-wave analysis.

4.6 CORAL adjustments for the MC simulation

One of the bigger differences from the reaction under investigation in this thesis to different COMPASS analyzes is the importance of the electromagnetic calorimeters. Here, it is important to reconstruct a final state with exactly two photons and the only way to do so, is via ECAL1 and ECAL2. Following this thought, the calorimeter description needs to be very accurate. During the CORAL reconstruction a shower (see sec. 3.1.3) fit, determines good photon clusters inside ECAL1 and ECAL2 respectively. The fit function used at COMPASS, was proposed by A. A. Lednev [24] and is shown in eq. (4.7), where x and y are the horizontal and vertical distance to the shower starting point and a_i and b_i are fit parameters, which describe the shape of the shower profile.

$$F(x, y) = \frac{1}{2\pi} \sum_{i=1}^{n} a_i \left(\arctan\left(\frac{x}{b_i}\right) + \arctan\left(\frac{y}{b_i}\right) + \arctan\left(\frac{xy}{b_i\sqrt{b_i^2 + x^2 + y^2}}\right)\right) + \frac{1}{4} \quad \text{with} \quad \sum_{i=1}^{n} a_i = 1 \tag{4.7}$$

Every calorimeter module has its own properties. Therefore, the shower parameters and order (n) needs to be determined for each module, e.g. GAMS, GAMS-R and Shashlik in the ECAL2 case, respectively. This was already done for the COMPASS data, but the MC data was generated with COMGEANT up until now. The calorimeter description of COMGEANT is not necessarily equal to that of TGEANT and the standard shower parameters for the 2008 hadron run at COMPASS might be inaccurate, while describing TGEANT simulated MC events.

First studies in this matter were performed by [25] and continued by [26]. In order to find good shower parameters, TGEANT was modified in a way, that just the electromagnetic calorimeter under investigation was activated and single photons were shot directly to specific calorimeter cells. This was done 1000 times per cell and the resulting events were then fitted with eq. (4.7). Within CORAL, a shower description up until $n = 3$ is supported. Regarding this, $n = 1, 2, 3$ was looked at in order to find the best description of the given showers.

Regarding the $\eta\pi^-$ final state, only 6.3% of the photons are measured in ECAL1. Furthermore, out of all measured photons in ECAL2, 5.9% were reconstructed in the GAMS-R and 0.8% in the

GAMS modules. The rest of the photons were measured in the Shashlik modules. Hence, the shower parameter studies were focused of the description of the Shashlik modules. The crucial question is, if the shower parameters need to change while regarding photons with different kinetic energies. This problem is addressed, by shooting single photons with different kinetic energies (10 to 100 GeV) onto an ECAL2 Shashlik cell and extracting the shower parameters. During the studies of [26], $n = 2$ was found to be sufficient in order to describe the shower. See tab. 4.2 for the different shower parameters.

Table 4.2: The shower parameters, determined by [26], are shown for different photon energies.

γ energy in GeV	a_1	b_1	a_2	b_2
10	1.0381 ± 0.0023	5.17 ± 0.03	$1 - a_1$	150 ± 22
20	1.0404 ± 0.0015	5.242 ± 0.020	$1 - a_1$	135 ± 9
30	1.0395 ± 0.0012	5.271 ± 0.016	$1 - a_1$	121 ± 6
40	1.0395 ± 0.0029	5.27 ± 0.05	$1 - a_1$	107 ± 12
50	1.0397 ± 0.0008	5.338 ± 0.013	$1 - a_1$	106 ± 4
60	1.0382 ± 0.0007	5.294 ± 0.011	$1 - a_1$	106.1 ± 2.7
70	1.0393 ± 0.0006	5.318 ± 0.011	$1 - a_1$	105.5 ± 2.5
90	1.0384 ± 0.0006	5.312 ± 0.009	$1 - a_1$	104.5 ± 2.1
100	1.0426 ± 0.0005	5.483 ± 0.009	$1 - a_1$	98.6 ± 1.8

These results leave the conclusion, that energy-dependent shower parameters are not necessary and the ones for 10 GeV will be used in the following.

The necessity to look into the shower description rised from the results of the MC data generation done during this work. As an example, ca. 60 000 selected events, with $0.150\,\text{GeV}^2 < t' < 0.242\,\text{GeV}^2$ and $1.3\,\text{GeV} < m_{\eta\pi^-} < 1.34\,\text{GeV}$ are taken of the generated MC data and analyzed separately. The two-photon mass spectrum for photons reconstructed only in the Shashlik modules of ECAL2 is shown in fig. 4.8.

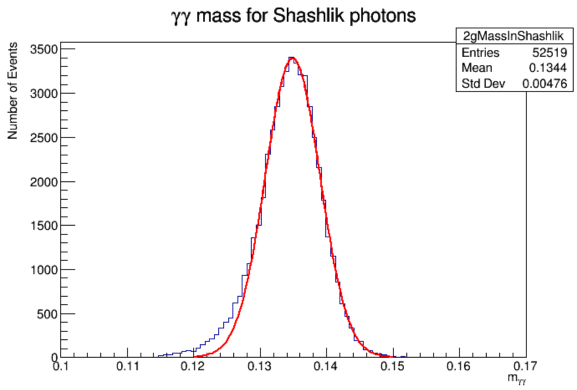

Figure 4.8: The spectrum of the two-photon mass, for photons reconstructed in the Shashlik modules of ECAl2, is shown. This data comes from the MC data generation done during this work, with $0.150\,\text{GeV}^2 < t' < 0.242\,\text{GeV}^2$ and $1.3\,\text{GeV} < m_{\eta\pi^-} < 1.34\,\text{GeV}$ for each event. A Gaussian function is fitted to the data points, which shows the asymmetry of the tho photon peak.

A symmetric peak around the π^0 mass is to be expected, with a Gaussian shape. This is the case, as the π^0 itself is a very narrow particle (width of a few eV [1]) and the spectrum should then just represent the detector resolution, for which a Gaussian should be sufficient to describe it.

Nevertheless, a clear asymmetry can be seen for the $\gamma\gamma$ mass distribution. This is illustrated, by the Gaussian function, which is fitted to a small region around the peak and then drawn for the full range of the diagram. Changing the shower parameters, this asymmetry shifts substantially (see fig. 4.9). The asymmetry shifted from being a tail to lower masses, to a tail to higher

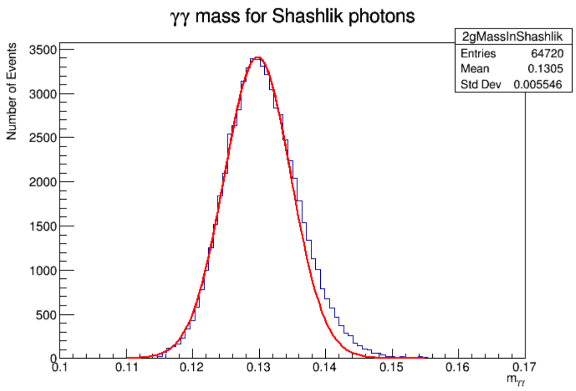

Figure 4.9: The spectrum of the two-photon mass, for photons reconstructed in the Shashlik modules of ECAL2, is shown. In order to reconstruct good photons, the new shower parameters are used. A Gaussian function is fitted to the data points, which shows the asymmetry of the two-photon peak.

masses. This data got reconstructed, by picking 600 000 MC events, generated with TGEANT, with $0.150\,\mathrm{GeV}^2 < t' < 0.242\,\mathrm{GeV}^2$ and $1.3\,\mathrm{GeV} < m_{\eta\pi^-} < 1.34\,\mathrm{GeV}$ and changing the shower parameters inside the CORAL settings to them for 10 GeV photons from tab. 4.2. One can see, that in addition to the different asymmetry, the peak position also changed. This comes from the fact, that a different shower profile leads to different calorimeter cells, which form one good photon cluster. Consequently, the energy of the cluster (photon) shifts. Inside CORAL, the `reserv` parameter adjusts for the energy calibration of the calorimeter cells.

$$E_{\text{final}} = \frac{E_{\text{measured}}}{\text{reserv}} \tag{4.8}$$

E_{measured} is the energy determined by the shower fit and E_{final} is the real energy of one photon. For this MC data, it is known, that the two photons should emerge from a π^0. Consequently, one can calculate the new `reserv` parameter by looking at the relative position of the two-photon peak to the nominal π^0 mass (134.977 MeV, see [1]). Four-momentum conservation dictates

$$\begin{aligned} p_{\pi^0}^2 &= \left(p_{\gamma_1} + p_{\gamma_2}\right)^2 \\ m_{\pi^0}^2 &= m_{\gamma_1}^2 + m_{\gamma_2}^2 + 2\left(E_{\gamma_1}E_{\gamma_2} - \vec{p}_{\gamma_1}\vec{p}_{\gamma_2}\right) \\ &= 2E_{\gamma_1}E_{\gamma_2}\left(1 - \cos\left(\theta_{\gamma_1\gamma_2}\right)\right) \end{aligned} \tag{4.9}$$

One can see, that the same change on E_{γ_1} and E_{γ_2} linearly leads to a change in m_{π^0}. This means, that the new `reserv` parameter can directly be determined from the two-photon mass spectrum. By fitting a Gaussian distribution with a polynomial background to the data in 4.9, the new `reserv` parameter can be extracted (see fig. 4.10).

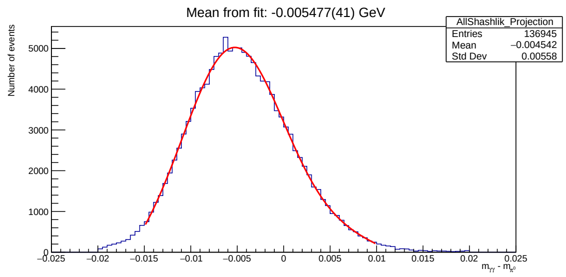

Figure 4.10: Determination of the new `reserv` parameter for the Shashlik modules of ECAL2. Notice, that the event number doubled. This is due to the fact, that one two-photon mass is shown for each photon, which doubles the amount of entries but does not effect the peak position. Also, the difference between the determined π^0 mass and the nominal π^0 mass rather than just the two-photon mass spectrum is shown.

The `reserv` parameters changes from 0.8977 to 0.8613 and the same data sample is analyzed again. The result is shown in fig. 4.11.

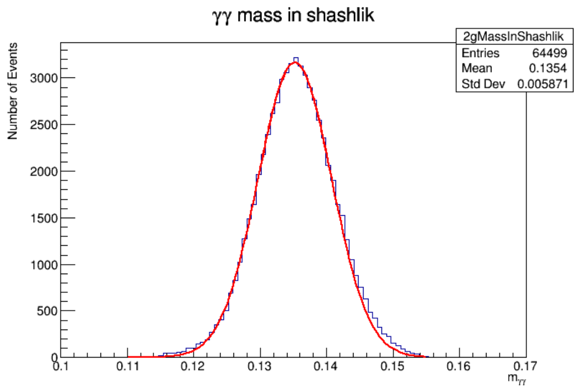

Figure 4.11: The two-photon mass diagram with the new `reserv`, as well as new shower parameters for photons, detected inside the Shashlik modules of ECAL2 is shown. The asymmetry of the peak is practically gone.

The asymmetry almost completely vanishes. This seems strange, because the change of the `reserv` parameter should just introduce a global shift within the mass. It should not change the characteristics of the spectrum itself. However, the event selection, used to select valid final state particles (see sec. 4.4), does not know if the pion mass spectrum is shifted or not. It simply applies the cut around the nominal π^0 mass, in order to find good events. After the application of the new shower parameters, this cut becomes not accurate anymore, meaning that the cut around the π^0 mass now cuts asymmetrically. This leads to an asymmetry within the two-photon mass spectrum. This error is of course ruled out, once the two-photon mass is shifted to the nominal π^0 mass, after the change of the `reserv` parameter.

Finally, one can say that the new shower parameters in combination with the new `reserv` parameter, are well suited to describe the characteristics of the Shashlik modules of ECAL2. In the future, this analysis should be carried onto the GAMS and GAMS-R modules of ECAL2, as well as the different modules of ECAL1, in order to describe the full calorimeter setup well, while regarding MC data, generated with TGEANT.

CHAPTER 5

Partial-wave analysis program

During this thesis a completely new partial-wave analysis (PWA) program for the $\eta^{(\prime)}\pi^-$ final state was developed. It is programmed in object-oriented C++ and controlled by a graphical user interface (GUI). The goal of this program is to perform a PWA in t' and $m_{\eta^{(\prime)}\pi^-}$ bins.

As explained in sec. 2.2, the negative log-likelihood function will be minimized to determine the different strengths of the given partial waves. Therefore, one has to give information about the different partial waves, which shall be included to the program. The general structure of the partial waves (see eq. (2.15)) is implemented and the quantum numbers l and m of the chosen partial waves need to be specified within the GUI. Information about the real data and Monte-Carlo events need to be present. They are required in form of a ROOT tree, where the four-momentum information of each final state particle, including the beam pion, is saved. The path to the two input files needs to be specified in the GUI.

For each event, the Gottfried-Jackson (GJ) angles θ_{GJ} and ϕ_{GJ} are extracted and saved within a given bin of t' and $m_{\eta^{(\prime)}\pi^-}$. The number of t' slices is to be determined within the GUI. The program will determine starting and end points of each slice in a way, that an equal amount of real data events is present in each t' slice. The starting and end points of the mass slices on the other hand, as well as the width of them can be set manually within the GUI. This is useful, as the analysis in many t' slices is used to disentangle the information on the resonant production from the non-resonant background while the amount of $m_{\eta^{(\prime)}\pi^-}$ slices on the other hand, as well as their ranges, determines how detailed specific mass regions are described, since the relative strength of each partial-wave is determined within each mass bin separately.

Next, some precalculations are performed, to reduce the time spend during the minimization of the negative log-likelihood function (see sec. 5.2), followed by the minimization itself (see sec. 5.3). The results, namely the strength of each partial wave in each bin, i.e. the complex coefficients, and their errors, determined by the fit, are saved in a ROOT tree.

5.1 The graphical user interface

A picture of the GUI can be seen in fig. 5.1. In the following, the different parts of the GUI are explained.

In the “General settings” region, one can turn some options on/off. They are briefly explained in tab. 5.1.

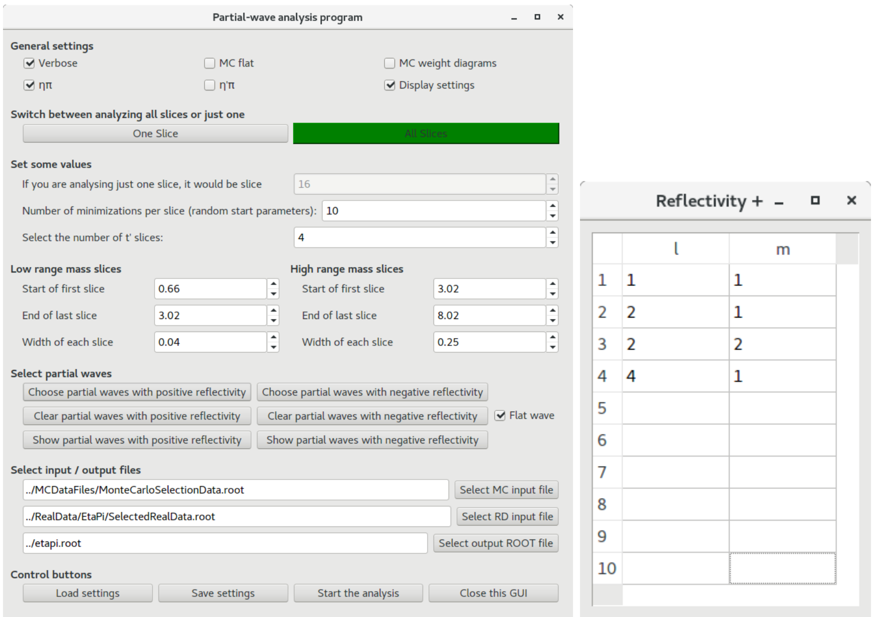

Figure 5.1: A picture of the graphical user interface, which controls the PWA program, is shown on the left. On the right, an example of the window is shown, where the partial waves with positive reflectivity are chosen.

Table 5.1: Brief explanation of the different general settings one can choose from in the GUI. Explained is the effect on the program, once the box, left to the given setting, is checked.

Setting	Brief explanation
Verbose	Information about the current state of the program is written to the terminal
MC weight diagrams	Create some diagrams, which serve as a check of the MC description (see sec. 5.4)
MC flat	Use 10^6 MC events, where the $\cos\theta_{GJ}$, ϕ_{GJ} distribution is flat across the whole phase space for each bin, instead of the TGEANT-generated MC events
$\eta\pi$	Consider the $\eta\pi^-$-final state
$\eta'\pi$	Consider the $\eta'\pi^-$-final state
Display settings	Information about the used settings is written to the terminal

Below the “General settings” one can choose between “One Slice” and “All slices”. The chosen one is marked in green. “All slices” means that the negative log-likelihood function is minimized for all t' and $m_{\eta^{(\prime)}\pi^-}$ slices independently, while “One Slice” just focuses on one particular $m_{\eta^{(\prime)}\pi^-}$ slice in the first t' slice. This is useful, if tests to the program need to be performed, or the strength of specific partial-waves in a small $m_{\eta^{(\prime)}\pi^-}$ range is under investigation and one wants to skip the other slices in order to save some time.

In the “Set some values” section of the GUI, one can determine the slice, which is analyzed when the option “One Slice” is used. in addition, the number of t' slices is set and how often each slice should be analyzed is determined. It is useful to do the minimization several times, with different randomly chosen start parameters, as the minimizer might not find the global minimum at the first minimization. In addition, due to the minimization procedure, sign ambiguities within the imaginary part of the coefficients can occur. Many minimization attempts will yield sufficient amount of data on the coefficients to correct for these ambiguities. See chapter 6 for more details on the matter.

As described in sec. 4.3, there are more events with low $m_{\eta^{(\prime)}\pi^-}$ mass and because of that, the data set is divided in a low and high mass region. For each region, the starting and end point of the mass slices can be chosen, as well as the slice width for each region. This is done in the “Low range mass slices” and “High range mass slices” section of the GUI.

As explained above, the characteristics of the partial waves, i.e. l and m, which are used to describe the data, are set in the “Select partial waves” section. The “Select partial waves ...” button opens the window shown on the right side of fig. 5.1, where l and m for the used partial waves with positive and negative reflectivity are determined. The $(l,\ m)$ combinations need to be in ascending order and the GUI will reject false inputs.

The ROOT files, which contain the MC and real data as well as the name and path to the output ROOT file, need to be determined. This is done in the “Select Files” section. One can enter the full / relative path manually or browse through the directories of the computer by clicking on the “Select ... file” buttons.

At last, there are the “Control buttons”. The given settings can be loaded and saved and the PWA program can be started or the GUI can be quit.

5.2 Precalculations

The COMPASS data as well as the MC data is stored as lab frame four-vector information in ROOT trees. They are read into the program and an event object (new C++ class) is created per MC and COMPASS event. There, t' and $m_{\eta^{(\prime)}\pi^-}$ is determined, the event is boosted to the Gottfried-Jackson frame and the needed θ_{GJ}, ϕ_{GJ} information are extracted. In principle, the negative log-likelihood function can be minimized now using equation (2.24) and the extracted Gottfried-Jackson angles, but this runs into a serious problem, as the calculation takes a lot of computing time and many minimization steps need to be performed per slice. In order to shorten the time that is needed per minimization step, it is useful to calculate every variable, which is not effected by the minimization procedure, beforehand.

Focusing first on the part which is described by the detector acceptance within the negative log-likelihood function (see eq. (2.24)) and inserting the definition of the intensity function (eq. (2.18)) for a given $(m_{\eta^{(\prime)}\pi^-}, t')$ bin one gets

$$\begin{aligned} N_e &= \iint \left(\sum_{\epsilon=+1,-1} \left| \sum_{lm} c^{\epsilon}_{lm} \Psi^{\epsilon}_{lm}(\theta,\phi) \right|^2 + |c_{\text{flat}}|^2 \right) \xi(\theta,\phi) \,\mathrm{d}\cos\theta \mathrm{d}\phi \\ &= \iint \left(\left| \sum_{lm} c^{+}_{lm} \Psi^{+}_{lm}(\theta,\phi) \right|^2 + \left| \sum_{lm} c^{-}_{lm} \Psi^{-}_{lm}(\theta,\phi) \right|^2 + |c_{\text{flat}}|^2 \right) \xi(\theta,\phi) \,\mathrm{d}\cos\theta \mathrm{d}\phi \end{aligned} \tag{5.1}$$

Now, one can calculate the absolute value squared of the intensity function for positive/negative reflectivity further, using basic definitions of matrices and the scalar product. In order to keep the notation short, l and m are combined to i and the reflectivity indication is dropped.

$$\begin{aligned} \left| \sum_i c_i \Psi_i(\theta,\phi) \right|^2 &= \left(\sum_i c_i \Psi_i(\theta,\phi) \right)^* \left(\sum_j c_j \Psi_j(\theta,\phi) \right) = \sum_i \sum_j c_i^* \Psi_i^*(\theta,\phi) \Psi_j(\theta,\phi) c_j \\ &= \sum_i \sum_j c_i^* B_{ij}(\theta,\phi) c_j = \sum_i c_i^* \sum_j B_{ij}(\theta,\phi) c_j \\ &= \sum_i c_i^* \left(B(\theta,\phi) \cdot \vec{c} \right)_i = \left(\vec{c}^{\,*} \right)^T \cdot B(\theta,\phi) \cdot \vec{c} \end{aligned} \tag{5.2}$$

The * denotes the complex conjugate, and T the transposed of a vector. The matrix $B(\theta, \phi)$ is given by

$$B = \begin{pmatrix} \Psi_1^*(\theta,\phi)\Psi_1(\theta,\phi) & \Psi_1^*(\theta,\phi)\Psi_2(\theta,\phi) & \dots & \Psi_1^*(\theta,\phi)\Psi_n(\theta,\phi) \\ \Psi_2^*(\theta,\phi)\Psi_1(\theta,\phi) & \ddots & & \vdots \\ \vdots & & \ddots & \Psi_{n-1}^*(\theta,\phi)\Psi_n(\theta,\phi) \\ \Psi_n^*(\theta,\phi)\Psi_1(\theta,\phi) & \dots & \Psi_n^*(\theta,\phi)\Psi_{n-1}(\theta,\phi) & \Psi_n^*(\theta,\phi)\Psi_n(\theta,\phi) \end{pmatrix} \tag{5.3}$$

where n is the number of partial waves. One B matrix exists per reflectivity and they do not interfere with each other.

The detector acceptance is described by MC data, i.e. a data sample which is generated by performing the same experiment (calculating the final state particles from a given initial state, while drawing the kinematic distributions at random) many times. This means, that the law of large numbers can be applied while solving the integral (5.1). In probability theory, this law states that a large number of trials should yield a result close to the expectation value. Consequently, one can rewrite (5.1) by using this and (5.2). $B_{\pm}$ denotes the B matrix for a given set of partial waves with positive / negative reflectivity, used in the analysis.

$$
\begin{aligned}
N_e &= \frac{V}{N_{\mathrm{MC}}} \sum_{k=1}^{N_{\mathrm{MC}}} \left(\left((\vec{c}_+^*)^T \cdot B_+(\theta_k, \phi_k) \cdot \vec{c}_+ + (\vec{c}_-^*)^T \cdot B_-(\theta_k, \phi_k) \cdot \vec{c}_- + |c_{\mathrm{flat}}|^2 \right) \xi(\theta_k, \phi_k) \right) \\
&= (\vec{c}_+^*)^T \cdot \left(\frac{V}{N_{\mathrm{MC}}} \sum_{k=1}^{N_{\mathrm{MC}}} B_+(\theta_k, \phi_k) \xi(\theta_k, \phi_k) \right) \cdot \vec{c}_+ + (\vec{c}_-^*)^T \cdot \left(\frac{V}{N_{\mathrm{MC}}} \sum_{k=1}^{N_{\mathrm{MC}}} B_-(\theta_k, \phi_k) \xi(\theta_k, \phi_k) \right) \cdot \vec{c}_- \\
&\quad + \frac{V}{N_{\mathrm{MC}}} \sum_{k=1}^{N_{\mathrm{MC}}} \xi(\theta_k, \phi_k) |c_{\mathrm{flat}}|^2
\end{aligned}
\tag{5.4}
$$

Note that V is the total phase-space volume and N_{MC} is the total number of MC events.

$$
V = \iint \mathrm{d}\cos(\theta) \mathrm{d}\phi = 4\pi \tag{5.5}
$$

The acceptance function $\xi(\theta, \phi)$ is still unknown. This problem is solved rather easily, as on an event-by-event basis, a MC event is either accepted or rejected by the event selection. Following this argument, the sum over all MC events is reduced to the sum over all accepted MC events, where the acceptance function evaluates to 1. This leaves the number of expected events to be

$$
N_e = (\vec{c}_+^*)^T \cdot A_+ \cdot \vec{c}_+ + (\vec{c}_-^*)^T \cdot A_- \cdot \vec{c}_- + A_{\mathrm{flat}} |c_{\mathrm{flat}}|^2 \tag{5.6}
$$

where

$$
A_\pm = \frac{4\pi}{N_{\mathrm{MC}}} \sum_{k=1}^{N_{\mathrm{MC}}^{\mathrm{acc}}} B_\pm(\theta_k, \phi_k) \quad \text{and} \quad A_{\mathrm{flat}} = 4\pi \frac{N_{\mathrm{MC}}^{\mathrm{acc}}}{N_{\mathrm{MC}}} \tag{5.7}
$$

The matrices $A_\pm$ are completely independent of the coefficients $c_\pm$ and can be precalculated before the minimization procedure, which leaves the calculation of the expected number of events to be a rather fast procedure, as it is now independent of the number of MC events and consist just of some simple matrix and vector multiplication.

Secondly, one can look at the last part of the negative log-likelihood function, which is calculated using the COMPASS data. It shall be called S in the following.

$$
S = \sum_{k=1}^{N_C} \ln I(\theta_k \phi_k) \tag{5.8}
$$

Unfortunately, the sum over all COMPASS events N_C, with the final state $\eta^{(\prime)}\pi^-$, is outside of the logarithm. This means that, in contrast to the first part of the negative log-likelihood function, the sum over all events can not be precalculated. Nevertheless, the intensity function per event can be evaluated beforehand in a similar way, as shown above.

$$
S = \sum_{k=1}^{N_C} \ln \left((\vec{c}_+^*)^T \cdot B_+(\theta_k, \phi_k) \cdot \vec{c}_+ + (\vec{c}_-^*)^T \cdot B_-(\theta_k, \phi_k) \cdot \vec{c}_- + |c_{\mathrm{flat}}|^2 \right) \tag{5.9}
$$

Again, $B_\pm$ can be calculated before the fit, while the multiplication with the changing coefficients $c_\pm$ and the summation over all events needs to be performed for each minimization step individually.

The negative log-likelihood function, as it will be minimized per t' and $m_{\eta^{(\prime)}\pi^-}$ slice now reads

$$\begin{aligned} -\ln\mathcal{L} = &(\vec{c}_+^{\,*})^T \cdot A_+ \cdot \vec{c}_+ + (\vec{c}_-^{\,*})^T \cdot A_- \cdot \vec{c}_- + A_{\text{flat}}|c_{\text{flat}}|^2 \\ &- \sum_{k=1}^{N_C} \ln\left((\vec{c}_+^{\,*})^T \cdot B_+(\theta_k, \phi_k) \cdot \vec{c}_+ + (\vec{c}_-^{\,*})^T \cdot B_-(\theta_k, \phi_k) \cdot \vec{c}_- + |c_{\text{flat}}|^2\right) \end{aligned} \tag{5.10}$$

5.3 PWA fit

The partial-wave fit is performed with ROOT, via the ROOT::Math::Minimizer class. The minimizer type MINUIT2 together with the MIGRAD algorithm is chosen[1]. The negative log-likelihood function (2.24) is given to the minimizer as well as the number of parameters, which will be two per coefficient, i.e. per partial wave, minus one per different reflectivity. Two because the coefficients are complex hence, the real and imaginary part are both free parameters. In order to fix the global phase, the first coefficient, i.e. the one corresponding ot the lowest l, m, of each reflectivity block is chosen to be real[2]. Three partial waves with positive and three with negative reflectivity would yield 11 parameters. Five for $\epsilon = +1$, five for $\epsilon = -1$ and one for the flat wave.

After the minimization of the negative log-likelihood function (see eq. (2.24)), the covariance matrix, which contains the information on the errors of the parameters, as well as the parameters itself are saved within the PWA program.

In order to identify how many events are represented by each partial wave, a normalization of the complex coefficients needs to be performed according to

$$\sum_{k=1}^{N} I(\theta_k \phi_k) \stackrel{!}{=} N \tag{5.11}$$

where N is the number of real data events in the given $(m_{\eta^{(\prime)}\pi^-},\ t')$ bin and $I(\theta_k \phi_k)$ is the intensity per event (see eq. (2.18)) evaluated with the determined complex coefficients by the fit. This means, that the real and imaginary part of each coefficient is scaled by

$$\sqrt{\frac{N}{\sum_{k=1}^{N} I(\theta_k \phi_k)}} \tag{5.12}$$

while the entries in the covarianz matrix are scaled with the square of that.

[1] See [27] for a detailed documentation on the ROOT Minuit2 package.

[2] This has to be done for every new reflectivity block, as partial-waves with different reflectivity do not interfere.

5.4 MC weight diagrams

From eq. (5.6) one can see, that the total number of expected events N_e is given as the sum over all MC events, where each MC event corresponds to the sum with a weight ω_k of

$$\omega_k = (\vec{c}_+^*)^T \cdot \frac{4\pi}{N_{\text{MC}}} B_+(\theta_k, \phi_k) \cdot \vec{c}_+ + (\vec{c}_-^*)^T \cdot \frac{4\pi}{N_{\text{MC}}} B_+(\theta_k, \phi_k) \cdot \vec{c}_- + 4\pi \frac{N_{\text{MC}}^{\text{acc}}}{N_{\text{MC}}} |c_{\text{flat}}|^2 \tag{5.13}$$

This means, that one can get a good handle on the quality of the MC data, as well as the sufficiency of the given partial-wave sample, for the description of the given real data, while histogramming any other quantity, where each event is weighted with the corresponding ω_k. As an example, one could plot $\cos\theta_{\text{GJ}}$ for each MC event with the given weight, as well as for each real data event and one should see differences on the statistical level if the MC data sample describes the detector acceptance well.

CHAPTER 6

Results of the analysis

The partial-wave analysis is performed for the $\eta\pi^-$ and $\eta'\pi^-$ final state. The goal of the analysis is, to determine the relative strength of given partial waves within the data set. First of all, the partial-wave set needs to be determined to describe the data. It is known from [1, 28] that the resonance states $a_2(1320)$, within the D-wave ($l = 2$), and $a_4(2040)$, within the G-wave ($l = 4$), are build by the $\eta^{(\prime)}\pi^-$ system. In addition, the search for an exotic meson in the P-Wave ($l = 1$) is on the table. All these resonant productions are considered to be produced via natural exchange, i.e. these waves are within positive reflectivity. Since the number of expected events decreases with increasing m, in general only waves with $m = 1$ are considered. To be consistent with the previous analysis done in [28], the $l = 2,\ m = 2$ D-wave is also included in the analysis of the $\eta\pi^-$ final state. Therefore, these partial waves should be present within the analysis.[1]

In order to catch all background processes, all negative-reflectivity waves up until $l = 2,\ m = 1$ are included as well, although they are expected to be heavily suppressed as no unnatural exchange is to be expected within diffractive scattering.

First of all, one can look at the $\cos\theta_{\mathrm{GJ}}$, m_{X^-} distribution of the COMPASS data in both final states (see fig. 6.1 and fig. 6.2).

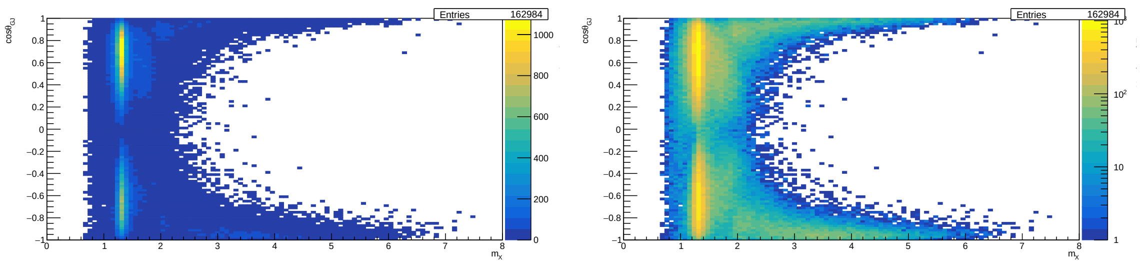

Figure 6.1: $\cos\theta_{\mathrm{GJ}}$, m_{X^-} distribution for the $\eta\pi^-$ final state. The diagram shown on the right is in log scale.

A symmetric structure within the distribution of $\cos\theta_{\mathrm{GJ}}$, m_{X^-} in the $\eta\pi^-$ final state is visible. In addition, a double peak structure at 1.3 GeV can be seen, which corresponds to the $a_2(1320)$ resonance, in a D-wave. In the logarithmic representation of the diagram, a quadruple peak structure can be

[1] From eq. (2.12) it becomes clear, that no partial wave with $m < 0$ is possible. In addition no partial wave with positive reflectivity and $m = 0$ is possible due to eq. (2.15)

seen at about 2 GeV, which corresponds to the $a_4(2040)$, in a G-wave. Note that the number of peaks directly points to the order of orbital angular momentum of the partial wave, in which the resonances should be observed. From these pictures alone, one can therefore expect to see a very prominent peak near 1.3 GeV in the $\eta\pi^-$ D-wave and a peak of less strength around 2 GeV in the $\eta\pi^-$ G-wave.

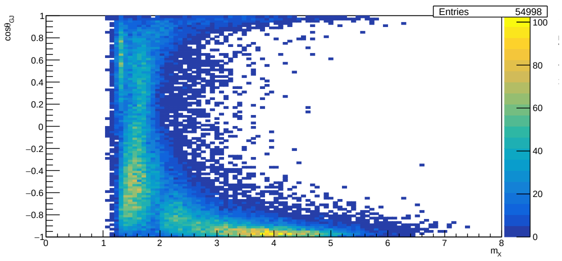

Figure 6.2: $\cos\theta_{\mathrm{GJ}}$, m_{X^-} distribution for the $\eta'\pi^-$ final state

The $\cos\theta_{\mathrm{GJ}}$, m_{X^-} distribution in the $\eta'\pi^-$ final state on the other hand is highly asymmetric. A high density near 1.3 GeV in the negative $\cos\theta_{\mathrm{GJ}}$ region is visible, which changes very promptly with increasing mass, until a peak structure near 1.5 GeV at negative $\cos\theta_{\mathrm{GJ}}$ values emerges. This hints to rapid phase motion between the D-wave and the P-wave as one can see below in the partial-wave analysis results of the $\eta'\pi^-$ final state. The asymmetric behavior, where angles with $\cos\theta_{\mathrm{GJ}} < 0$ are preferred in contrast to angles with $\cos\theta_{\mathrm{GJ}} > 0$ is explained by the acceptance of the detector as shown in sec. 4.5.

6.1 Partial-wave analysis in the $\eta\pi^-$ final state

In order to be consistent with the previous analysis done in [28], one shall look at the results of the partial-wave analysis of the $\eta\pi^-$ final state first, where the P-wave ($l = 1,\ m = 1$), D-waves ($l = 2,\ m = 1$ and $l = 2,\ m = 2$) and G-wave ($l = 4,\ m = 1$) are considered for natural exchange, i.e. positive reflectivity. In addition, the data is not split into t' slices up to now (see fig. 6.3). Inside the diagram, the letters P, D and G signal the given l and the amount of "+" next to the letters signal the order of m. Each diagram consist of the result of the data of 10 independent fit attempts all plotted on top of each other, while only fit results which correspond to the global minimum of the negative log-likelihood function within these attempts are displayed[2]. This behavior is true for all plots to come.

On the diagonal, the intensities of the given partial waves are displayed, from top left to bottom right in ascending order of $l,\ m$. The intensity of a given wave is defined as in eq. (2.18) with the exception, that just this wave participates.

$$I_i = \left| c_i \Psi_i \right|^2 \tag{6.1}$$

where i determines the given partial wave, c_i the complex coefficient determined by the fit (see sec. 5.3) and Ψ_i is the given partial wave as in eq. 2.15 evaluated for each event. In addition, the interference

[2] The accepted range for a minimum to be at the global minimum is ±0.01 %, relative to the global minimum.

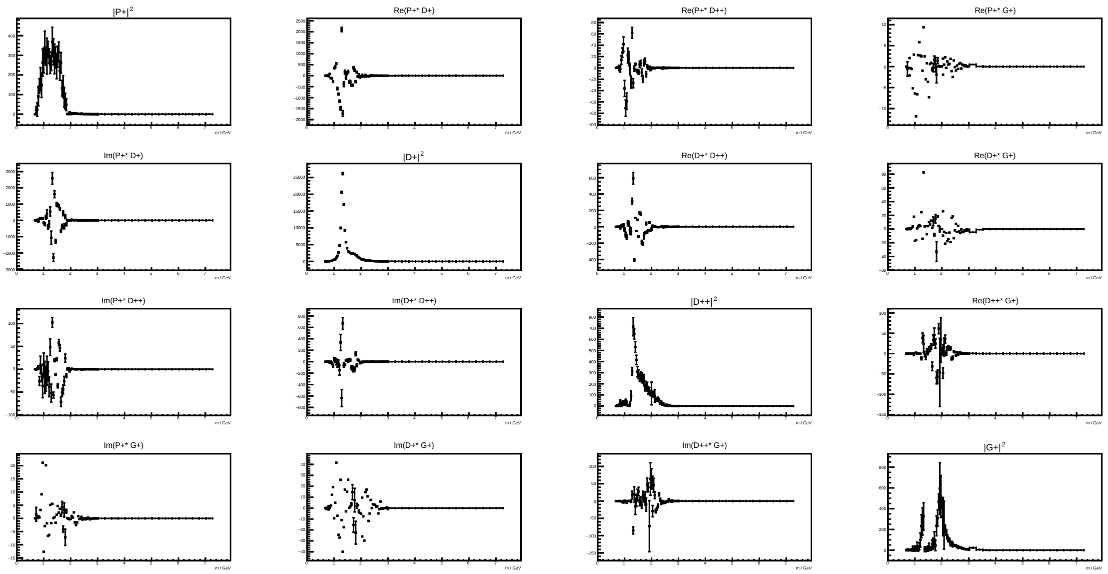

Figure 6.3: Results of the PWA for the $\eta\pi^-$ final state, for the partial waves with positive reflectivity. On the diagonal, the intensity of the given wave is shown. The imaginary part of the interference is shown on the bottom off-diagonals and the real part of that on the top off-diagonals.

between two partial waves F_{ij} can be defined as

$$F_{ij} = (c_i \Psi_i)^* \cdot c_j \Psi_j \tag{6.2}$$

where * denotes the complex conjugate. Note, that the interference between the partial wave i with itself yields the intensity. There are in principle three ways of displaying the interference, as this is a complex number. One can look at the real, imaginary part and the phase. It is in general more useful to look at the phase, as rapid motions in the same yield information about resonant states.

Nevertheless, in order to be consistent with [28], the real (top right) and imaginary (bottom left) parts of the interference of two partial waves are displayed on the off-diagonals of fig. 6.3. For example in the top left corner is the intensity of the $\eta\pi^-$ P-wave and diagonally below the intensity of the $\eta\pi^-$ D-wave. This leaves the first diagram in the second row to be the imaginary part of the interference of the P-wave and the D-wave.

In addition, one can look at the intensities of the unnatural waves as displayed in fig. 6.4. Here, the intensity increases above a mass of 2 GeV. From this it becomes clear, that the given set of partial waves did not describe the data well for high masses, as the fit focuses on the background waves for higher masses. One possible solution to this problem is to include waves with higher l, as they should describe higher masses of $m_{\eta^{(\prime)}\pi^-}$.

One unexpected result is, that the intensity of the flat wave is non-existent across all masses. This could only be the case, if the data set is purely consisting of $\eta\pi^-$ final state events, which is very unlikely. Hence, this hints to some error in the fit, which could not be solved up until now. Nevertheless, these diagrams can be compared to [28] and similar features are seen. This will be described closer while looking at the low mass region in particular down below.

From now on, only the phase between the given partial waves and the intensities are shown. The

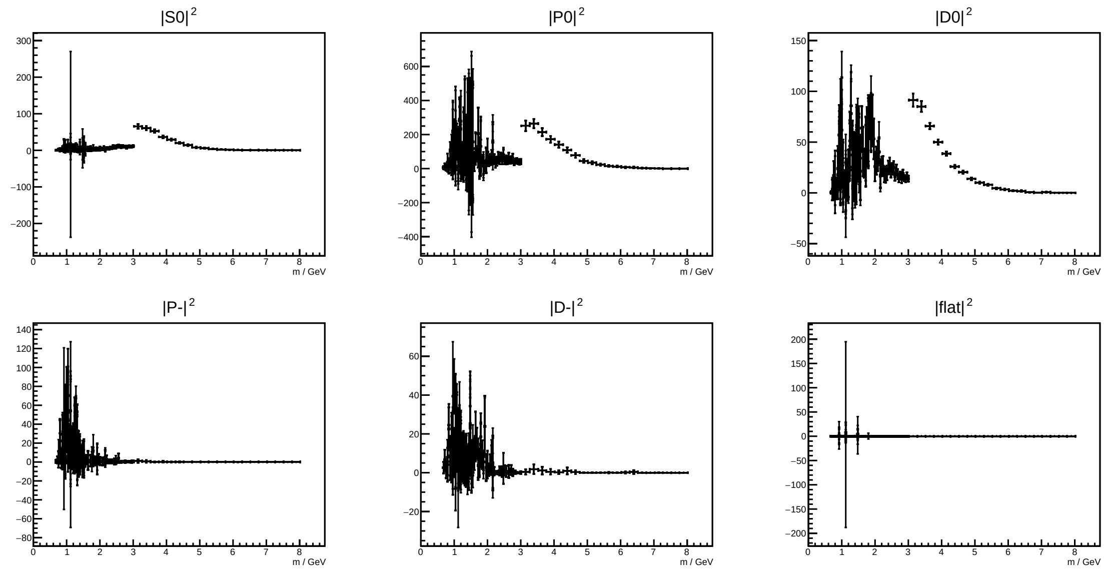

Figure 6.4: Results of the PWA for the $\eta\pi^-$ final state, for the partial waves with negative reflectivity and the flat wave. Displayed are the intensities of the given partial waves.

phases will be on the off-diagonals and the intensities on the diagonal.

In fig. 6.5 the same data as in fig. 6.3 is displayed but with the phases and intensities instead of the real, imaginary parts and intensities. On first sight, a rather interesting feature is seen above a mass of 2 GeV. The phases seem to be out of control. This is due to the fact, that the different intensities are near zero and the algorithm, i.e. `atan2(imaginary(`F_{ij}`), real(`F_{ij}`))`, which determines the phase, highly depends on the sign of `real(`F_{ij}`)` and `imaginary(`F_{ij}`)`. Therefore, all the phase motions above 2 GeV can be neglected.

Finally, in fig. 6.6, the low mass region of the fit results is displayed for the partial waves with positive reflectivity in the $\eta\pi^-$ final state. Looking first at the intensities of the given partial waves, a clear $a_2(1320)$ peak at 1.3 GeV is visible in the D-wave, as predicted above. In addition, a broad resonance like structure is seen in the P-wave and the $a_4(2040)$ can be detected in the G-wave. However, one needs to note, that the relative strength between the different waves is significant, as the spectrum is heavily dominated by the D-wave and the P-wave intensity is even below that from the D-wave with $m = 2$. The resonance behavior is underlined by the fact, that the phase motion of the D-wave (at about 1.3 GeV) and the G-wave (at about 2 GeV) changes rapidly. An other interesting feature are the sign ambiguities, seen in the phase diagrams. The fit does not determine the sign of the imaginary part of the coefficients. This makes it possible for the phase with a value x to be $+x$ or $-x$, for different fit attempts. These ambiguities can be solved by choosing the sign of the imaginary parts for every wave. However, this still needs to be done.

In fig. 6.7, 6.8, 6.9 and 6.10, the intensity and phase diagrams for the different t' slices are shown.

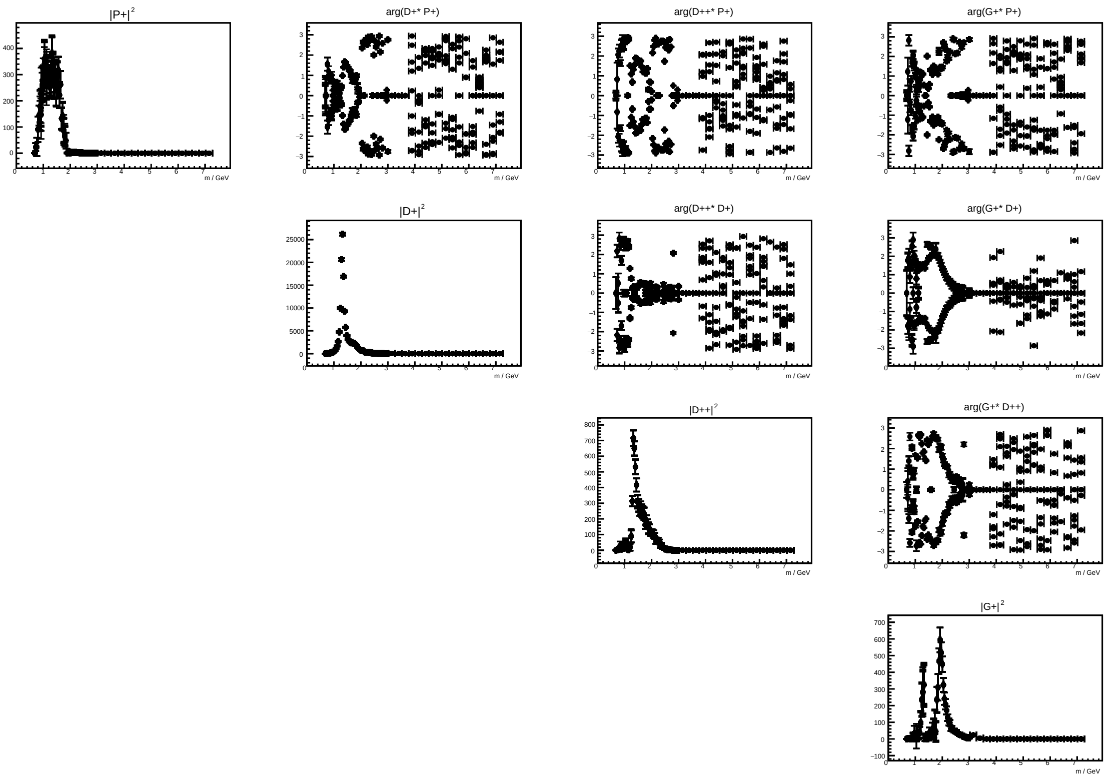

Figure 6.5: Results of the PWA for the $\eta\pi^-$ final state for positive reflectivity waves. Analyzed is the full data sample, in the full t' range. On the diagonal, the intensity of the given partial wave is displayed, while the relative phase between the partial waves are shown on the off-diagonals.

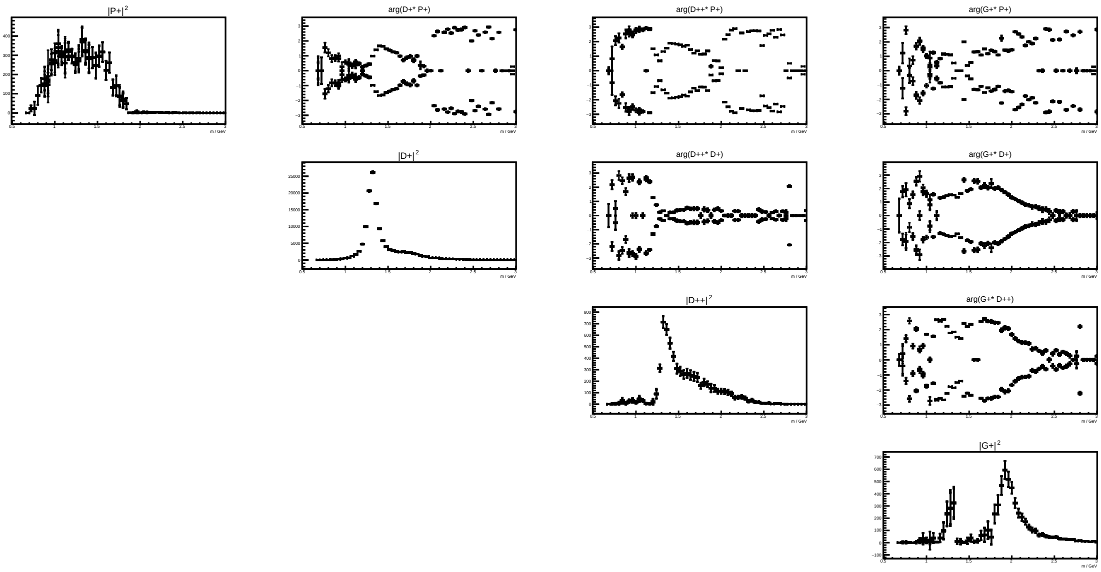

Figure 6.6: Results of the PWA for the $\eta\pi^-$ final state for positive reflectivity waves. Analyzed is the full data sample, in the full t' range and a closer look to masses below 3 GeV is shown. On the diagonal, the intensity of the given partial wave is displayed, while the relative phase between the partial waves are shown on the off-diagonals.

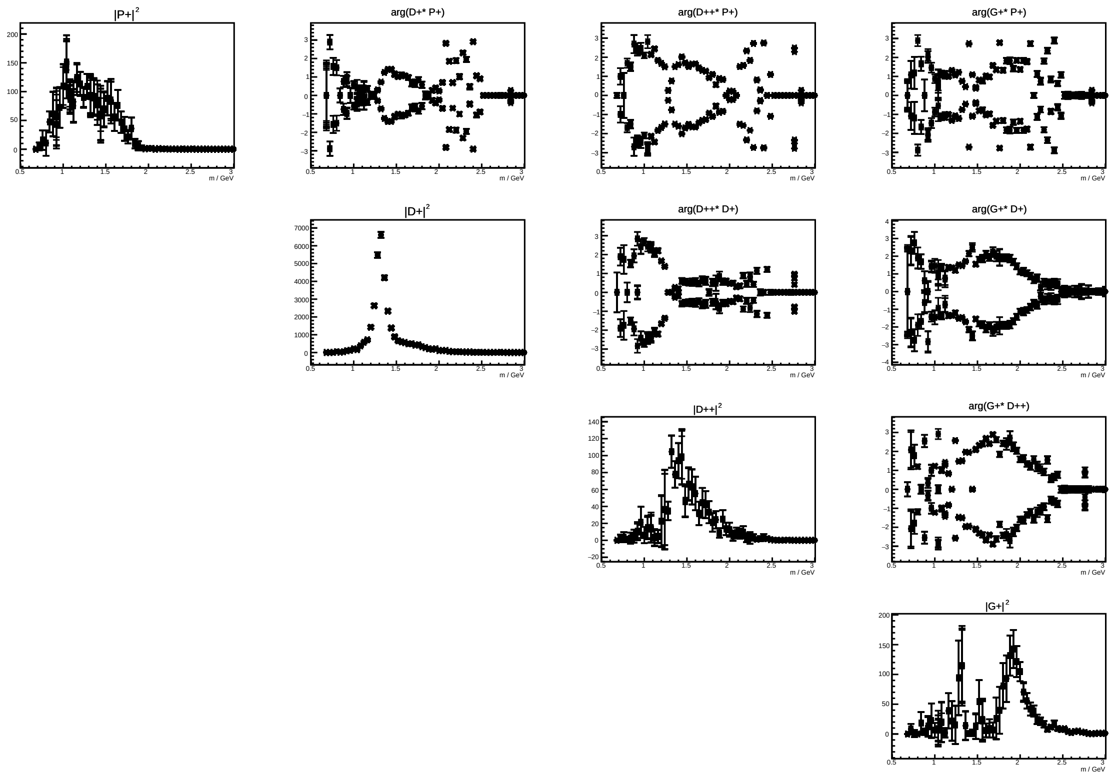

Figure 6.7: Results of the PWA for the $\eta\pi^-$ final state for positive reflectivity waves. Analyzed are the events with $0\,\mathrm{GeV}^2 < t' < 0.150\,\mathrm{GeV}^2$. On the diagonal, the intensity of the given partial wave is displayed, while the relative phase between the partial waves are shown on the off-diagonals.

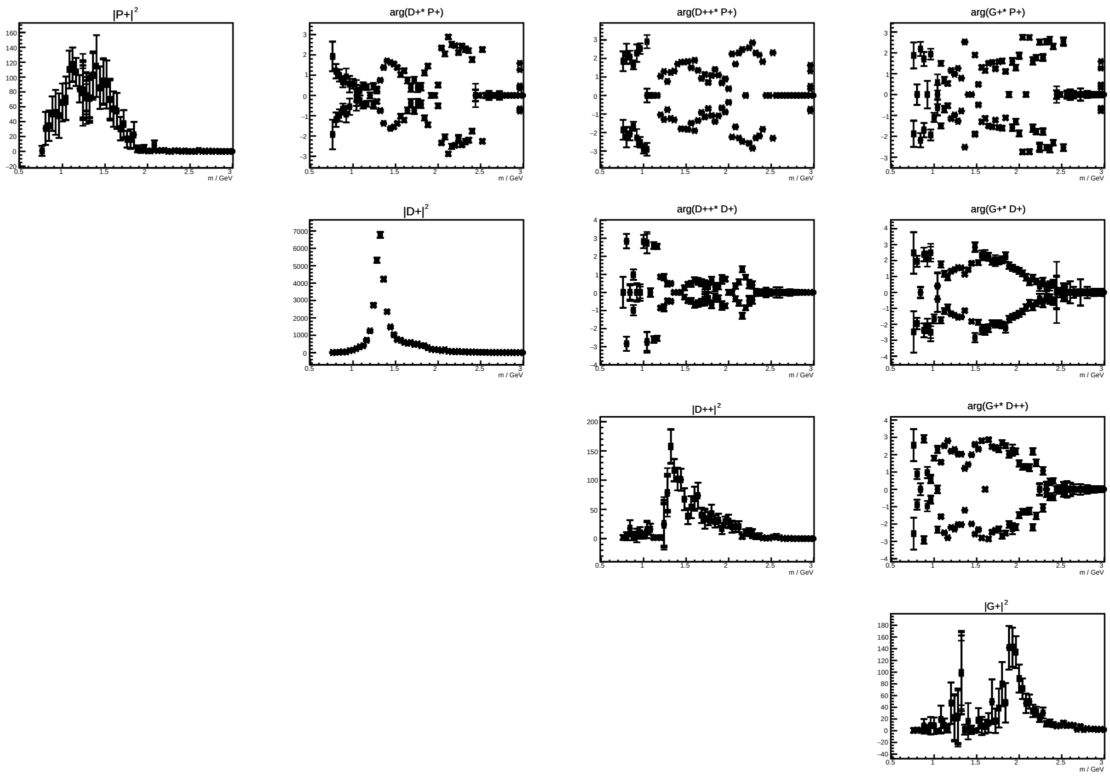

Figure 6.8: Results of the PWA for the $\eta\pi^-$ final state for positive reflectivity waves. Analyzed are the events with $0.150\,\mathrm{GeV}^2 < t' < 0.242\,\mathrm{GeV}^2$. On the diagonal, the intensity of the given partial wave is displayed, while the relative phase between the partial waves are shown on the off-diagonals.

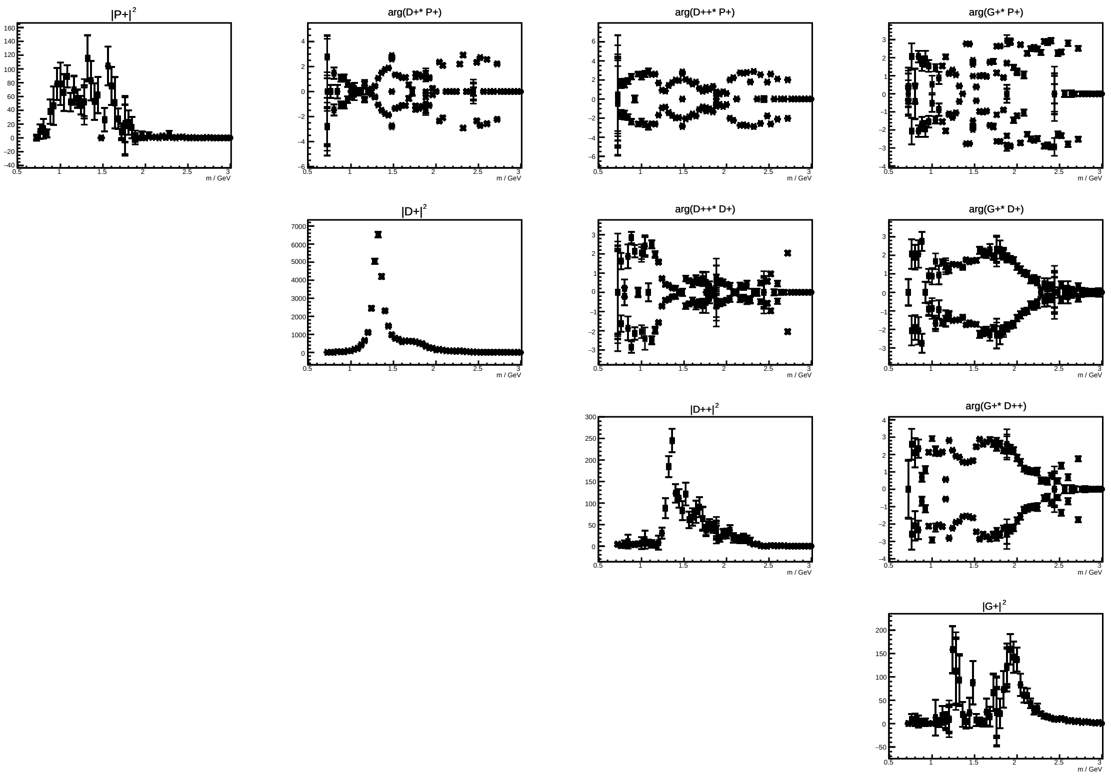

Figure 6.9: Results of the PWA for the $\eta\pi^-$ final state for positive reflectivity waves. Analyzed are the events with $0.242\,\mathrm{GeV}^2 < t' < 0.393\,\mathrm{GeV}^2$. On the diagonal, the intensity of the given partial wave is displayed, while the relative phase between the partial waves are shown on the off-diagonals.

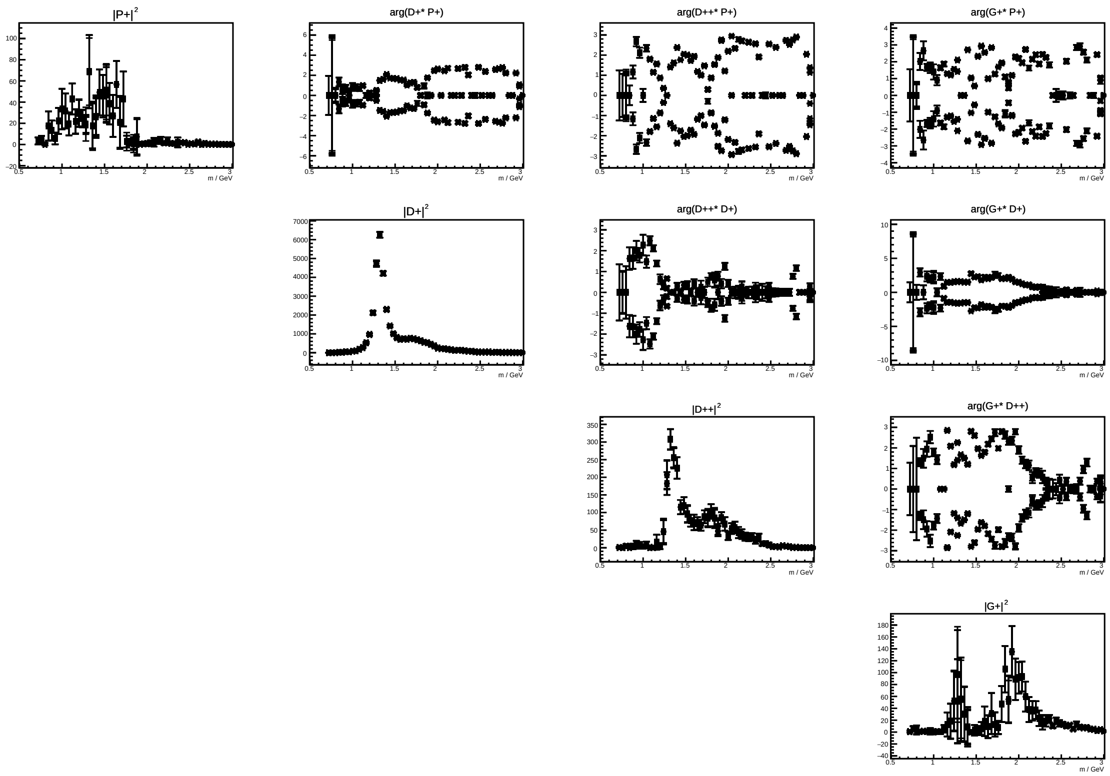

Figure 6.10: Results of the PWA for the $\eta\pi^-$ final state for positive reflectivity waves. Analyzed are the events with $0.393\,\mathrm{GeV}^2 < t'$. On the diagonal, the intensity of the given partial wave is displayed, while the relative phase between the partial waves are shown on the off-diagonals.

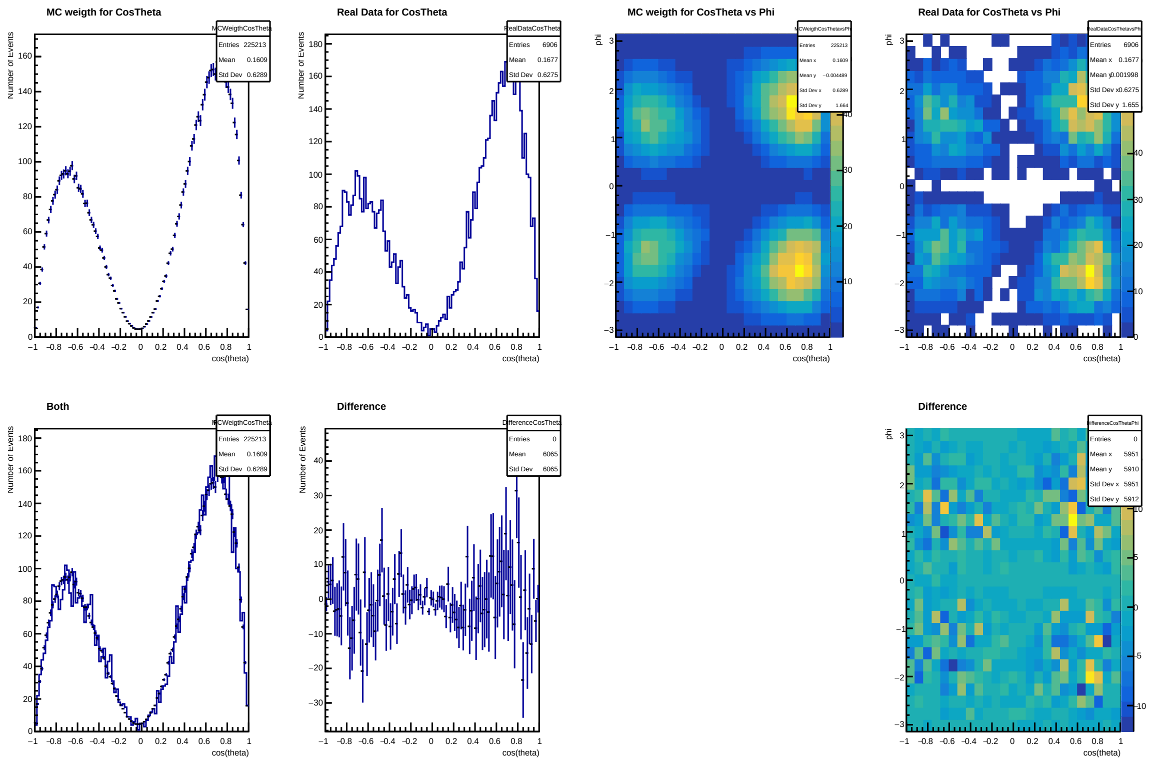

Figure 6.11: Diagrams for $\cos\theta_{\mathrm{GJ}}$ and $\cos\theta_{\mathrm{GJ}}$ versus ϕ_{GJ} for all COMPASS events with $0.150 < t' < 0.242$ and $1.30\,\mathrm{GeV} < m_{\eta\pi^-} < 1.34\,\mathrm{GeV}$. The MC events are weighted according to eq. (5.13). In the bottom row, the difference between the COMPASS and weighted MC data are shown, as well as both together in one diagram.

Notice, that the peak position of the $a_2(1320)$ and the $a_4(2040)$ signal do not change with changing t', while the background in the D-wave as well as the signal in the P-wave adjust. This is of course expected, as the resonance parameters should not depend on the transferred momenta. This behavior might make it possible to fit the $a_2(1700)$, the first excitation state of the $a_2(1320)$, which appears as a broader structure at 1.7 GeV.

6.2 MC weight diagrams

At last, for the $\eta\pi^-$ final state, the $\cos\theta_{\mathrm{GJ}}$ and ϕ_{GJ} diagrams are shown for COMPASS data and MC data, weighted with the fit results according to eq. (5.13) (see fig. 6.11).

The results are shown for the mass slice near the $a_2(1320)$ resonance ($1.30\,\mathrm{GeV} < m < 1.34\,\mathrm{GeV}$) in the second t' slice ($0.150\,\mathrm{GeV}^2 < t' < 0.242\,\mathrm{GeV}^2$). The distributions can be reconstructed very accurately for both $\cos\theta_{\mathrm{GJ}}$ and ϕ_{GJ}, which signals good MC data and a good fit for the over all data sample.

6.3 Partial-wave analysis in the $\eta'\pi^-$ final state

The analysis in the $\eta'\pi^-$ final state follows the same principles as that for the $\eta\pi^-$ final state, with the exception of the $m = 2$ D-wave, as the contribution of this wave is anyway suppressed and the available amount of data is lower as in the $\eta\pi^-$ final state. In addition, the analysis in [28] did not include this wave for the $\eta'\pi^-$ final state either. First, the intensities and real and imaginary parts of the positive reflectivity waves are shown in the full mass spectrum (see fig. 6.12). Although, the G-wave seems to describe the data sample somewhat around a mass of 3 GeV, the negative reflectivity waves still catch an equal amount of intensity each above 3 GeV. The high mass region is therefore again not properly described by this data set, which can be seen as another hint to the fact, that one should extend the wave set to waves with higher l.

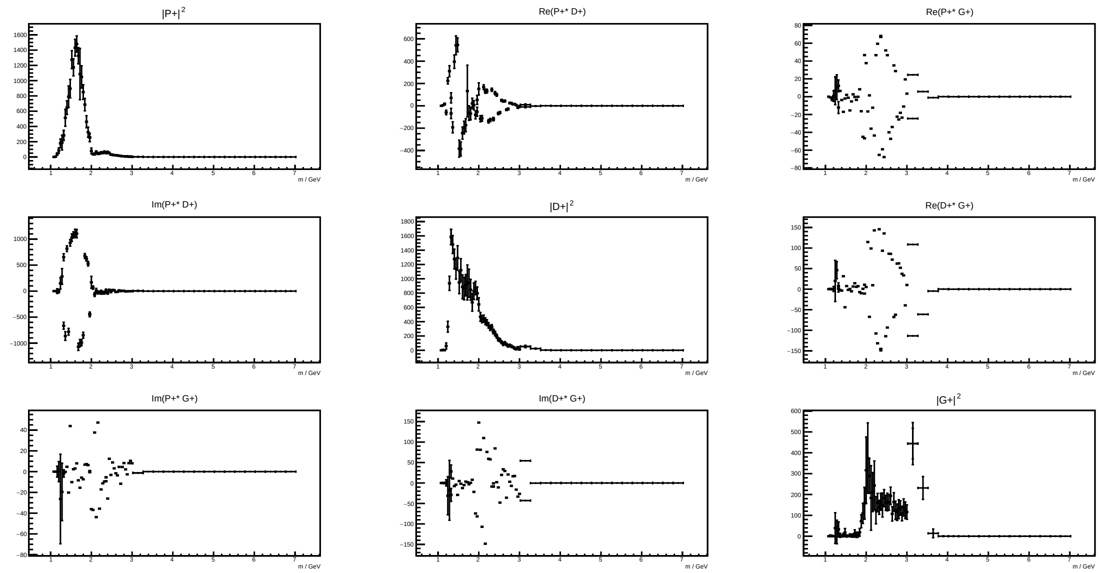

Figure 6.12: Results of the PWA for the $\eta'\pi^-$ final state, for the partial waves with positive reflectivity. On the diagonal, the intensity of the given wave is shown. The imaginary part of the interference is shown on the bottom off-diagonals and the real part of that on the top off-diagonals.

Focusing again on the phase and intensity diagrams in the low mass region, the effects described at the beginning of this chapter are now visible. A rapid phase motion can be seen in the phase between the P- and D-wave between 1.3 GeV and 1.6 GeV, which hits to the two resonance states, the $a_2(1320)$ and the π_1. Judging from the relative strength of these waves, the P-wave is now way more prominent than the D-wave and the signal around 1.6 GeV way more resonance-like. The sign ambiguities as well as the ambiguities caused by the method to determine the phase are again visible.

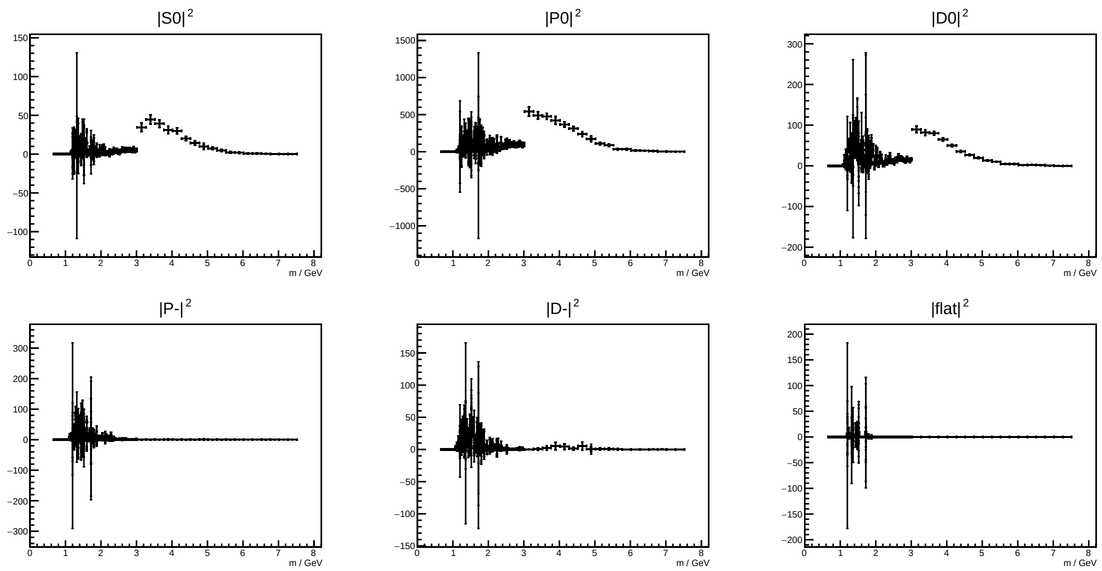

Figure 6.13: Results of the PWA for the $\eta'\pi^-$ final state, for the partial waves with negative reflectivity and the flat wave. Displayed are the intensities of the given partial waves.

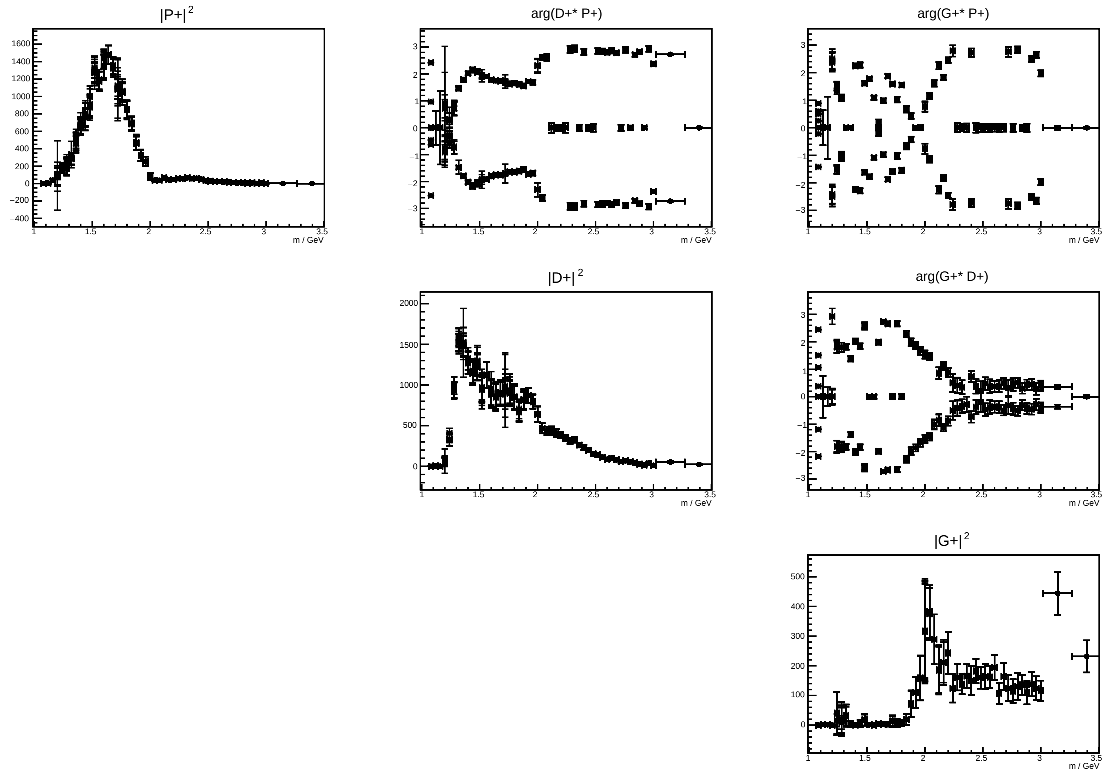

Figure 6.14: Results of the PWA for the $\eta'\pi^-$ final state for positive reflectivity waves. Analyzed is the full data sample, in the full t' range and a closer look to masses below 3 GeV is shown. On the diagonal, the intensity of the given partial wave is displayed, while the relative phase between the partial waves are shown on the off-diagonals.

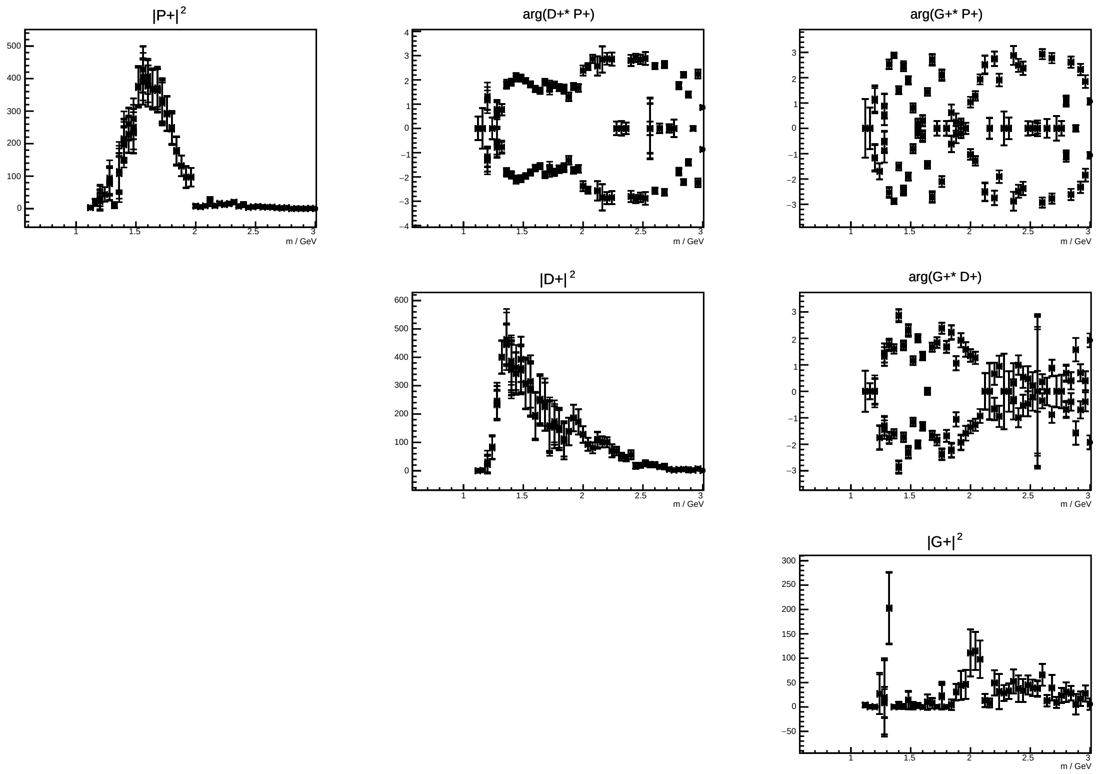

Figure 6.15: Results of the PWA for the $\eta'\pi^-$ final state for positive reflectivity waves. Analyzed are the events with $0\,\mathrm{GeV}^2 < t' < 0.151\,\mathrm{GeV}^2$. On the diagonal, the intensity of the given partial wave is displayed, while the relative phase between the partial waves are shown on the off-diagonals.

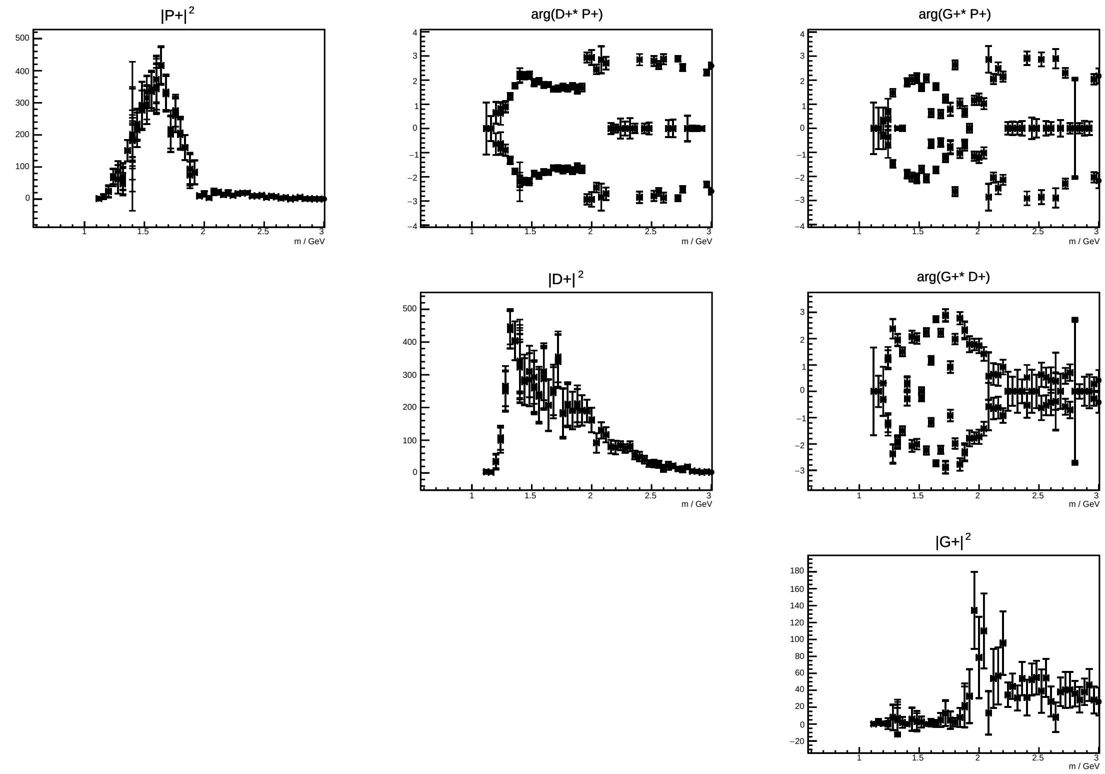

Figure 6.16: Results of the PWA for the $\eta'\pi^-$ final state for positive reflectivity waves. Analyzed are the events with $0.151\,\mathrm{GeV}^2 < t' < 0.242\,\mathrm{GeV}^2$. On the diagonal, the intensity of the given partial wave is displayed, while the relative phase between the partial waves are shown on the off-diagonals.

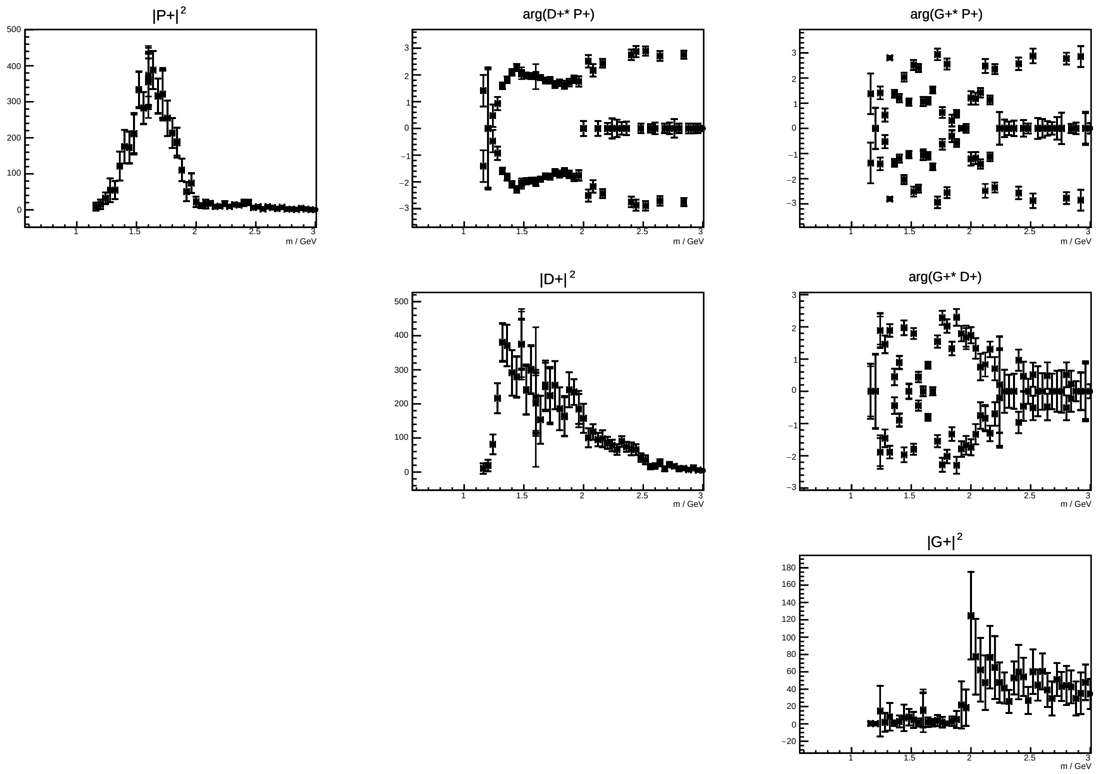

Figure 6.17: Results of the PWA for the $\eta'\pi^-$ final state for positive reflectivity waves. Analyzed are the events with $0.244\,\mathrm{GeV}^2 < t' < 0.398\,\mathrm{GeV}^2$. On the diagonal, the intensity of the given partial wave is displayed, while the relative phase between the partial waves are shown on the off-diagonals.

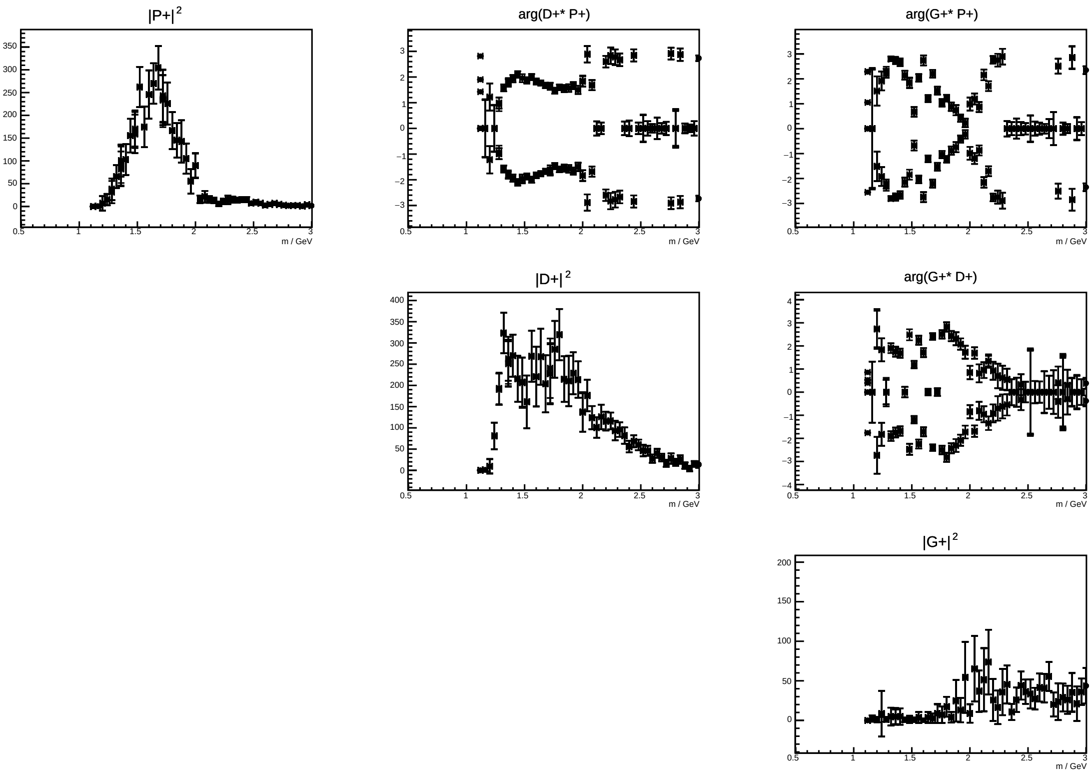

Figure 6.18: Results of the PWA for the $\eta'\pi^-$ final state for positive reflectivity waves. Analyzed are the events with $0.398\,\mathrm{GeV}^2 < t'$. On the diagonal, the intensity of the given partial wave is displayed, while the relative phase between the partial waves are shown on the off-diagonals.

Looking at the different diagrams for changing t' (fig. 6.15, 6.16, 6.17 and 6.18), the peak in the $\eta'\pi^-$ P-wave is very stable, as expected. In addition, the background in the D- and G-wave changes. This leads to the impression, that the exotic signal in the $\eta'\pi^-$ P-wave is the strongest out of the resonant production signals in the $\eta'\pi^-$ final state, as analyzed during this thesis and it makes it very unlikely to come from non-resonant background or be an artifact of the PWA itself.

CHAPTER 7

Summary and Outlook

During this thesis, the reactions $\pi^- p \to \eta\pi^- p$ and $\pi^- p \to \eta'\pi^- p$ were studied, while using the COMPASS data from the 2008 hadron run. This kind of analysis was done before, but recent improvements on the reconstruction and selection of the COMPASS data yielded much more events ($> 40\%$) within these final states. The search for an exotic signal within the $\eta^{(\prime)}\pi^-$ P-wave, as well as the improved number of events, motivates the new analysis.

This thesis starts with the discussion of the partial-wave analysis model, which is used in the end to analyze the COMPASS data, taken in the 2008 hadron run. The negative log-likelihood function is derived and the importance of the knowledge about the detector acceptance emphasized. Consequently, the COMPASS experiment itself is discussed and the key components are presented.

Following that, the way of representing the detector acceptance in form of Monte-Carlo (MC) data is reviewed. A completely new MC data sample, for the $\eta\pi^-$ (approximately 38×10^6 MC events) and $\eta'\pi^-$ (approximately 15×10^6 MC events) final state is generated, using the new MC simulation program TGEANT. The generation was done on the supercomputer Blue Waters, in Illinois, USA. In addition, the parametrization of the ECAL2 Shashlik modules, within the reconstruction program CORAL, is updated for MC events within these final states, i.e. the shower parameters and the energy calibration parameter (the `reserv` parameter).

These MC events are then selected with a new UserEvent function, which closely follows the guidelines of [10], but is adapted for the MC simulation, as well as the COMPASS data tool chain. This UserEvent was also used to cross check the event selection, done in [10]. Approximately 5.5×10^6 $\eta\pi^-$ and 2.8×10^6 $\eta'\pi^-$ final state MC events survived the event selection, while the cross check on the COMPASS data found very similar results as in [10] (changes on the permil level).

In order to investigate the characteristics of the $\eta^{(\prime)}\pi^-$ final state, a partial-wave analysis (PWA) in bins of the four-momentum transfer t' and the mass of the $\eta^{(\prime)}\pi^-$ system was performed, while using the the newly generated MC events and the approved COMPASS events. For that, a new PWA program was developed during this thesis and the underlying principles are explained. Finally, the results of this PWA are shown. Within the $\eta\pi^-$ final state, the D-wave takes up almost all the intensity, as it is expected due to the very prominent $a_2(1320)$. Nevertheless, a small signal can be seen in the exotic P-wave, which becomes less prominent with increasing t'. In addition, the $a_4(2040)$ is visible in the G-wave. Nevertheless, higher masses (above 2.5 GeV) are not described well by the chosen wave set.

For the $\eta'\pi^-$ final state, the exotic P-wave is of similar prominence as the D-wave, which is partially due to the fact, that the mass of the $\eta'\pi^-$ final state is very close to the $a_2(1320)$ threshold and it is therefore not expected to be as prominent as in the $\eta\pi^-$ final state. A very stable signal can be seen in the P-wave throughout all t' slices.

This partial-wave analysis yielded promising results, which are by no means fully understood up to now. A closer look to higher masses and a new partial-wave analysis with more partial waves has to be done, in oder to understand all effects within the data. Partial waves with larger orbital angular momentum l are expected to have a bigger impact on the high-mass region of the data. Higher l waves could therefore solve the problem, that the intensity is increased in the unnatural waves for masses above 3 GeV with the wave set used in this thesis. In addition, the partial-wave results need to be interpreted by a fit, in order to extract possible resonance parameters.

Also, the t' dependence on the cross section can be investigated. In general, $\mathrm{d}\sigma/\mathrm{d}t' \propto (t')^{|m|} \exp(-bt')$ is to be expected, where m is the spin projection to the z-axis [28]. This can be tested by integrating over all masses for a given partial wave in the different t' slices and determining b with a fit to the resulting data.

Regarding the partial-wave analysis itself, the ambiguities have to be solved within the program and one has to understand, why the fit did not distribute any intensity to the flat wave. Also, this analysis only incorporates the COMPASS data of 2008, but there was an additional hadron run in 2009. This data has to be analyzed, reconstructed and selected and finally embedded into the PWA. The increasing amount of data should help to analyze the high mass region better.

Overall, the previous analysis could be reproduced and improved by the higher statistics. With the very adaptive nature of the PWA program it is possible to start in-depth investigations of different combinations of wave sets. The coupled-channel analysis of JPAC [9] can now be done in different t' slices, which should help to disentangle signal and background even further and should increase the stability and precision of the fit results. The separation into different t' slices also enables further investigations of the non-resonant production mechanisms at COMPASS.

Bibliography

[1] M. Tanabashi et al., *Review of Particle Physics*, Phys. Rev. D **98** (3 2018) 030001,
URL: https://link.aps.org/doi/10.1103/PhysRevD.98.030001
(cit. on pp. 1, 3, 20, 23, 29, 41).

[2] D. Alde et al., *Evidence for a* 1^{-+} *exotic meson*, Physics Letters B **205** (1988) 397,
ISSN: 0370-2693,
URL: http://www.sciencedirect.com/science/article/pii/0370269388916863
(cit. on p. 1).

[3] S. A. Sadovsky,
Comments to the partial wave analysis of the $\eta\pi$ *system produced in peripheral* πp *interactions*,
Nucl. Phys. **A655** (1999) 131 (cit. on p. 1).

[4] G. S. Adams et al.,
Observation of a New $J^{PC} = 1^{-+}$ *Exotic State in the Reaction* $\pi^- p \rightarrow \pi^+\pi^-\pi^- p$ *at* 18GeV$/c$,
Phys. Rev. Lett. **81** (26 1998) 5760,
URL: https://link.aps.org/doi/10.1103/PhysRevLett.81.5760 (cit. on p. 1).

[5] A. A. et al., *Exotic* $\eta\pi$ *state in* $\bar{p}d$ *annihilation at rest into* $\pi^-\pi^0\eta p$*-spectator*,
Physics Letters B **423** (1998) 175, ISSN: 0370-2693,
URL: http://www.sciencedirect.com/science/article/pii/S0370269398001233
(cit. on p. 2).

[6] K. Schoenning, *Hadron Spectroscopy with COMPASS at CERN*,
J. Phys. Conf. Ser. **381** (2012) 012029, arXiv: 1112.0511 [hep-ex].

[7] M. Alekseev et al., *Observation of a* $J^{PC} = 1^{-+}$ *exotic resonance in diffractive dissociation of* 190 GeV$/c$ π^- *into* $\pi^- \pi^- \pi^+$, Phys. Rev. Lett. **104** (2010) 241803,
arXiv: 0910.5842 [hep-ex] (cit. on p. 2).

[8] C. Adolph et al.,
Odd and even partial waves of $\eta\pi^-$ *and* $\eta'\pi^-$ *in* $\pi^- p \rightarrow \eta^{(\prime)}\pi^- p$ *at* 191 GeV$/c$,
Physics Letters B **740** (2015) 303, ISSN: 0370-2693,
URL: http://www.sciencedirect.com/science/article/pii/S0370269314008685
(cit. on p. 2).

[9] A. Rodas et al., *Determination of the Pole Position of the Lightest Hybrid Meson Candidate*,
Phys. Rev. Lett. **122** (4 2019) 042002,
URL: https://link.aps.org/doi/10.1103/PhysRevLett.122.042002
(cit. on pp. 2, 62).

[10] R. Reyes Ramos,
Selection of diffractively produced $\eta\pi$ and $\eta'\pi$ final states at the COMPASS experiment,
M. Sc. thesis: Rheinische Friedrich-Wilhelms-Universität Bonn, 2018
(cit. on pp. 2, 21, 23, 25, 61, 67, 69, 70, 72).

[11] T. C. Szameitat,
New Geant4-based Monte Carlo Software for the COMPASS-II Experiment at CERN,
PhD thesis: Albert-Ludwigs-Universität Freiburg im Breisgau, 2016 (cit. on pp. 2, 17).

[12] S. U. Chung, *Techniques of amplitude analysis for two-pseudoscalar systems*,
Physical Review D - PHYS REV D **56** (1997) 7299 (cit. on pp. 6, 7).

[13] P. Abbon et al., *The COMPASS Setup for Physics with Hadron Beams*,
Nucl. Instrum. Meth. **A779** (2015) 69, arXiv: `1410.1797 [physics.ins-det]`
(cit. on pp. 9, 13, 14, 17).

[14] H. Kolanoski and N. Wermes, *Teilchendetektoren, Grundlagen und Anwendungen*,
Springer Spektrum, 2016 (cit. on p. 9).

[15] P. Abbon et al., *The COMPASS experiment at CERN*, Nucl. Instrum. Meth. **A577** (2007) 455,
arXiv: `hep-ex/0703049 [hep-ex]` (cit. on pp. 13–15, 17).

[16] R. Brun and F. Rademakers, *ROOT: An object oriented data analysis framework*,
Nucl. Instrum. Meth. **A389** (1997) 81 (cit. on p. 15).

[17] S. G. et. al., *PHysics Analysis Software Tools*,
URL: `http://ges.home.cern.ch/ges/phast/` (visited on 16/05/2019) (cit. on p. 15).

[18] S. A. et al., *Geant4—a simulation toolkit*, Nucl. Instrum. Meth. **506** (2003) 250 (cit. on p. 17).

[19] T. Szameitat and C. Regali,
TGEANT, A Geant4 based monte carlo simulation for the COMPASS-II experiment,
URL: `https://na58-project-tgeant.web.cern.ch/` (visited on 07/05/2019)
(cit. on p. 18).

[20] W. Renz, *Akzeptanzbestimmung mit einer Monte Carlo Simulation für den*
$\pi^- p \to \pi^- p\eta(\pi^+\pi^-\pi^0(\gamma\gamma))$-Zustand,
B. Sc. thesis: Rheinische Friedrich-Wilhelms-Universität Bonn, 2018 (cit. on p. 19).

[21] M. Mikhasenko, personal communication (cit. on p. 21).

[22] C. L. M. et al., *Deploying a Large Petascale System: The Blue Waters Experience*,
Procedia Computer Science **29** (2014) 198 (cit. on p. 21).

[23] N. C. for Supercomputing Applications, *System Summary*, URL:
`https://bluewaters.ncsa.illinois.edu/hardware-summary` (visited on 08/05/2019)
(cit. on p. 21).

[24] A. Lednev, *Electron shower transverse profile measurement*,
Nuclear Instruments and Methods in Physics Research Section A: Accelerators, Spectrometers,
Detectors and Associated Equipment **366** (1995) 292, ISSN: 0168-9002,
URL: `http://www.sciencedirect.com/science/article/pii/0168900295007172`
(cit. on p. 27).

[25] A. Heimeroth, *Studien zur Monte-Carlo-Simulation von elektromagnetischen Kalorimetern des COMPASS-Experiments am CERN*,
B. Sc. thesis: Rheinische Friedrich-Wilhelms-Universität Bonn, 2018 (cit. on p. 27).

[26] W. Renz, COMPASS note in progress (cit. on pp. 27, 28).

[27] F. James and M. Winkler, *Minuit 2*,
URL: https://root.cern.ch/root/htmldoc/guides/minuit2/Minuit2.html (visited on 09/06/2019) (cit. on p. 38).

[28] T. Schlüter,
The $\pi^-\eta$ and $\pi^-\eta'$ Systems in Exclusive 190 GeV π^-p Reactions at COMPASS (CERN),
PhD thesis: Ludwig-Maximilians-Universität München, 2012 (cit. on pp. 41–43, 52, 62).

APPENDIX A

Own contributions

- GEM expert-on-call for the COMPASS experiment
- Part of the shift crew for the COMPASS experiment
- Monte-Carlo (MC) simulation:
  - Creation of a new beam file, which provides the π^- beam information for TGEANT
  - Testing the new generator for TGEANT
  - Confirming the functionality of the generator for the $\eta^{(\prime)}\pi^-$ final state
  - Generating $\approx 37 \times 10^6$ $\eta\pi^-$ final state MC events
  - Generating $\approx 15 \times 10^6$ $\eta'\pi^-$ final state MC events
  - Developing a new UserEvent for the event selection in PHAST as a cross check to [10], which is not only usable for the COMPASS data, but in addition also for the MC data
  - Determining and adjusting the `reserv` parameter for the new shower parameters, for the Shashlik part of the ECAL2 calorimeter within CORAL
- Partial-wave analysis:
  - Developing a completely new program for the partial-wave analysis of the $\eta^{(\prime)}\pi^-$ final state, which is controlled by a graphical user interface
  - Performing the partial-wave analysis with one set of partial waves for the $\eta^{(\prime)}\pi^-$ final state

APPENDIX B

Cross check on the event selection done in [10]

These diagrams are generated with PHAST, during the event selection of the real COMPASS data and can be compared to them in [10]. Small discrepancies in entry numbers can occur, as this event selection was done in one stage and [10] splits the event selection in two different parts. Notice, that this as well as the original event selection was done on already preselected data, which required a best primary vertex inside a very wide z-range, one or three charge particles leaving the primary vertex and the charge sum of these particles to be -1. For each diagram which follows the previous, the given cut, determined within this diagram is applied. See [10] for more details.

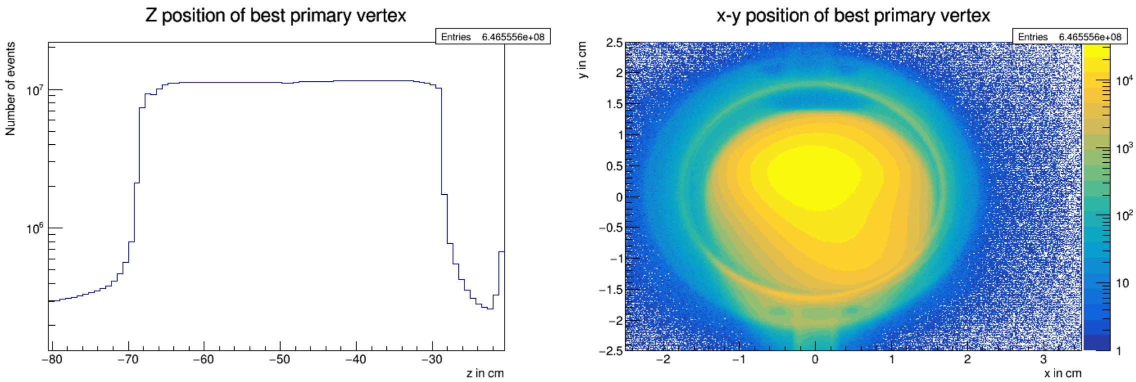

Figure B.1: On the left, the z-position of the primary vertex is shown as well as it's xy-position on the right.

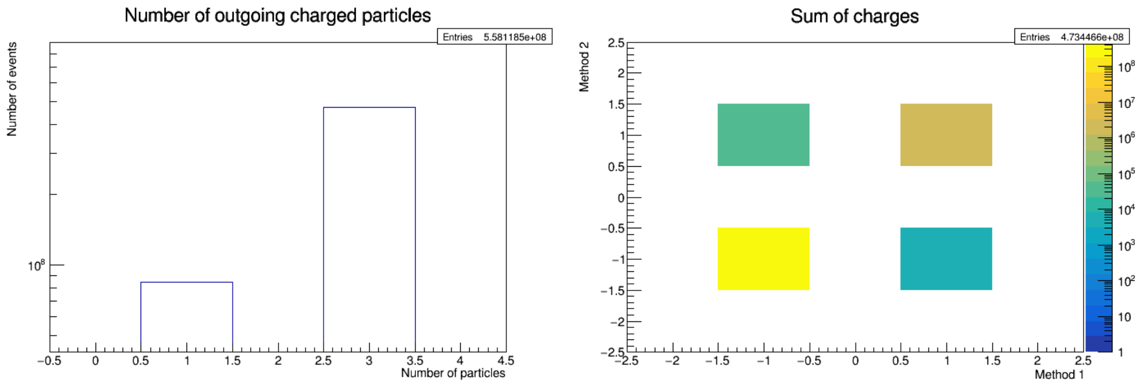

Figure B.2: The number of charged particles leaving the primary vertex is shown left, as well as the charge sum of these particles on the right. Notice, that there are two methods to deduce the charge of a particle in PHAST, hence the two-dimensional graph.

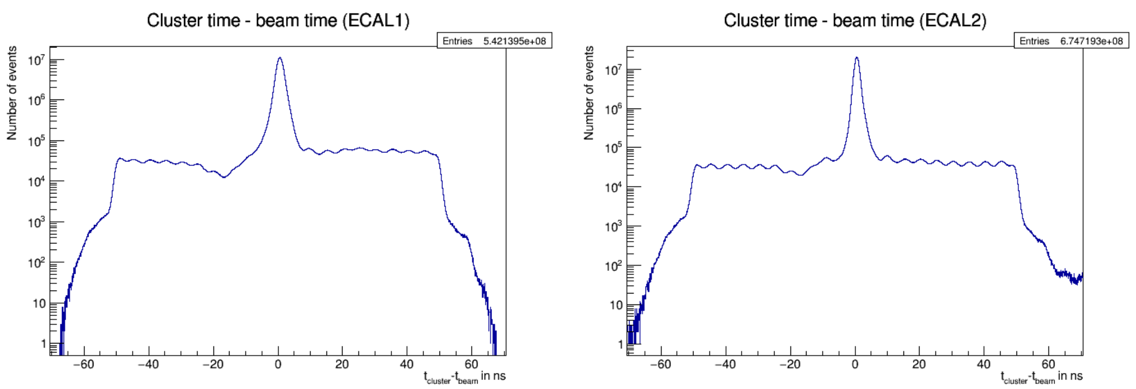

Figure B.3: Here, the time difference of the beam signal, compared to the time signal from the photon clusters determined inside the electromagnetic calorimeters is shown. For ECAL1 on the left and ECAL2 on the right.

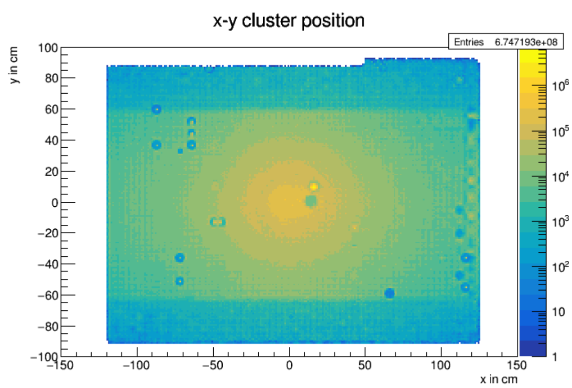

Figure B.4: For each event, the x and y position of a found cluster in ECAL2 is shown.

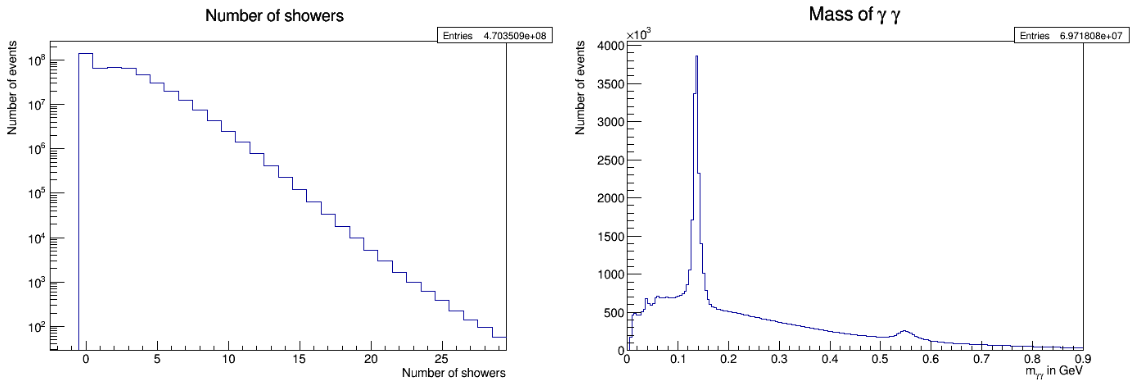

Figure B.5: Here, all shower clusters, found inside the electromagnetic calorimeters are shown on the left and the full mass distribution of the two-photon system is shown on the right. Notice the clear visible peak around 135 MeV, which corresponds to the π^0 and the one around 550 MeV, which corresponds to the η.

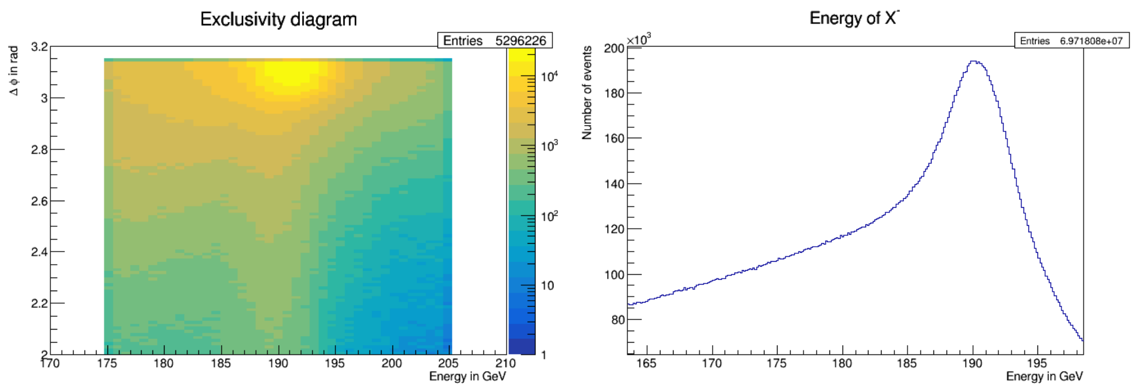

Figure B.6: On the left, the coplanarity angle is plotted vs the mass of X^-, while the energy distribution of X^- is shown on the right. Notice that the coplanarity angle does not become negative, in contrast to eq. (4.5). This is due to the calculation of this angle within the UserEvent, where the angle between two vectors is taken, which is defined to be between 0 and π within the code. However, this makes the cut on the exclusivity even easier.

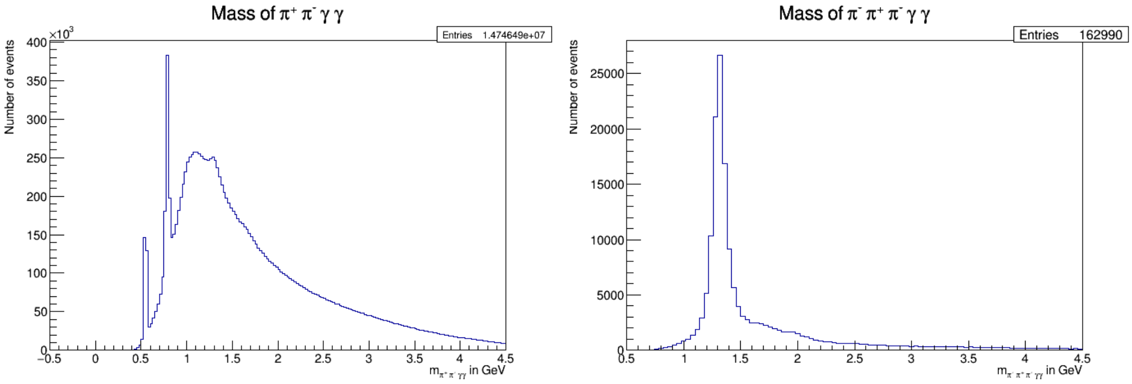

Figure B.7: On the left, the mass of the three-pion system is shown, after a cut on the two photon mass spectrum is done, which required a π^0. Two clear peaks are visible, which correspond to the η and the ω[1]. On the right, the final mass distribution X^- after all cuts, including the cut around the η mass on the three-pion mass spectrum, are applied, is shown. The clear peak around 1.3 GeV corresponds to the $a_2(1320)$

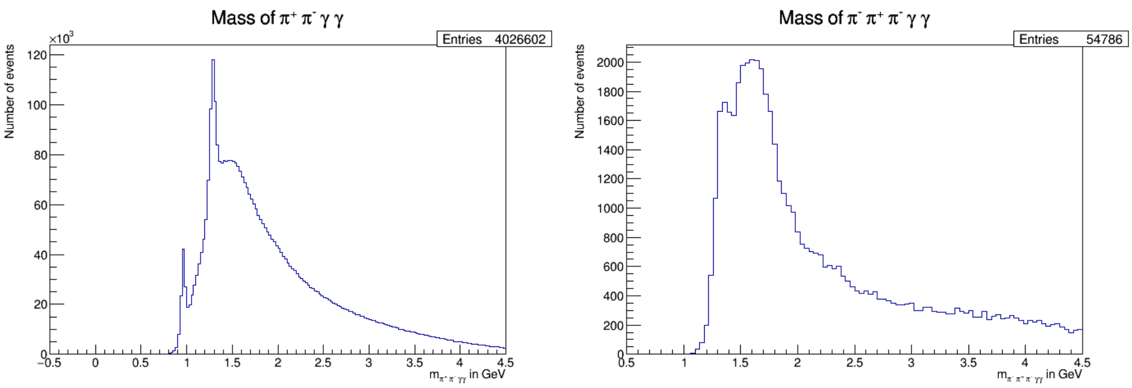

Figure B.8: On the left, the mass of the $\pi\pi\eta$ system is shown, after a cut on the two-photon mass spectrum is done, which required an η. Two clear peaks are visible, which correspond to the $\eta'(958)$ and either the $\eta(1295)$ or the $f_1(1285)$. On the right, the final mass distribution X^- after all cuts, including the cut around the η' mass on the $\pi\pi\eta$ mass spectrum, are applied, is shown.

APPENDIX C

Diagrams for the Monte-Carlo event selection

In the following, the same diagrams as in Appendix B are shown for the Monte-Carlo event selection. On the left, the diagrams for the generated $\eta\pi^-$ final state events and on the right these for the $\eta'\pi^-$ are shown.

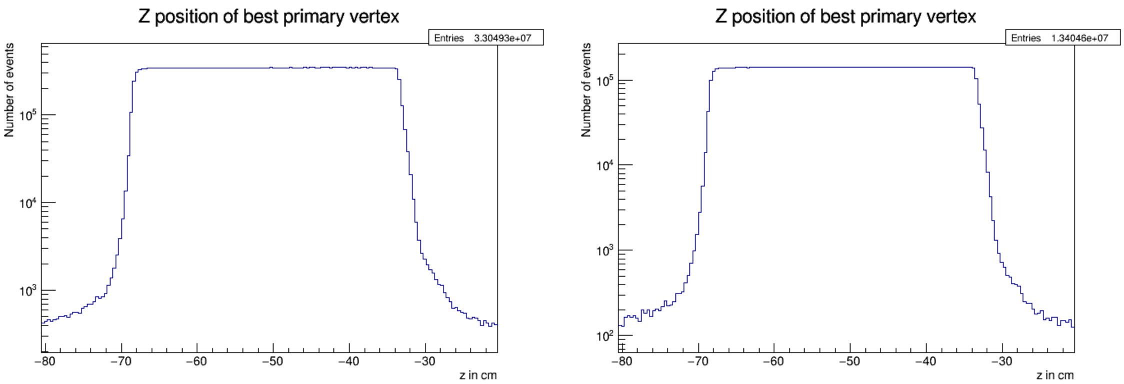

Figure C.1: z-position of the primary vertex.

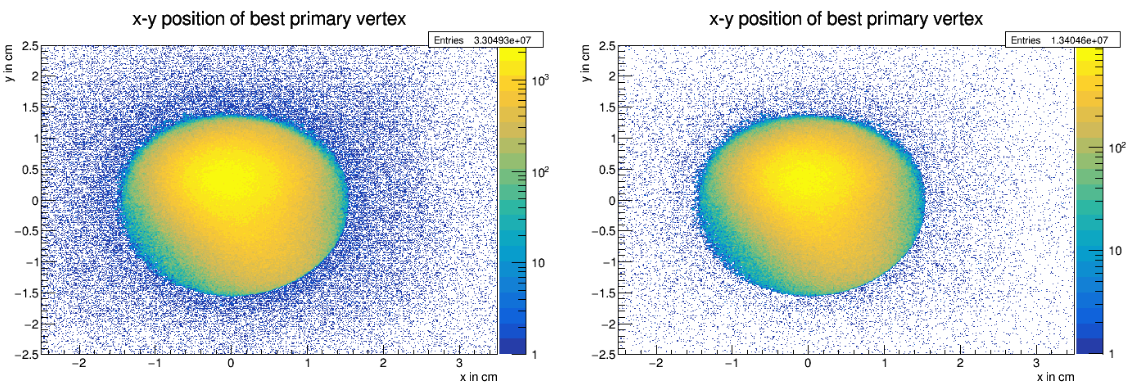

Figure C.2: x and y position of the primary vertex.

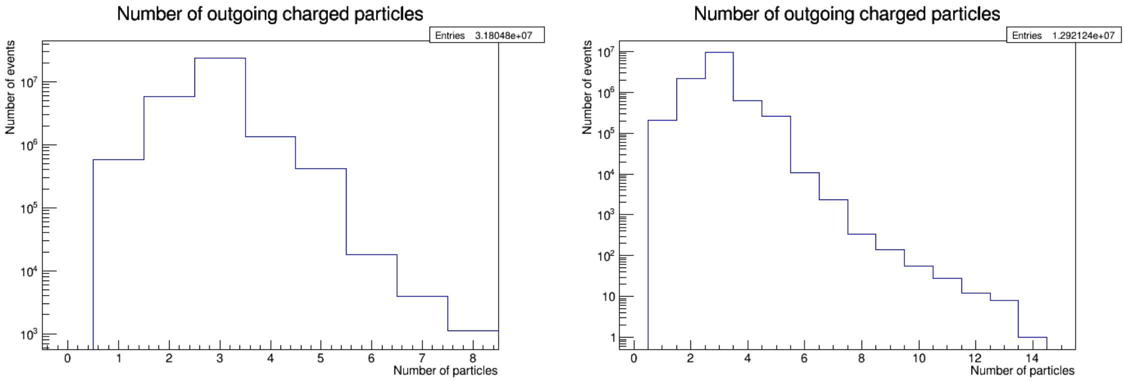

Figure C.3: The number of charged particles leaving the primary vertex.

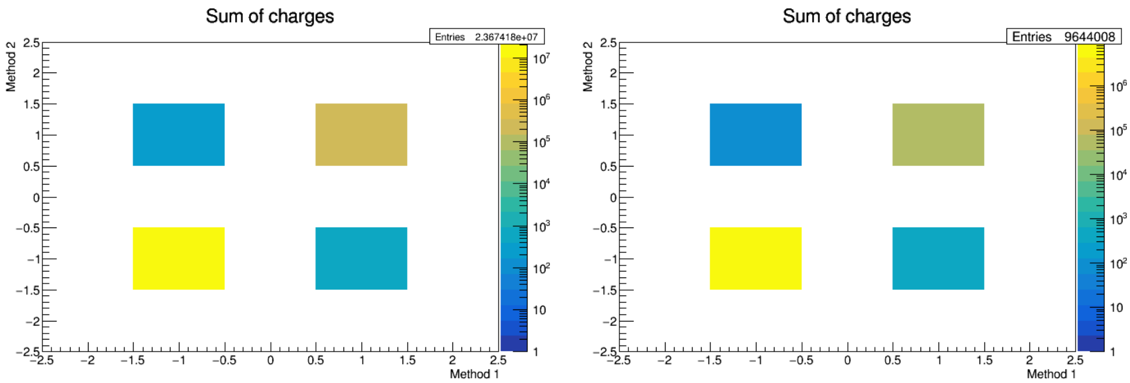

Figure C.4: The charge sum of the three outgoing particles from the primary vertex, shown for both methods within PHAST.

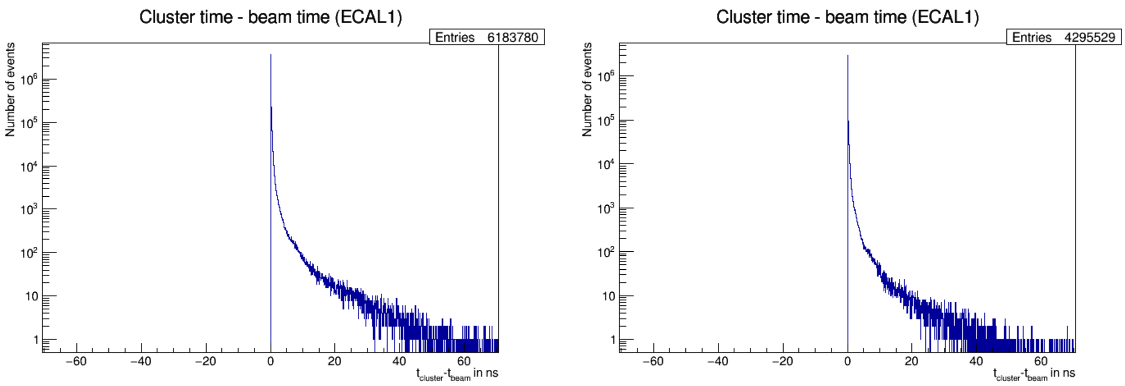

Figure C.5: Difference between cluster time of ECAL1 and beam time.

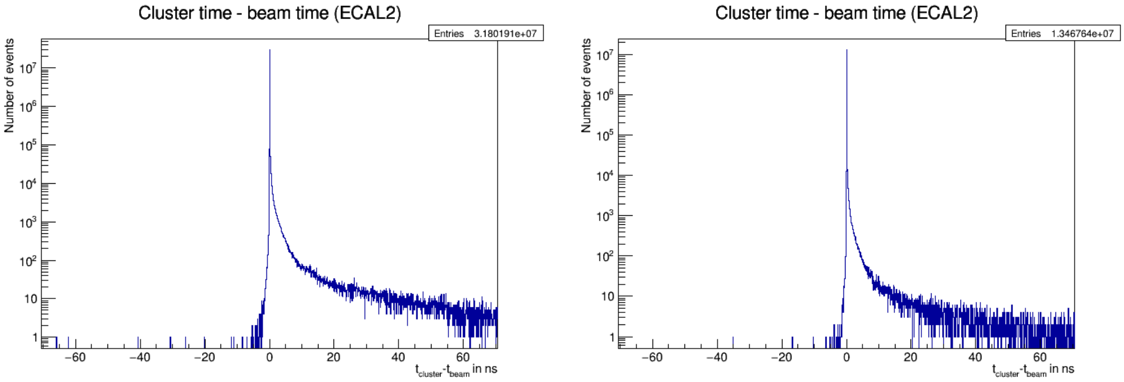

Figure C.6: Difference between cluster time of ECAL2 and beam time.

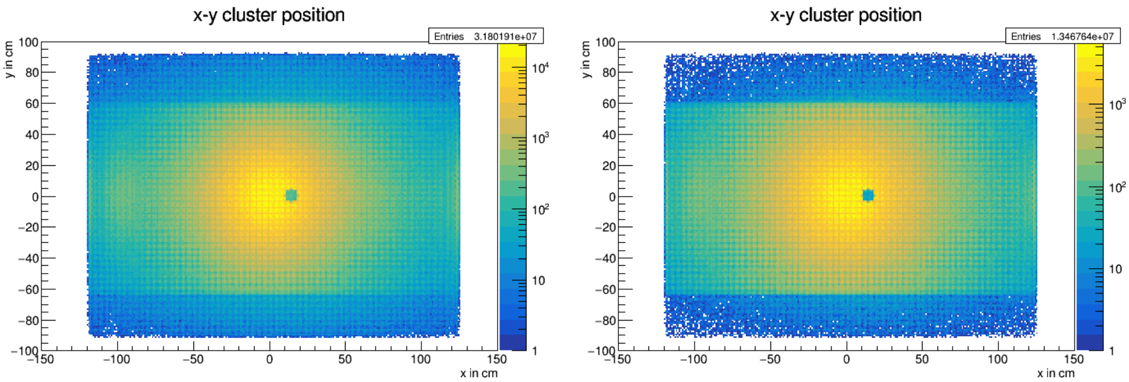

Figure C.7: x, y position of given clusters in ECAL2

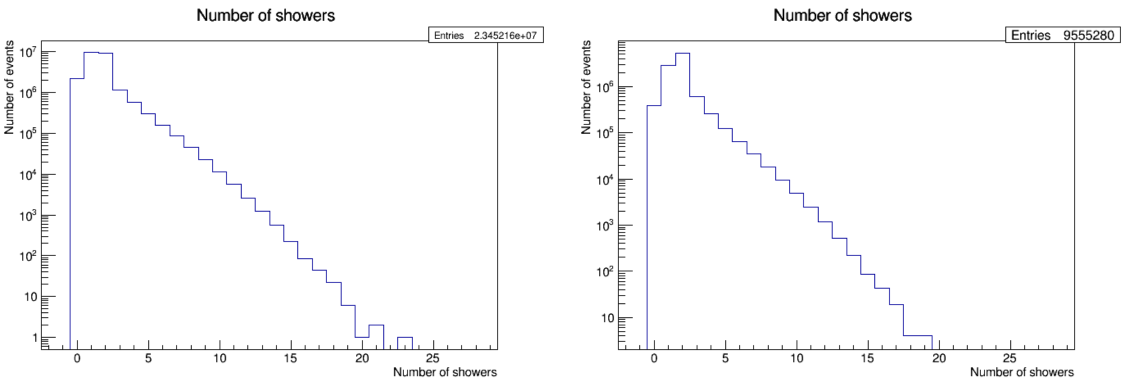

Figure C.8: Number of good clusters determined in the electromagnetic calorimeters

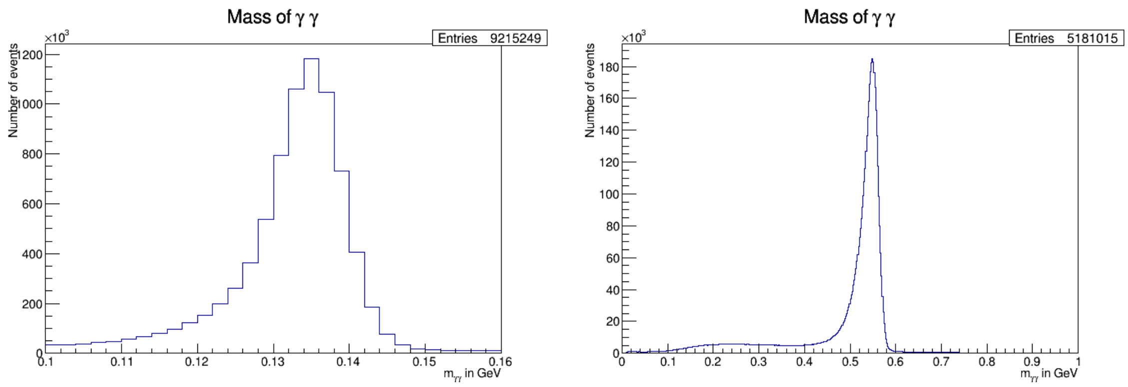

Figure C.9: Two-photon mass spectrum.

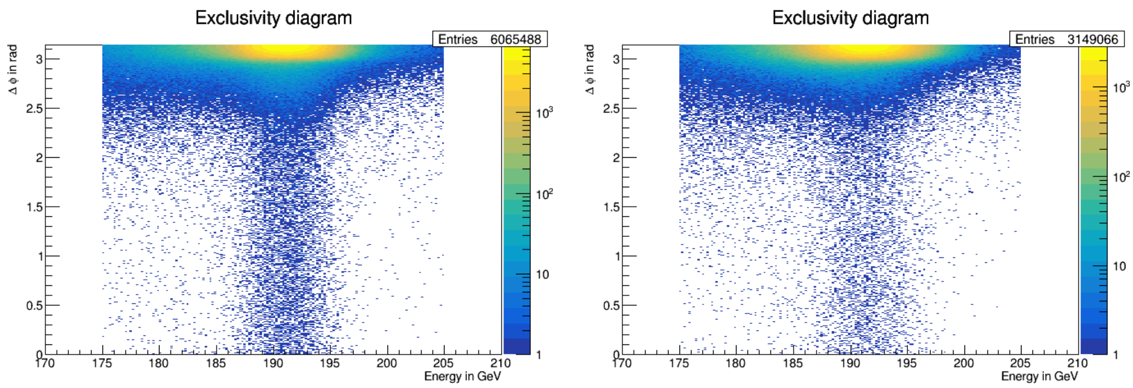

Figure C.10: The coplanarity angle is shown on the y-axis, while the energy of X^- is shown on the x-axis.

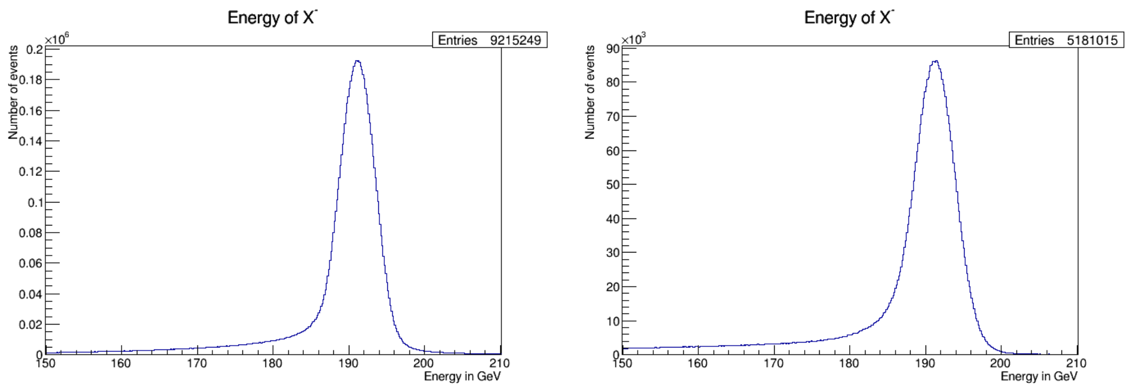

Figure C.11: Energy of the intermediate state X^-

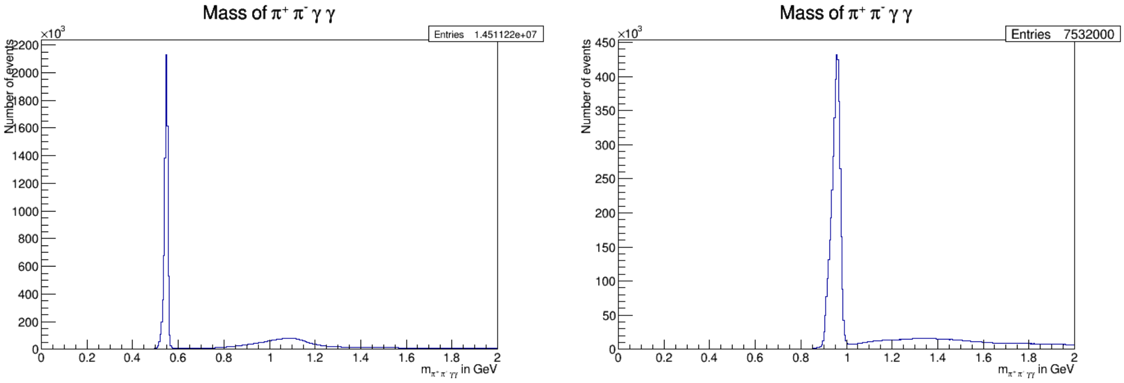

Figure C.12: $\pi\pi\gamma\gamma$ mass spectrum, where one can see a clear η peak in the left diagram and a clear η' peak in the right. Notice the background, which comes from the fact, that the bachelor π^- is indistinguishable of the π^- emerging of the $\eta^{(\prime)}$ and therefore one bad background $\pi^-\pi^+\gamma\gamma$ arises per event.

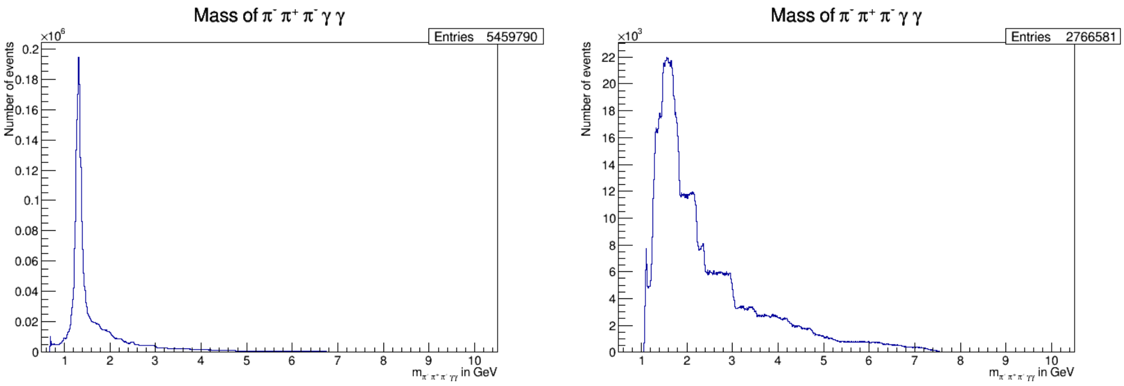

Figure C.13: The mass of the intermediate state X^- is shown. The rather edgy distribution rises from the fact, that the Monte-Carlo data is produced in bins with different amount of events per bin.

List of Figures

List of Tables